UNIVERSITÀ
DEGLI STUDI
FIRENZE

DOCTORAL PROGRAMME IN INDUSTRIAL ENGINEERING
DOTTORATO DI RICERCA IN INGEGNERIA INDUSTRIALE

XXXII

Wireless Charging of Electric Vehicles: Analysis, Design and Experimental Test of a Secondary Side Controlled System

ING/IND-32

Doctoral Candidate
Fabio Corti

Supervisors
Prof. Alberto Reatti

Prof. Luca Pugi

Prof. Marco Pierini

Ing. Andrea Nepote

External Referees
Prof. Augustin Mpanda

Prof. Ermanno Cardelli

Dean of the Doctoral Programme
Prof. Maurizio De Lucia

Years 2016/2019

Acknowledgments

Firstly, I would like to express my sincere gratitude to my advisor Prof. Marco Pierini and Prof. Albert Reatti for giving me the opportunity to enjoy this wonderful professional experience.

I want to also thank Eng. Andrea Nepote, for the continuous support of my Ph.D study and related research, for his patience, motivation, and his guidance that helped me in all the time of research.

Thanks to Marelli Europe S.p.A for funding this research.

I am also grateful to my co-advisor, Prof. Luca Pugi, who shares a great amount of knowledge, suggestions, and experience with me.

Besides my advisors, I would like to thank my talented colleagues at University of Florence: Dr. Lorenzo Berzi, Dr. Riccardo Barbieri, Dr. Libero Paolucci, Dr. Edorardo Locorotondo, Dr. Vincenzo Cultrera and Dr. Giacomo Talluri and Dr. Carlos Iturrino for their insightful comments and encouragement, but also for the hard questions which encouraged me to widen my research from various perspectives.

Finally, thanks to my parents for supporting me throughout my years of study, through the process of researching and my life in general.

Thank you all.

Summary

In the last decades, Wireless Power Transfer (WPT) has attracted increasing interest from industry and academic research because of its possible applications. In this thesis, the application of WPT to the Electric Vehicle (EV) charging is studied. This project was born thanks to the collaboration with MARELLI EUROPE S.p.A., and it has as objective the creation of an on-board vehicle converter able to provide a desired current charging profile to the battery and simultaneously maximize the transmission efficiency. Based on the standards concerning the static wireless charging, the power charging level has been set to P_o=3.7kW. For a simple reading, the thesis is organized as following.

In **Chapter 1**, an introduction explaining how EV can contribute to greenhouse gases reduction is presented. All the advantages of the EV wireless charging and how it can help to the spreading of EVs, is discussed.

The techniques used to transfer power from a transmitter to a receiver without a direct connection are discussed in **Chapter 2**. These can exploit the magnetic field (inductive WPT), the electric field (capacitive WPT) and the electromagnetic field (Radiative WPT). For each technique, the principle of operation and several applications found in literature are shown. For the EV application, the inductive wireless power transfer is the most suitable, and it is used in this project.

In **Chapter 3** the state of the art on the EV wireless charging is shown. Starting from the SAE J2954, the specifications of the proposed system will be presented.

In order to transfer the power with high transmission efficiency, the resonance between the inductance of the coils and some external capacitances is exploited. In **Chapter 4**, the behavior of several compensation topologies under load resistance, frequency and coupling coefficient variation is analyzed. A comparison between them is shown and the adoption of the Series-Series compensation in this project, is justified.

In **Chapter 5**, the procedure used for the PADs geometry optimization is shown. An overview of different coils geometry is presented. Being this project focused on the static wireless charging and the misalignment initially neglected, the circular coil is adopted. The Finite Element Analysis (FEA) was used to optimize the geometry and subsequently the results have been validated experimentally. The human exposure to magnetic field density is studied.

After sizing the system infrastructure, the attention is placed on the control strategies in **Chapter 6**. The control must perform two tasks: the first one is to provide to the vehicle the desired charging profile, while the second one is the maximization of the transmission efficiency. In this chapter two different control strategies are shown, highlighting the advantages and disadvantages of each one.

In **Chapter 7** some practical considerations for the prototype realization are described. A brief description of the main components used to implement the system is given and their use justified.

Finally, in **Chapter 8**, the experimental setup and the performance achieved from the designed system are presented and discussed.

Publications

During the PhD course, the research was focused mainly on wireless power transmission techniques, leading to the following journal publications.

- A. Ayachit, F. Corti, A. Reatti, M. Kazimierczuk, , "Zero-Voltage Switching Operation of Transformer Class-E Inverter at Any Coupling Coefficient", IEEE Transactions on Industrial Electronics, Vol. 66, Issue 3, May 2018, pp. 1809-1819.
- L. Pugi, A. Reatti, F. Corti, "Application of modal analysis methods to the design of wireless power transfer systems", Meccanica, Vol. 54, Issue 1-2, January 2019, pp.321-323.
- L. Pugi, A. Reatti, F. Corti, "Application of Wireless Power Transfer to Railway Parking Functionality: Preliminary Design Considerations with Series-Series and LCC Topologies", Vol. 2018.
- L. Pugi, A. Reatti, F. Corti, R. Mastromauro, "Modelling of inductive resonant transfer for electric vehicles", International Journal of Electric and Hybrid Vehicles, Vol.10, Issue 2, 2018, pp. 131-160.

and to the following conference publications

- L. Pugi, A. Reatti, F. Corti, "Wireless Power Transfer for Static Railway Applications", International Conference on Environment and Electrical Engineering, 12-15 June 2018, Palermo.
- F. Corti, A, Reatti, M. Pierini, R. Barbieri, L. Berzi, A. Nepote, "A Low-Cost Secondary-Side Controlled Electric Vehicle Wireless Charging System using a Full-Active Rectifier" International Conference of Electrical and Electronic Technologies for Automotive,9-11 July 2018, Milano.
- A. Reatti, F. Corti, A. Ayachit, M. Kazimierczuk, "Design of a loosely coupled transformer loaded series-parallel class-DE ZVS inverter", 54th IEEE/IAS Industrial and Commercial Power Systems Technical Conference, 7-10 May 2018, Niagara Falls, Canada.
- F. Corti, A, Reatti, M. Pierini, R. Barbieri, L. Berzi, L. Pugi, "Application of induction power recharge to garbage collection service", IEEE 3rd International Forum on Research and Technologies for Society and Industry, 11-13 September 2018, Modena.
- B. Allotta, L. Pugi, F. Corti, A. Reatti, "Wireless power recharge for underwater robotics", 17th IEEE International Conference on Environment and Electrical Engineering, 6-9 June 2017, Milan.
- L. Pugi, A. Reatti, F. Corti, R. Mastromauro, "Inductive power transfer: Through a bond graph analogy, an innovative modal approach", 17th IEEE International Conference on Environment and Electrical Engineering, 6-9 June 2017, Milan.

The research was not exclusively limited to the wireless power transmission, but also other aspects of power electronics and reliability were investigated:

- N. Kollipara, M. Kazimierczuk, A. Reatti, F. Corti, "Phase control and power optimization of LLC converter" ,Symposium on Circuits and Systems, 26-29 May 2019, Sapporo, Japan.
- A. Reatti, F.Corti, A. Tesi, A. Torlai, M. Kazimierczuk, "Nonlinear exact analysis and solution of power stage of DC-DC PWM boost converter" , Symposium on Circuits and Systems, 26-29 May 2019, Sapporo.
- A. Reatti, F.Corti, A. Tesi, A. Torlai, M. Kazimierczuk,, "Effect of parasitic components on dynamic performance of power stages of DC-DC PWM buck and boost converters in CCM", Symposium on Circuits and Systems, 26-29 May 2019, Sapporo, Japan.
- A. Baidhani, M. Kazimierczuk, T. Salvatierra, A. Reatti, F.Corti, "Sliding-mode voltage control of dynamic power supply for CCM", IEEE International Symposium on Circuits and Systems, 26-29 May 2019, Sapporo, Japan.
- A. Reatti, F. Corti, G. Migliazza, E. Lorenzani, "Control Strategies for Class-E Resonant Inverter with Wide Load Variation", IEEE International Conference on Environment and Electrical Engineering, 12-15 June 2018, Palermo.
- M. Catelani, L. Ciani, F. Corti, V. Sorrentino, A. Ayachit, M. Kazimierczuk, "Reliability analysis and electrical characterization of a Class-E resonant inverter", IEEE International Instrumentation and Measurement Technology Conference, 14-17 May 2018, United States.
- I. Azigenberg, F. Corti, A. Luchetta, A. Reatti, S.Manetti, M. Kazimierczuk "A multi-step approach to the single fault diagnosis of DC-DC switched power converters", IEEE International Symposium on Circuits and Systems, 27-30 May 2018, Firenze.
- F. Corti, A. Luchetta, A. Reatti, S.Manetti, M. Kazimierczuk, "Class-E DC-AC resonant inverter design centering", 17th IEEE International Conference on Environment and Electrical Engineering, 6-9 June 2017, Milan.
- F. Corti, A. Luchetta, A. Reatti, S.Manetti, M. Kazimierczuk,"Fault detection in Class-E^2 resonant converters", IEEE International Instrumentation and Measurement Technology Conference, 22-25 May 2017, Torino.

Table of contents

List of figures

List of tables

Acronyms List

AGV	Automatic Guided Vehicle
CDIAC	Carbon Dioxide Information Analysis Center
D-SC	Dual Side Controlled
CWPT	Capacitive Wireless Power Transfer
D	Duty Cycle
DWC	Dynamic Wireless Charging
EV	Electric Vehicle
EMF	Electromagnetic Field
FAR	Full Active Rectifier
FHA	First Harmonic Analysis
ICEV	Internal Combustion Engine Vehicles
ICES	International Committee on Electromagnetic Safety
ICNIRP	International Commission on Non-Ionizing Radiation Protection
IEEE	Institute of Electrical and Electronics Engineers
IEC	International Electro Technical Commission
IPCC	Intergovernmental Panel on Climate Change
IWPS	Inductive Wireless Power System
KVL	Kirchhoff's Voltage Law
GHG	Greenhouse Gases
OLVEV	On-Line Electric Vehicle
PP	Parallel Parallel
PS	Parallel Series
P-SC	Primary Side Controlled
SS	Series Series
SAE	Society of Automotive Engineers
SoC	State of Charge
SP	Series Parallel
S-SC	Secondary Side Controlled
TF	Transfer Function
VSI	Voltage Source Inverter
WHO	World Health Organization
WPT	Wireless Power Transfer

1. Introduction

1.1. Greenhouse Gas Emission

In the last few years it has been more and more talked about greenhouse gas (GHG). The GHGs are fundamental for the human survival on the earth, keeping the Earth's climate livable. The first studies on the subject are dated in 1895 of the Swedish chemist Svante Arrhenius. He discovered that humans could enhance the greenhouse effect by making carbon dioxide CO_2. Levels of greenhouse gases (GHGs) have gone up and down over the years but nowadays, the levels of these heat-trapping gases are higher than in the past centuries due to pollution made from the humans. For example, in Figure.1.1, the CO_2 concentration over the years is shown.

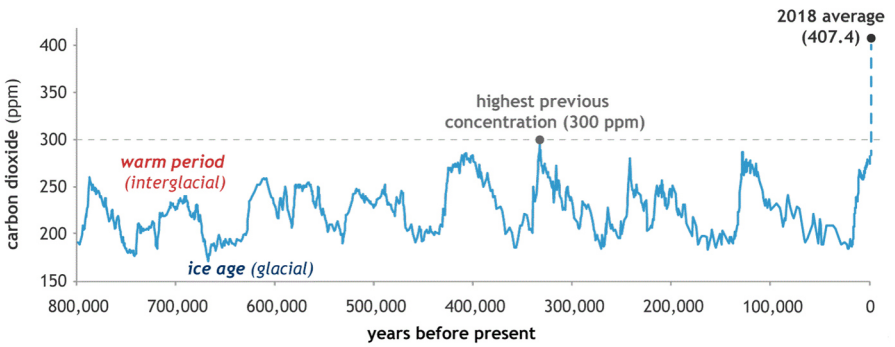

Figure 1.1: Carbon dioxide concentration in the past years. Source: NOA Climate.gov.

The more greenhouse gases are in the atmosphere, the more heat gets trapped, leading to catastrophic consequences such as glaciers melting, sea levels rising and desertification.
At the global scale, the key greenhouse gases emitted by human activities are:

- **Carbon dioxide (CO_2)**: the main source of this gas is the use of fossil fuel. Other sources are the deforestation, land clearing for agriculture, and degradation of soils. Likewise, land can also remove CO_2 from the atmosphere through reforestation, improvement of soils, and other activities.
- **Methane (CH_4)**: Agricultural activities, waste management, energy use, and biomass burning all contribute to CH_4 emissions.
- **Nitrous oxide (N_2O)**: Agricultural activities, such as fertilizer use, are the primary source of N_2O emissions. Fossil fuel combustion also generates N_2O.
- **Fluorinated gases (F-gases)**: Industrial processes, refrigeration, and the use of a variety of consumer products contribute to emissions of F-gases, which include hydrofluorocarbons (HFCs), perfluorocarbons (PFCs), and sulfur hexafluoride (SF_6).

According to the Intergovernmental Panel on Climate Change (IPCC), the percentage of these gases is shown in Figure1.2.

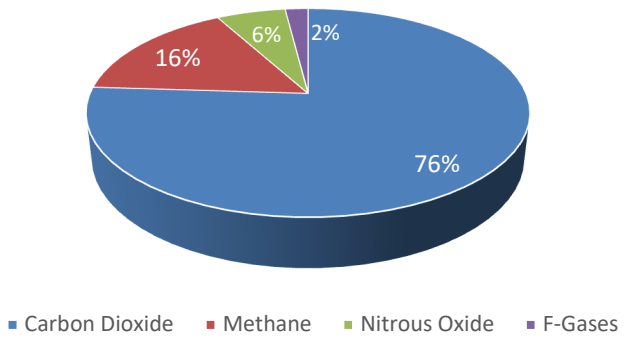

Figure 1.2: Global Greenhouse Gas Emission by Gas. Detail about the sources included in these estimations can be found in the "Contribution of Working Group III to the fifth Assessment Report for the Intergovernmental Panel on Climate Change".

Even if the CO_2 is not the only greenhouse, given its relative quantity, its contribution to the global warming is remarkable.
In addition, the air pollution is currently the leading environmental cause of premature death. According to the World Health Organization (WHO), approximately 7 million premature deaths annually are due to the effects of air pollution.

To reduce the concentration of GHGs it is firstly necessary understand the causes of these emissions. In the last few decades the emissions from several growing economies have been increasing significantly. An analysis made from the Carbon Dioxide Information Analysis Center (CDIAC) shows that China is now the largest emitter, followed by the US, EU-28, India, Russia, Indonesia, Brazil, Japan and Canada as shown in Figure 1.3.

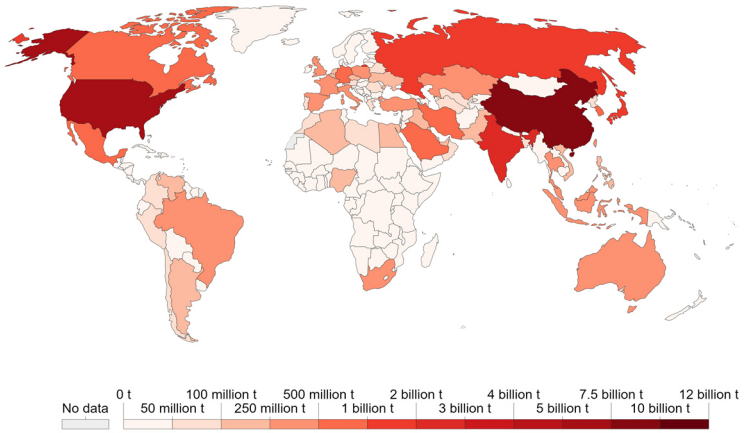

Figure 1.3: Annual CO2 Emission measured in Billions of Tons per year. Source: Global Carbon Project by Carbon Dioxide Information Analysis Center (CDIAC)

Note that several nations that are already top emitters are likely to continue to increase emissions as they undergo development. In contrast, the CO_2 emissions of many high-income regions such as EU-28 and USA have stabilized and, in several cases, decreased in recent decades, as shown in Figure 1.4.

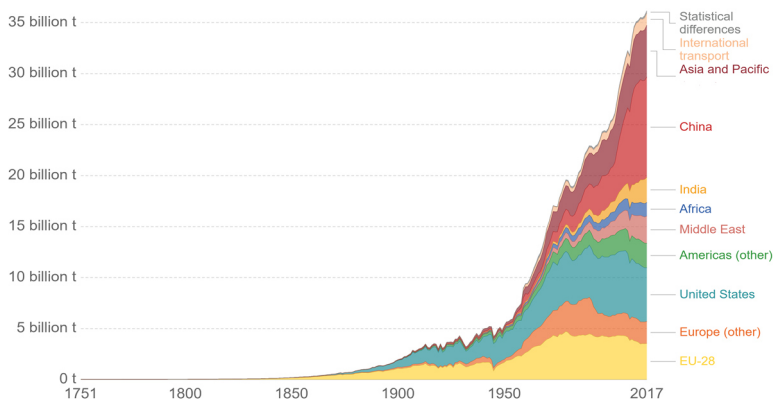

Figure 1.4: Annual CO2 emission measured in tonnes per year by World Region. Source: Global Carbon Project by Carbon Dioxide Information Analysis Center (CDIAC)

Globally, the latest data suggests that over the last few years, global annual emissions of CO_2 have approximately stabilized. Anyway, this slowdown is too recent to ascertain whether this stabilization in emissions represents a peak (with a reduction trend to follow), or a plateau and therefore many efforts still have to be made.

1.2. Dioxide Emission by Sector

As stated by the IPCC, the CO_2 emission by sectoral sources are shown in Figure 1.5.

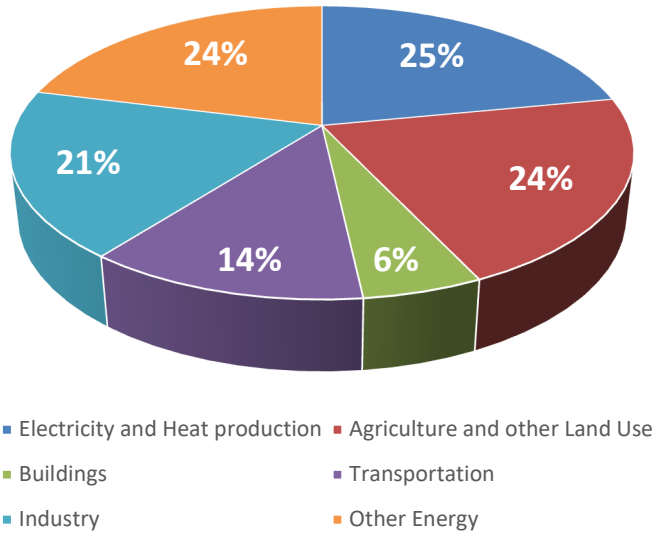

Figure 1.5: CO_2 emission by sectoral source.

Following is reported the activities included in each source:

- **Electricity and Heat Production**: emissions due to public heat and electricity production, energy industries, fugitive emissions from solid fuels, oil and gas, manufacturing industries and construction.
- **Transportation**: emissions due to domestic aviation, road transportation, rail transportation, domestic navigation and other transportation.
- **Buildings**: Residential and other sectors.
- **Industry**: production of minerals, chemicals, metals, pulp/paper/food/drink, halocarbons, refrigeration and air conditioning; aerosols and solvents; semiconductor/electronics manufacture; electrical equipment.
- **Agriculture and Other Land use**: methane and nitrous oxide emissions from enteric fermentation; manure management; rice cultivation; synthetic fertilizers; manure applied to soils; manure left on pasture; crop residues; burning crop residues, savanna and cultivation of organic soils cropland; grassland and burning biomass for agriculture or other uses.
- **Other Energy**: solid waste disposal; wastewater handling; waste incineration; other waste handling.

As shown in Fig. 1.5, a large part of the total emission is due to transportation. More and more attention from governments, industries and research is focused on alternative sustainable solutions able to reduce this emission, i.e. the substitution of the Internal Combustion Engine Vehicles (ICEV) with the electric vehicles (EV).

1.3. Static Wireless Charging

To perform an accurate analysis of a vehicle's environmental impact, three distinct life stages of the vehicles experience must be analyzed: manufacturing, operation and end-of-life. Several researches show that the EV is usually more polluting compared to the traditional vehicle during the manufacturing phase because of the large lithium-ion batteries which are material and energy intensive to produce [1].

During the operation phase the situation changes. Being the EVs powered by electricity which is usually a cleaner energy source than gasoline, the EVs reach the traditional car pollution level within at most 18 months continuing to pollute less until the end-of-life. When the capacity of the battery degrades to a point that the vehicle range becomes unacceptable, it must be removed from the vehicle. Environmental regulation such as End-of-Vehicle directives require to automakers to take extended responsibility to their vehicle and components after use. According to the auto industry, degraded battery removed from EV still has around 80% capacity remaining [2], allowing to the use to other applications. Concerning the decommissioning of the vehicle, the EV and internal combustion engine vehicle ICEV use a similar process. All the components of both vehicles are usually disposed while the EV lithium-ion battery pack is usually recycled.

Besides the environmental aspect, there are others that are contributing to the EVs spread such as:

- Long-term economic Saving: in most parts of the world, electricity is cheaper than petroleum, leading to a significant cost advantage. In addition, given the level of efficiency EVs in comparison to ICEV, on a cost per mile basis, fueling an EV is much cheaper than fueling a traditional fuel vehicle.
- Reduced Noise Pollution: electric car is characterized by smooth drive and low noise pollution.
- Low maintenance: electrically powered engines are more reliable than combustion engine.

For all these reasons, as shown in Figure 1.6, it is expected that the use of electric vehicle is going to increase in the next years.

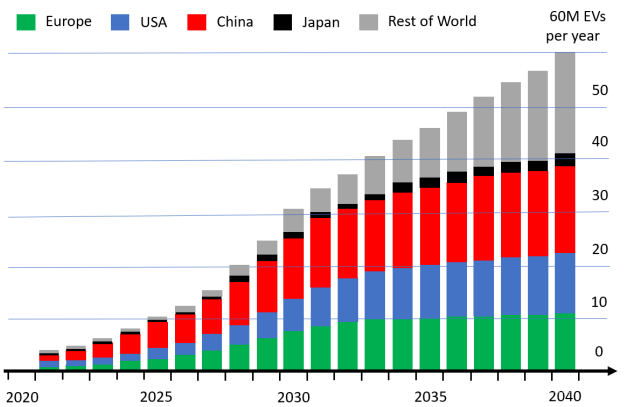

Figure 1.6: Global EV revolution. Source: Bloomberg New Energy Finance.

On the other hand, the EV has also some disadvantages. The EV needs longer refuelling time compared with ICEV. Furthermore, it usually has a limited range. This last characteristic is the cause of range anxiety, that is the fear that a vehicle has insufficient range to reach its destination and would thus strand the vehicle's occupants. It is considered to be one of the major barriers to large scale adoption of all-electric cars.

These disadvantages are strictly related with the battery. Due to lower energy density than fuel, a higher quantity of batteries is needed to ensure acceptable range. This led to heavier vehicles and longer refuelling time. To cope the physic limits of the batteries and solve the problems related with the long charging time and range anxiety many solutions have been studied such as:

- Battery swapping: this solution was introduced by the Chinese carmaker NIO and consists on several battery swap station equipped with a robot which replaces the drained battery with a fully charged spare. [3]

- Dynamic Wireless charging: allows the vehicle to be charged while in motion, allowing to the reduction of the overall battery capacity in the vehicle. This provides the benefit of reducing overall vehicle cost and reduced charging times.

Another problem that is actually limiting the EV diffusion is the reduced number of charging stations dislocated in the territory, many of which with different charging standards and therefore different electric connector. Some of these are shown in Figure 1.7.

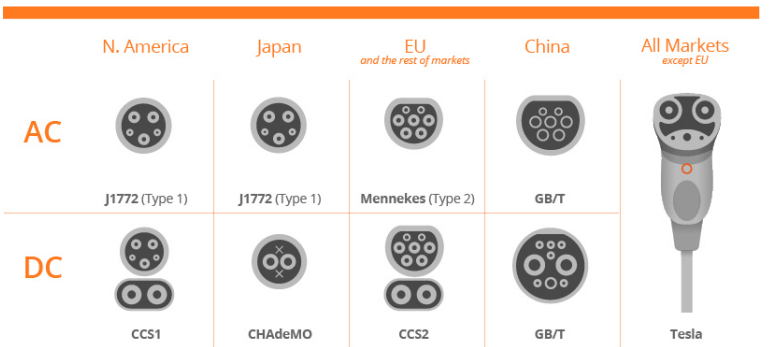

Figure 1.7: EV Charging Connector Types. Sources: Enel X.

A solution able to overcome this problem and simplified the charging process is the EV static wireless charging. The power is transferred from the power grid to the vehicle battery through air and without any contact between them, as shown in Figure 1.8.

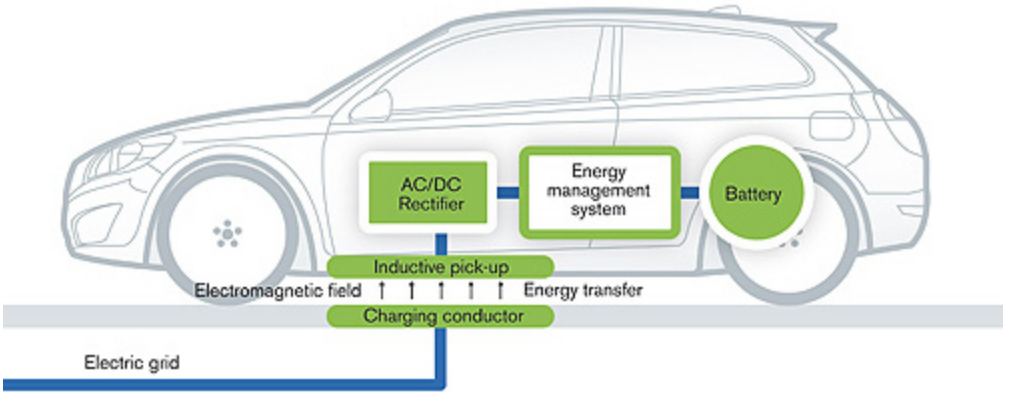

Figure 1.8: Electric Vehicle Wireless Changing System Architecture.

Since it can be embedded underground, exposition to rainy, snowy, humidity and temperature variations are drastically reduced, increasing its reliability, and therefore reducing the ordinary and extraordinary maintenance. Furthermore, it represents the best charging solution for autonomous electric vehicle since the charging process can be completely automated [4].
In the next chapter, the physical principle used to transfer the power from a transmitter to a receive without direct connection between them will be studied in depth.

2. Wireless Power Transfer

A Wireless Power Transfer (WPT) system is made up from a transmitter, which generates a time-varying electromagnetic field and a receiver which manage power from the field and supply an electrical load. Depending on the coupling mechanism exploited, two main categories can be defined: Near Field and Far Field systems, as shown in Figure 2.1.

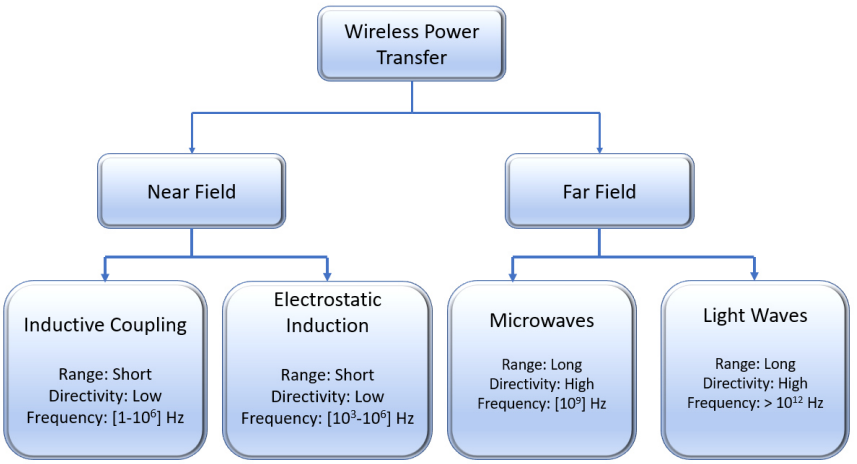

Figure 2.1: Classification of WPT systems

In a Near Field system (also called Non- Radiative system) the power is transferred within one wavelength of the oscillating field. In this region electric and magnetic field oscillate separately. The power can be transferred by magnetic fields using inductive coupling or by electric fields using capacitive coupling. The range of these fields depends on the transmitter size and geometry, but it is usually short. In fact, the power transmitted decrease exponentially with the distance, therefore if the distance between the transmitter and receiver D_{range} is much larger than the antenna diameter D_{ant} , very little power will be received.

In a Far Field (also called **Radiative**) system, the power is transferred over one wavelength of the oscillating field. The electric and magnetic fields are perpendicular to each other and propagate as an electromagnetic wave. Unlike fields, electromagnetic radiation can be focused into a narrow beam. From the Rayleigh criterion, to produce a narrow beam with

significant amount of energy on a distant receiver, an antenna must be much larger than the wavelength of the waves used $D_{ant}>>\lambda=c/f$. Practical beam power devices require wavelengths in the centimeter region or below, corresponding to frequencies above 1 GHz, in the microwave range or above. Due to its omnidirectional character the efficiency is very low, thus more useful to transmit information rather than power.
In the next chapters the principle of operation of each technique is studied.

2.1. Inductive Power Transfer

2.1.1. Principle of Operation

There are two main physical laws that describe how the inductive wireless transmission works: the Ampere's circuit law and the Faraday's law of induction.
In classical electromagnetism, Ampere's circuital law relates the integrated magnetic field around a closed loop to the electric current passing through the loop

$$\nabla \times \vec{H} = \vec{J} \Leftrightarrow \oint_L \vec{H} \cdot d\vec{l} = \oint_L \vec{J} \cdot d\vec{s} = I_{en} \tag{1}$$

where $\vec{J}$ is the current density [A/m^2], I_{en} [A] is the current enclosed in the circuit and $\vec{H}$ [A/m] is the magnetic field. On the other hand, the Faraday's law of induction is a basic law of electromagnetism predicting how a magnetic field will interact with an electric circuit to produce an electromotive force ε. This phenomenon is usually called electromagnetic induction. The general form of Faraday's law is given by

$$\nabla \times \vec{E} = -\frac{\partial \vec{B}}{\partial t} \Leftrightarrow \oint_L \vec{E} \cdot d\vec{l} = -\frac{d}{dt} \int_S \vec{B} \cdot d\vec{A} = \varepsilon \tag{2}$$

where $\vec{E}$ [V/m] is the electric field, $\vec{B}$ [T] is the magnetic flux density and A [m^2] is the area enclosed by the loop. The mathematical definition of magnetic flux Φ through a surface is

$$\Phi = \int_S B dA \tag{3}$$

Thus, the electromotive force ε is proportional to the derivative of the magnetic flux but it causes a current to flow in a direction to oppose change in the magnetic field. This behavior is summarized by the Lenz's law

$$\varepsilon = -\frac{d\Phi}{dt} \tag{4}$$

This phenomenon can be exploited to transfer power between two coils places near each other.

Let's suppose two coils closed to each other, as shown in Figure 2.2.

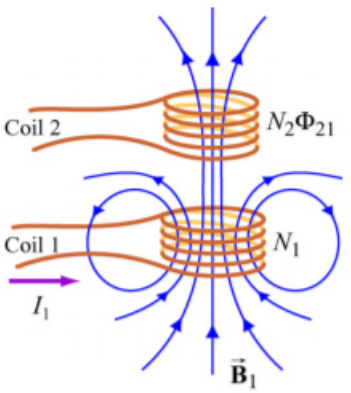

Figure 2.2 Coupling between two coils.

In the first coil, made up from N_1 turns, flows a current I_1 which creates a magnetic field B_1. Since the two coils are close to each other, some of the magnetic field lines through coil 1 will also pass through coil 2. Let Φ_{21} denote the magnetic flux through one turn of coil 2 due to I_1. Now, by varying I_1 with time, there will be an induced emf associated with the changing magnetic flux in the second coil

$$\varepsilon_{12} = -\frac{d}{dt}\int_S \vec{B}\cdot d\vec{A}_2 = \varepsilon = -N_2\frac{d\Phi_{12}}{dt} \tag{5}$$

The time rate of change of magnetic flux Φ_{21} in coil 2 is proportional to the time rate of change of the current in coil 1:

$$N_2\frac{d\Phi_{12}}{dt} = M_{12}\frac{dI_1}{dt} \tag{6}$$

here the proportionality constant M_{21} is called the mutual inductance. It can also be written as

$$M_{12} = \frac{N_2\Phi_{12}}{I_1} = \frac{N_1\Phi_{12}}{I_2} \tag{7}$$

2.1.2 Applications

In literature there are lot of studies and applications that exploit the magnetic field to transfer the power wirelessly, as shown in Table.2.1. The applications vary from the EV wireless charging to the smartphone charging. This technique is usually used to transfer high power (up to several kW) along medium distance (tens of centimeters).

Table 2.1: EXAMPLES OF INDUCTIVE POWER TRANSFER APPLICATIONS

Reference	Year	Frequency	Power	Efficiency	Air Gap	Application
[5]	2015	20 kHz	27 kW	74 %	20 cm	KAIST OLEV BUS Dynamic Wireless Charging
[6]	2009	85 kHz	3.7 kW	90 %	15 cm	Witricity Static Wireless Charging
[7]	2013	22 kHz	3.3 kW	89%	15 cm	ORNL Lab Static Wireless Charging
[8]	2015	10 MHz	10 W	14%	0.8 mm	Mobile Device Wireless Charging

2.2. Capacitive Power Transfer

2.2.1. Principle of Operation

Capacitive Wireless Power Transfer (CWPT) uses electric field to transfer power wirelessly. Its principle of operation is very similar to the operation of a capacitor. In Figure 2.3 is shown the simple structure of a capacitor, made up from a transmitter and a receiver.

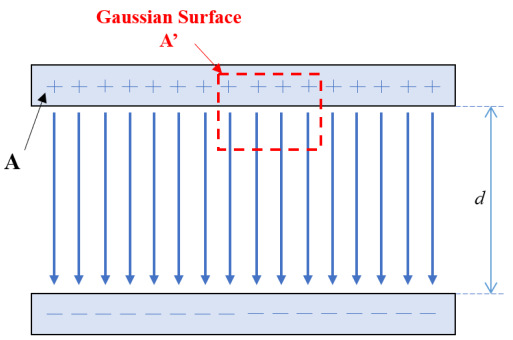

Figure 2.3: two plate capacitor structure.

The capacitance between the primary and secondary side can be derived using the Gauss' law

$$\oiint_S \vec{E} \cdot d\vec{A} = \frac{q_{enc}}{\varepsilon_0} \tag{8}$$

Where $\vec{E}$ is the electric field, S is a closed surface enclosing any volume V, $d\vec{A}$ a vector representing an infinitesimal element of the area surface, q_{encl} is the total charge enclosed within V and ε_0 is the vacuum permittivity. By choosing a Gaussian box with cap area A' to enclose the charge on the positive plate the electric field in the region between the plates is

$$EA' = \frac{q_{enc}}{\varepsilon_0} \Rightarrow E = \frac{\sigma}{\varepsilon_0} \tag{9}$$

The potential difference between the plates is

$$\Delta V = V_- - V_+ = -\int_+^- \vec{E} \cdot d\vec{s} = -Ed \tag{10}$$

However, in computing the capacitance C, the relevant quantity is the magnitude of the potential difference

$$|\Delta V| = Ed \tag{11}$$

and its sign is immaterial. From the definition of capacitance, we have

$$C = \frac{Q}{|\Delta V|} = \frac{\varepsilon_0 A}{d} \tag{12}$$

Note that C depends only on the geometric factors A and d.

2.2.2. **Applications**

Also for the capacitive wireless power transfer the applications are numerous. Generally, the power that can be transferred is lower compared with the inductive, but it still finds several applications such as wireless charging of electric vehicle, undersea charging and implantable devices, as shown in Table 2.2.

Table 2.2: EXAMPLES OF CAPACITIVE POWER TRANSFER APPLICATIONS

Reference	Year	Frequency	Power	Efficiency	Air Gap	Application
[9]	2016	1 MHz	1.8 kW	85%	15 cm	Four Plate System
[10]	2019	625 kHz	100 W	80 %	15 cm	Undersea Wireless Power Transfer System
[11]	2018	13.56 MHz	884 W	91.3 %	12 cm	EV Wireless Charging Prototype
[12]	2018	1 MHz	90 mW	70 %	3 mm	Implantable Medical Devices

2.3. Radiative Power Transfer

2.3.1. Principle of Operation

Among several kinds of wireless power transmission technologies, the radiative power transmission is noticeable for the features of being applied in long-distance transmission. It had been suggested to power helicopter, transfer power to the far-reached areas, and transfer the solar power to the earth by the solar power satellite. With the development of the wireless communications, radars, and radio astronomy, the techniques of the microwave generators and transmitting antennas have been much developed and could be adopted also to transfer power. For this purpose, the rectenna, consisting on an antenna and a rectifying circuit, is usually used. It is well known that the losses of microwaves below X-band are low in the atmosphere. The strength and the direction of the microwave beam could be controlled by the transmitting and the receiving antennas as shown in Figure 3.

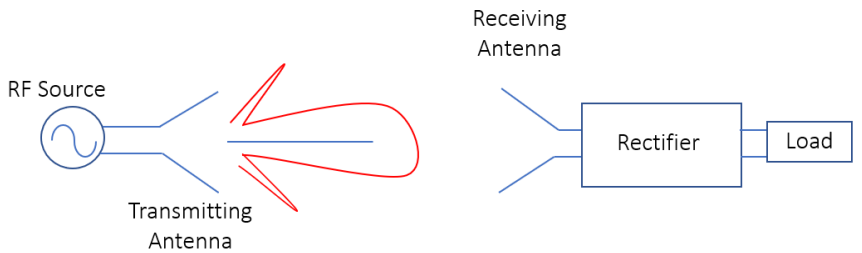

Figure 2.4: Directionality of Radiative Power Transfer.

So, it is a feasible manner to transmit power to a far distance. The study and applications of WPT technology mainly focus on the ISM (industrial, scientific, and medical) bands of L (915 MHz), S (2.45 GHz), and C (5.8 GHz).

2.3.2 Applications

This power transmission technique is characterized by low power transmission and long distance. Several applications are actually based on this technology, such as medical implants and energy harvesting for sensors networks.

Table 2.3: EXAMPLES OF RADIATIVE POWER TRANSFER APPLICATIONS

Reference	Year	Frequency	Power	Efficiency	Air Gap	Application
[13]	2018	2.45 GHz	1.2 mW	40 %	42 cm	Medical Implants
[14]	2019	2.45 GHz	8.56 mW	68 %	40 cm	Energy Harvesting Sensor Networks
[15]	2016	60 GHz	1.22 mW	28 %	4 cm	Compact WPT system

3. Electric Vehicle Wireless Charging: State of Art

Extensive use of gasoline leads to the emission of harmful substances into an environment already suffering from the emission of greenhouse gases. Therefore, to alleviate dependence on conventional energy source and to minimize its harmful effects on the environment, there is a need for alternative solutions such as Electric Vehicles (EVs). Differently from Internal Combustion Engine Vehicles (ICEV), EVs are not a matured technology in terms of vehicle autonomy and charging infrastructure. A lot of research efforts is being carried out by academia and industries to improve their performance. As shown in the previous chapter, the main obstacles to EVs diffusion are strictly related with the low energy density of batteries, which lead to a limited autonomy. In addition, a lower energy density leads to an increasing in the cost of the vehicle as well as weight of the battery pack. For this reason, the technique used to charge the vehicle can play an important role to solve these physical limitations increasing the autonomy.

There are substantially two charging techniques: wired and wireless charging. The first one is performed by a direct connection between the electric power grid and the vehicle. The second one is performed without direct contact between them. Even though wired charging is popular, the problems with messy wires and safety matter in wet environment are a major drawback of this solution. The wireless charging can bring several benefits, summarized below:

- The embedded underground infrastructure makes the charging station insensitive from weather conditions and vandal attack. Exposition to rainy, snowy, humidity and temperature variations are drastically reduced, increasing the system reliability, and therefore reducing the ordinary and extraordinary maintenance.
- Allow completely automated charging process for autonomous electric vehicle, removing the human intervening.
- The Dynamic Wireless Charging (DWC) makes possible to charge the vehicle while it is in motion. This allows a reduction in the number of charging stations and increase the vehicle autonomy. Being the vehicle charged during the route, it can be equipped with a smaller capacity battery pack.

Several studies are available in literature concerning the comparison between wireless and wired charging. The WC can be particularly exploited for vehicles whose route is predefined and it may be advantageous to size the battery capacity according to the number of charging zone and the route. This is usually verified in a wide variety of industrial vehicles that are customized to perform different public services in urban environments. Typical mission profiles associated to these urban services are often ideal to the application of electric vehicles since low speed and frequent accelerations and decelerations are required. The cost of accumulators which are required to assure prescribed vehicle autonomy represents a serious issue for a fast diffusion of this technologies. However, some of the most commonly diffused

public services, such as collection of garbage, involve the execution of fixed route with frequent and prolonged stoppages, a profile mission that suggests the possibility to adopt charging solutions to supply additional energy to the vehicle.
For example, in [16], the application of wireless charging to garbage collection service was studied for the city of Livorno, in Italy. The duration of such time-speed mission is about 10 hours and 30 minutes and 120km with approximately 98 stoppages to load dumpsters. The comparison in terms of final mission state of charge (SoC) of the electric vehicle assuming a static wireless charging system in each stop and without them is presented. The charging time at each stop is assumed the same to collecting garbage, while the charging power is randomly calculated as a value comprehended between maximum available power and its 10%, in order to take into account power variability due to misalignment of wireless charging units.
After a very though analysis of the energy expended from the truck during the whole driving cycle the results are interesting. If at each stops a wireless charging station is used, the final SoC is of 77.5%, while without any charging station the SoC will be 43.6%. The results not only highlight the economic savings, but also highlight the lower battery stress. It is usually suggested to not excessively discharge the EV battery.
Thus, against a higher infrastructure cost [17], various research state that the cost will be amortized thanks to the previously mentioned advantage. In addition, in the European market, the cost of these system will be reduced by 39% compared with the actual value, making it more convenient that the wired solution.

3.1. SAE J2954 Standard

To create a user-friendly wireless charging process, it is vital to define standards for efficiency, power level, operating frequency, EMI, EMC, and safety and testing for the research and commercialisation of the technology. Many international organisations task forces, such as the Society of Automotive Engineers (SAE), International Electro Technical Commission (IEC) and Institute of Electrical and Electronics Engineers (IEEE) have been working with research institutes, governments, universities, and EV automotive industries to enable commercialisation [18]. In Tab. 3.1, the list of announced and on-going updated standards from all over the world are shown.

Table 3.1: EXAMPLES OF RADIATIVE POWER TRANSFER APPLICATIONS

Organization/Society	Standard	Description	Year
Society for Automobile Engineering (SAE)	J2954	Wireless Power Transfer for Light-Duty Plug-In EVs and Alignment Methodology	2017
	J2847/6	Communication Between Wireless Charged Vehicles and Wireless EV Chargers	2015
	J1773	EV Inductively Coupled Charging	2014
Institute of Electrical and Electronic Engineers (IEEE)	P2100.1	Wireless Power and Charging Systems	2017
	C95.1	Respect to Human Exposure to Radio Frequency (3 kHz – 300 GHz) Electromagnetic Fields	2006
International Electro-mechanical Commission (IEC)	61980-1 Cor.1	EV WPT Systems Part -1: General Requirements	2017
	62827-2 Ed.1.0	WPT-Management: Part 2: Multiple Device Control Management	2017
	63,028 Ed.1.0	WPT-Air Fuel Alliance Resonant Baseline System (BSS)	2017

These standards came out recently, confirming that the topic is still under development. The most completed standard for wireless charging of EV is the SAE J2954/1. This standard defines four power charging levels, as shown in Table 3.2 [19].

Table 3.2: POWER LEVELS FROM SAE J2954/1 AND MINIMUM EFFICIENCY.

Mode	Load Power	Minimum Efficiency	Minimum Efficiency under Misalignment
WPT1	3.7 kW	85 %	80 %
WPT2	7.7 kW	85 %	80 %
WPT3	11.1 kW	85 %	80 %
WPT4	22 kW	-	-

WPT1 is for a household with a maximum power capacity of 3.7 kVW from single phase 120-V ac supply. WPT2 is for the higher power of 7.7 kW from 240-Vac mains, WPT3 upgrades this to 11.1 kW, and WPT4 to 22 kW input from a 240-V three-phase ac supply outlet. SAE J2954/2 is under development for WPT charging of heavy-duty EVs such as a bus where the power rating is between 22–150 kW and higher from a 208-Vac three phase, 480-Vac three phase, or medium voltage supply. At either level of charging, the efficiency of the system must be greater than 85% for a matched system at rated power and >80% for interoperable systems. The distance between the primary coil and a secondary coil, the magnetic gap, is classified into three Z-classes with values reported in Table 3.3.

Table 3.3: CLASSIFICATION FOR DIFFERENT TRANSMISSION DISTANCE.

Z-class	Maximum Input Apparent Power
Z1	10-15 cm
Z2	14 – 21 cm
Z3	17 – 25 cm

Concerning the human exposure to the electromagnetic field, the compliance with the International Commission on Non-Ionizing Radiation Protection (ICNIRP) directives has to be analysed. According to the standard, in the frequency range from 3 kHz to 10 MHz, the reference levels for occupational exposure to time-varying magnetic fields is 100 μT (rms), while reference level for general public exposure to time-varying magnetic fields is 27 μT (rms) [20]. The compliance to the directive of the designed system will be shown in the next chapter.

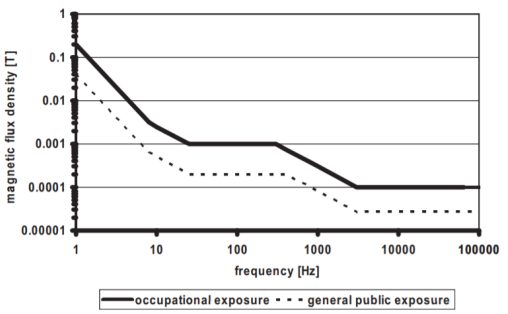

Figure 3.1: ICNIRP magnetic flux exposure limits.

3.2. Specification of the Proposed Wireless Charging System

The overall WPT architecture for EVs is shown in Figure 3.2. The power grid voltage is usually rectified to create a DC bus. Then, a power inverter converts dc voltage into high-frequency ac voltage. The power is transferred from the primary coil to the secondary using the compensating networks to reduce the reactive power and increase the transmission efficiency. Several compensations topologies will be studied in depth in the next chapter. Then, the power received on the secondary side is rectified and managed to charge the vehicle battery.

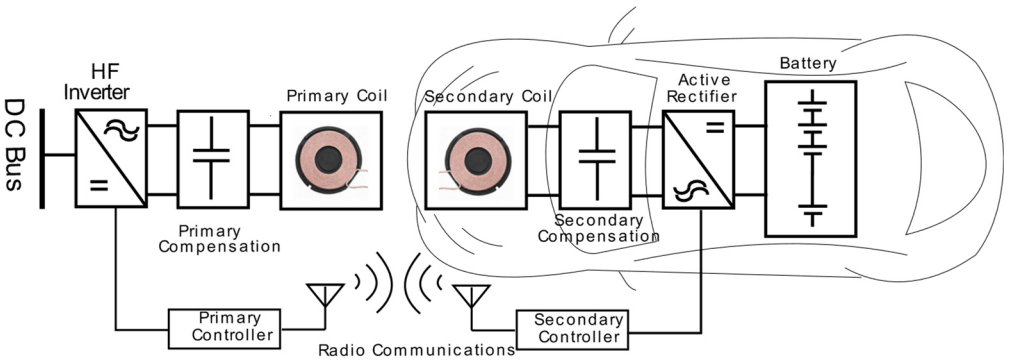

Figure 3.2: Block Diagram of a WPT system.

Another important aspect of these systems is the control strategy adopted for the coordination between primary and secondary side. Under this point of view, all the EV wireless charging systems can be classified in three way:

- Primary-side controlled systems (P-SC) [21]-[23]: the control is totally managed by the primary side. Usually the secondary consists on a full-wave passive rectifier. The disadvantage is that it is difficult to adjust the primary circuit to control multiple loads.
- Dual-side controlled systems (D-SC) [4]- [6]: the control strategy is implemented from both the primary and secondary side. It represents the most expensive solution in terms of cost and complexity. It usually requires a RF wireless communication between primary and secondary. Anyway, thanks to the higher number of degrees of freedom available for the control, it ensures the highest performance.
- Secondary-side controlled systems (S-SC) [27]-[29]: the control is totally managed from the secondary side. The primary inverter impresses a high frequency voltage to the resonant tank. Then, the power delivered to the secondary coil is managed from a dc-dc converter in order to charge the battery. Thus, the control strategy is only on the secondary side. This solution represents the most economical, but a complex control strategy is required to obtain good performance.

In [30] a comparison between primary side controlled and secondary side controlled systems are studied. Results show that secondary side system can reach higher system efficiency under the same operating conditions.

In this project, the attention is focused on a secondary side controlled system for several reasons. Firstly, it is a low-cost solution, fundamental aspect in the automotive sector. Then, this project is focused on the realization of an on-board device able to receive the power from the secondary coil and manage it to charge the EV battery with a simultaneous maximization of the transmission efficiency. All of these operations have to be made independently from the primary characteristics and without any RF communications.

The other system constraints are summarized in Table 3.4.

Table 3.4: PROPOSED SYSTEM COSTRAINTS

Parameter	Symbol	Value
Output Power Level	P_0	3.7 kW
Distance between Coils	d	15 cm
Operating Frequency	f	85 kHz

4. Magnetic Resonant Compensations

The most important feature of an Inductive Wireless Power System (IWPS) is to work with high transmission efficiency. An IWPS consists of two coupled inductors called primary and secondary. If the primary coil is supplied by an alternating current, a time-varying magnetic field B is produced. A part of this magnetic field, according to the coupling coefficient between the coils, reaches the secondary coil and, therefore, an electro motive force is induced across the secondary coil turns. Unfortunately, non-resonant coupled inductors waste most of the energy in the form of conduction losses in the primary coil due to the high quantity of reactive power circulating in the system, also for a very short range and a large coupling [31]. In order to increase the transmission efficiency over a wider distance, the resonance phenomenon between the coil inductance and additional capacitances is usually exploited [32]-[34]. These additional capacitors are designed to create resonance between the primary and secondary coils at a specific resonant frequency; thereby, they reduce the reactive power circulating inside the circuits and can allow the transmission of real power over relatively large distances among the primary and secondary coils with increased efficiencies. Depending on the connection between the capacitors and coils, four main topologies can be identified: Series Series (SS), Series Parallel (SP), Parallel Series (PS), and Parallel Parallel (PP). In literature are also available compensations which uses an higher number of reactive components such as the LCC, S-LCC and LCC-S.

In this project the SS compensation will be used because of its better performance in terms of efficiency and output power. The comparison between the SS compensation and the others will be shown.

4.1. Assumptions

The compensations analysis is carried out under the following assumptions:

- The input voltage v_1 supplied by a DC-AC inverter is purely sinusoidal. Its RMS value is V_1 and its frequency f.
- The load R_L is purely resistive.
- The coils used to transmit the power wirelessly are represented in the form of T-model, which includes the mutual inductance defined as $M = k\sqrt{L_1 L_2}$. The self-inductance of the primary and secondary coils is L_1 and L_2, respectively.
- The parasitic resistance due to DC-resistance, proximity effect and skin effect of the primary and secondary coil is R_1 and R_2 respectively.
- The compensation C_2 is designed to resonate with the secondary self-inductance L_2 at the resonant angular frequency ω_0. The primary capacitance C_1 is chosen to cancel the imaginary part of input impedance seen from the voltage source V_1 at the resonant angular frequency ω_0.

To understand the performance of each compensation topology, the efficiency and the output power P_o for different values of operating frequency f, mutual inductance M and load resistance R_L is studied.
The numerical comparison between the topologies is carried out calibrating the components to resonate at the frequency f_0=85 kHz, at the coupling coefficient k_0=0.2 and at a load resistance R_{L0}=10 Ω. The primary and secondary self-inductance are assumed to be identical $L_1 = L_2 =$ 100 μH. The parasitic resistance of the coil is $R_1 = R_2 =$ 0.1 Ω. The power grid single-phase voltage has an RMS value of V_{grid} = 230V, thus the amplitude is $V_{grid}^{max} \approx$ 230V x 1.414 ≈ 325.2 V. This voltage is then rectified by an ideal full-wave rectifier, producing a constant voltage $V_{DC} \approx V_{grid}^{max}$. An high frequency full bridge inverter impresses a square wave voltage with 50% duty cycle between $\pm V_{DC}$. Applying the first harmonic analysis (FHA), only the contribution of the first harmonic is taken into account. Thus, the sinusoidal voltage applied to the resonant tank has a frequency f_0=85 kHz and an amplitude $V_1^{max}=4V_{DC}/\pi\approx$415V. Its RMS value is $V_1= V_1^{max}$ /1.414≈293V. Since in real application some parameters can vary, plots of the output power P_o and efficiency η for different value of load resistance R_L and coupling coefficient k are shown. Concerning the frequency, in this project it is assumed to be constant to f_0=85 kHz, as explained before.

4.2. Series-Series Compensation

The electric circuit of a Series Series (SS) compensation is shown in Fig. 4.1. It is made up from a primary capacitance C_1 connected in series with the primary inductor L_1. On the secondary side the inductance L_2 is connected in series with the secondary capacitance C_2 and the load resistance R_L.

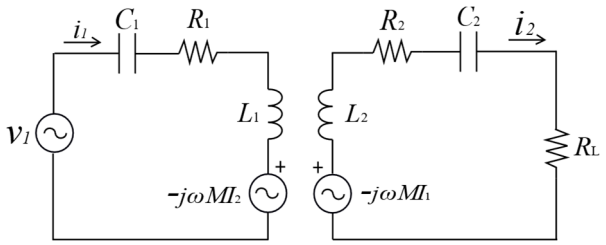

Figure 4.1: SS compensation topology.

Writing the Kirchhoff's voltage law (KVL), and representing them with matrix formulation one obtains

$$\begin{bmatrix} V_1 \\ 0 \end{bmatrix} = \begin{bmatrix} R_1 + j\left(\omega L_1 - \dfrac{1}{\omega C_1}\right) & -j\omega M \\ -j\omega M & R_L + R_2 + j\left(\omega L_2 - \dfrac{1}{\omega C_2}\right) \end{bmatrix} \begin{bmatrix} I_1 \\ I_2 \end{bmatrix} \tag{13}$$

where V_1 is the phasor input voltage, and I_1 and I_2 are the primary and secondary current phasor RMS module, ω is the operating angular frequency of the circuit, R_1 is the parasitic resistance of the primary coil and R_2 is the resistance of the secondary coil.

Inverting (13), the expressions of primary and secondary current phasors are

$$I_1 = \frac{R_2 + R_L + j\left(\omega L_2 - \dfrac{1}{\omega C_2}\right)}{\left[R_1 + j\left(\omega L_1 - \dfrac{1}{\omega C_1}\right)\right]\left[R_2 + R_L + j\left(\omega L_2 - \dfrac{1}{\omega C_2}\right)\right] + \omega^2 M^2} V_1 \tag{14}$$

$$I_2 = \frac{-j\omega M}{\left[R_1 + j\left(\omega L_1 - \dfrac{1}{\omega C_1}\right)\right]\left[R_2 + R_L + j\left(\omega L_2 - \dfrac{1}{\omega C_2}\right)\right] + \omega^2 M^2} V_1 \tag{15}$$

Thus, the ratio between primary and secondary current is

$$\frac{I_1}{I_2}=\frac{R_2+R_L+j\left(\omega L_2-\frac{1}{\omega C_2}\right)}{-j\omega M}=\frac{1}{\omega M}\left[-\left(\omega L_2-\frac{1}{\omega C_2}\right)+j\left(R_2+R_L\right)\right] \tag{16}$$

The efficiency of the series-series compensation circuit can be calculated as

$$\eta=\frac{R_L\left|I_2\right|^2}{R_L\left|I_2\right|^2+R_2\left|I_2\right|^2+R_1\left|I_1\right|^2}=\frac{R_L}{R_L+R_2+R_1\frac{\left|I_1\right|^2}{\left|I_2\right|^2}}=\frac{R_L}{R_L+R_2+\frac{R_1}{\omega^2M^2}\left[\left(\omega L_2-\frac{1}{\omega C_2}\right)^2+\left(R_2+R_L\right)^2\right]} \tag{17}$$

4.2.1. Compensation Design

The secondary capacitance C_2 is chosen to resonate with the secondary coil at the resonant frequency $f_0=\omega_0/2\pi$, thus

$$C_2=\frac{1}{\omega_0^{\,2}L_2} \tag{18}$$

The impedance seen by the source V_1 is

$$Z_{in}=R_{in}+jX_{in}=R_1+j\omega L_1-\frac{j}{\omega C_1}+\frac{M^2\omega^2}{j\omega L_2-\frac{j}{\omega C_2}+R_2+R_L} \tag{19}$$

Neglecting the parasitic resistance of the primary and secondary coils, the value of C_1 that cancel the imaginary part of the input impedance X_{in} at the resonance frequency ω_0 is

$$C_1=\frac{1}{\omega_0^{\,2}L_1} \tag{20}$$

Thus, the SS compensation expressions of the efficiency and output power are

$$\eta=\frac{R_L}{R_L+R_2+\frac{R_1}{\omega_0^2M^2}\left(R_2+R_L\right)^2} \tag{21}$$

$$P_o=R_L\left(\frac{V_1\omega M}{R_1\left(R_2+R_L\right)+\omega^2M^2}\right)^2 \tag{22}$$

In the next sections, the optimum values of mutual inductance M, angular frequency ω and load resistance R_L which maximize the output power and the transmission efficiency for the SS compensation are studied.

4.2.2. **Dependence from Mutual Inductance *M***

In order to understand how the mutual inductance affects the efficiency, the derivative is studied.

$$\frac{\partial \eta}{\partial M} = \eta' = \frac{2R_L R_1 \left(\frac{R_2 + R_L}{\omega} \right)^2 M}{\left\{ \left[\left(R_2 + R_L \right) M^2 \right] + \left[R_1 \left(\frac{R_2 + R_L}{\omega_0} \right)^2 \right] \right\}} \tag{23}$$

The value of mutual inductance which maximize the efficiency, i.e. $M: \frac{\partial \eta}{\partial M} = 0$ is $M = 0$, with $R_1 \left(\frac{R_2 + R_L}{\omega} \right)^2 \neq 0$. This mean that the efficiency increases as the mutual inductance increase. The same approach is used to understand the dependence of the output power from the mutual inductance

$$\frac{\partial P_o}{\partial M} = \frac{2\omega V_i M \left[R_1 \left(R_2 + R_L \right) - \omega^2 M^2 \right]}{\left[R_1 \left(R_2 + R_L \right) + \omega^2 M^2 \right]^3} \tag{24}$$

Imposing $M: \frac{\partial P_o}{\partial M} = 0$, one obtains the following solutions:

$$M_1 = 0, \quad R_1 \left(R_2 + R_L \right) \neq 0 \tag{25}$$

$$M_2 = -\sqrt{\frac{R_1 \left(R_2 + R_L \right)}{\omega^2}}, \quad \omega \neq 0, \; R_1 \left(R_2 + R_L \right) \neq 0 \tag{26}$$

$$M_3 = \sqrt{\frac{R_1 \left(R_2 + R_L \right)}{\omega^2}}, \quad \omega \neq 0, \; R_1 \left(R_2 + R_L \right) \neq 0 \tag{27}$$

The only one usable solution is M_3. If the load resistance R_L, the angular frequency ω and the parasitic component of the coils R_1 and R_2 are known, this information can be used to know the distance at which the output power is maximized.

4.2.3. **Dependence from Operating Frequency *f***

According to (17), the expression of the efficiency as a function of the angular frequency is

$$\eta(\omega)=\frac{N(\omega)}{D(\omega)}=\frac{\omega^4 C_2^2 M^2 R_L}{\omega^4 C_2^2\left[M^2 R+L_2^2 R_1\right]+\omega^2 R_1\left[C_2^2 R^2-2L_2 C_2\right]+R_1} \tag{28}$$

Its derivate is studied in order to understand the value of ω which maximize η, thus

$$\eta'(\omega)=\frac{N'(\omega)D(\omega)-N(\omega)D'(\omega)}{D^2(\omega)}=\frac{2\omega^3 C_2^2 M^2 R_1 R_L\left[\omega^2\left[C_2^2 R^2-2L_2 C_2\right.\right.}{D^2(\omega)} \tag{29}$$

The solution of the equation $\eta'(\omega)=0$ that $\omega \in \mathbb{R}$, $\omega > 0$ represents the value which maximizes the efficiency. After many calculations one obtain

$$\omega^{\eta_{\max}}=\sqrt{-\frac{2}{C_2^2 R^2-2L_2 C_2}} \tag{30}$$

Being the secondary capacitance C_2 designed to resonate with the secondary inductance L_2 at the resonant frequency ω_0, i.e.

$$L_2 C_2 = L_2\frac{1}{\omega_0^2 L_2}=\frac{1}{\omega_0^2} \tag{31}$$

The expression of $\omega^{\eta max}$ can be written

$$\omega^{\eta_{\max}}=\sqrt{\frac{1}{\frac{1}{\omega_0^2}-\frac{1}{2}R^2 C_2^2}} \tag{32}$$

Being $\frac{1}{\omega_0^2} \gg \frac{1}{2}R^2 C_2^2$, thus $\omega^{\eta_{\max}}=\omega_0$

4.2.4 Dependence of Efficiency from C_2

The expression of the efficiency as a function of C_2 is

$$\eta = \frac{N(C_2)}{D(C_2)} = \frac{C_2^2 \omega^4 M^2 R_L}{C_2^2\left[\omega^4 M^2 R + \omega^4 L_2^2 R_1 + \omega^2 R^2 R_1\right] - 2C_2\omega^2 L_2 R_1 + R_1} \tag{33}$$

The derivate of η is

$$\eta' = \frac{-2\omega^4 M^2 R_L R_1 C_2\left[C_2\omega^2 L_2 - 1\right]}{D^2(C_2)} \tag{34}$$

The value of C_2 which maximize the efficiency is

$$C_2 = \frac{1}{\omega^2 L_2} \tag{35}$$

4.2.5 Dependence of Efficiency from R_L

The expression of the efficiency as a function of the load resistance is

$$\eta(R_L) = \frac{N(R_L)}{D(R_L)} = \frac{R_L\omega^2 M^2 C_2^2}{C_2^2 R_1 R_L + C_2^2\left[\omega^2 M^2 + 2R_1 R_2\right]R_L + \omega^2 C_2^2\left[M^2 R_2 + L_2^2 R_1\right] + C_2 R_1\left[C_2 R_2^2 - 2L_2\right] + \frac{R_1}{\omega^2}} \tag{36}$$

The derivate is

$$\eta'(R_L) = \frac{-\omega^2 M^2 C_2^4 R_1 R_L^2 + M^2 C_2^2\left\{C_2^2\omega^4\left[M^2 R_2 + L_2^2 R_1\right] + \omega^2 C_2 R_1\left[C_2 R_2^2 - 2L_2\right.\right.}{\omega^2 M^2 C_2^2 R_1} \tag{37}$$

Thus, the value of load resistance which maximize the efficiency is

$$R_L^\eta = \sqrt{\frac{\omega^4 C_2^2\left[M^2 R_2 + L_2^2 R_1\right] + \omega^2 C_2 R_1\left[C_2 R_2^2 - 2L_2\right] + R_1}{\omega^2 C_2^2 R_1}} \tag{38}$$

If the system is designed to work in resonance, i.e. $C_2 = 1/(\omega_0^2 L_2)$, the expression of the load resistance can be simplified as

$$R_L^\eta = R_2\sqrt{1 + \frac{\omega^2 M^2}{R_1 R_2}} \tag{39}$$

The output power P_0 is a function of the load resistance R_L

$$P_0 = R_L\left(\frac{V_1\omega M}{R_1\left(R_2+R_L\right)+\omega^2M^2}\right)^2 = \frac{R_LV_1^2\omega^2M^2}{R_L^2R_1^2+R_L\left(2\omega^2M^2R_1+2R_1^2R_2\right)+\omega^4M^4+2\omega^2M^2R_1R_2+R_1^2R_2^2} \tag{40}$$

$$\frac{\partial P_0}{\partial R_L} = \frac{N^{'}(R_L)D(R_L)-N(R_L)D^{'}(R_L)}{D^2(R_L)} = \frac{V_i^2M^2\omega R_1^2R_2^2}{\left[R_1^2R_L^2+R_L\left(2\omega^2M^2R_1+2R_1^2R_2\right)+\omega^4M^4+2\omega^2M^2R_1R_2+R_1^2R_2^2\right]^2} \tag{41}$$

Thus, the output power increase as the load resistance increases. From (15) it is possible to note that if the parasitic resistances are neglected R_1=R_2=0 and the system operate in resonance, the output current I_2 is approximately independent from the load resistance R_L. Thus, under this operating condition, the output power increase approximately linearly as the load resistance R_L increase.

4.3 Series-Parallel Compensation

The Series-Parallel (SP) compensation topology is shown in Figure 4.2. It consists on a primary capacitance C_1 connected in series with the primary coil L_1. The secondary coil L_2 is connected in parallel with the secondary capacitance C_2 and the load resistance R_L.

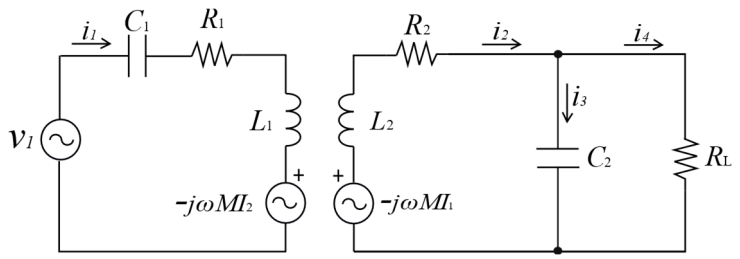

Figure 4.2: SP compensation topology.

Applying Kirchhoff's voltage law (KVL) for the circuit in Figure 42, one obtains

$$\begin{bmatrix} V_1 \\ 0 \\ 0 \end{bmatrix} = \begin{bmatrix} R_1 + j\left(\omega L_1 - \dfrac{1}{\omega C_1}\right) & -j\omega M & 0 \\ -j\omega M & R_2 + j\left(\omega L_2 - \dfrac{1}{\omega C_2}\right) & \dfrac{j}{\omega C_2} \\ 0 & \dfrac{j}{\omega C_2} & R_L - \dfrac{j}{\omega C_2} \end{bmatrix} \begin{bmatrix} I_1 \\ I_2 \\ I_4 \end{bmatrix} \tag{42}$$

Inverting (42), the analytical expressions of the primary and secondary currents are obtained as follows

$$I_1 = \frac{\left(R_L - j\dfrac{1}{\omega C_2}\right)\left[R_2 + j\left(\omega L_2 - \dfrac{1}{\omega C_2}\right)\right] + \dfrac{1}{\omega^2 C_2}}{\dfrac{1}{\omega^2 C_2^2}\left[R_1 + j\left(\omega L_1 - \dfrac{1}{\omega C_1}\right)\right] + \left(R_L - j\dfrac{1}{\omega C_2}\right)\left\{\omega^2 M^2 + \left[R_1 + j\left(\omega L_1 - \dfrac{1}{\omega C_1}\right)\right]\left[R_2 + j\left(\omega L_2 - \dfrac{1}{\omega C_2}\right)\right]\right\}} V_1 \tag{43}$$

$$I_2 = \frac{-\dfrac{M}{C_2} - j\omega M R_L}{\dfrac{1}{\omega^2 C_2^2}\left[R_1 + j\left(\omega L_1 - \dfrac{1}{\omega C_1}\right)\right] + \left(R_L - j\dfrac{1}{\omega C_2}\right)\left\{\omega^2 M^2 + \left[R_1 + j\left(\omega L_1 - \dfrac{1}{\omega C_1}\right)\right]\left[R_2 + j\left(\omega L_2 - \dfrac{1}{\omega C_2}\right)\right]\right\}} V_1 \tag{44}$$

$$I_4 = \frac{\dfrac{M}{C_2}}{\dfrac{1}{\omega^2 C_2^2}\left[R_1 + j\left(\omega L_1 - \dfrac{1}{\omega C_1}\right)\right] + \left(R_L - j\dfrac{1}{\omega C_2}\right)\left\{\omega^2 M^2 + \left[R_1 + j\left(\omega L_1 - \dfrac{1}{\omega C_1}\right)\right]\left[R_2 + j\left(\omega L_2 - \dfrac{1}{\omega C_2}\right)\right]\right\}} V \tag{45}$$

Thus, the ratio between the input and output currents are

$$\frac{I_1}{I_4} = \frac{1}{M}\left\{\left[L_2 + C_2 R_L R_2\right] + j\left[R_L C_2\left(\omega L_2 - \frac{1}{\omega C_2}\right) - \frac{R_2}{\omega}\right]\right\} \tag{46}$$

$$\frac{I_2}{I_4} = 1 + j\omega R_L C_2 \tag{47}$$

The overall efficiency can be calculated as

$$\eta = \frac{R_L |I_4|^2}{R_L |I_4|^2 + R_1 |I_1|^2 + R_2 |I_2|^2} = \frac{R_L}{R_L + R_2\left[1 + (\omega R_L C_2)^2\right] + \frac{R_1}{M^2}\left\{(L_2 + C_2 R_L R_2)^2 + \left[R_L C_2\left(\omega L_2 - \frac{1}{\omega C_2}\right) - \frac{R_2}{\omega}\right]^2\right\}} \tag{48}$$

4.3.1 Compensation Design

The secondary capacitance C_2 is chosen to resonate with the secondary coil at the resonance frequency $f_0=\omega_0/2\pi$, thus

$$C_2 = \frac{1}{\omega_0^2 L_2} \tag{49}$$

The impedance seen from the source V_1 is

$$Z_{in} = R_{in} + jX_{in} = R_1 - \frac{j}{\omega C_1} + j\omega L_1 + \frac{M^2\omega^2}{R_2 + \frac{R_L}{1 + j\omega C_2 R_L} + j\omega L_2} \tag{50}$$

Neglecting the parasitic resistance of the primary and secondary coils, the value of C_1 that cancels the imaginary part of the input impedance X_{in} at the resonant frequency ω_0 is

$$C_1 = \frac{L_2^2 C_2}{L_1 L_2 - M^2} = \frac{1}{\omega_0^2\left(L_1 - \frac{M^2}{L_2}\right)} \tag{51}$$

4.4 Parallel-Series Compensation

The Parallel Series (PS) compensation topology is shown in Figure 4.3. The primary capacitance C_1 is connected in parallel with the voltage source V_1 and the primary inductance L_1. As in the SS compensation, on the secondary side, the capacitor C_2 is connected in series with both the load resistance R_L and secondary inductance L_2.

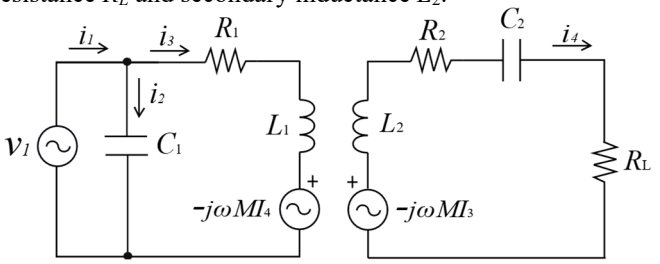

Figure 4.3: PS compensation topology.

Applying Kirchhoff's voltage law (KVL) to the circuit in Fig. 4.3 and representing them in matrix form, one obtains

$$\begin{bmatrix} V_i \\ 0 \\ 0 \end{bmatrix} = \begin{bmatrix} -\frac{j}{\omega C_1} & \frac{j}{\omega C_1} & 0 \\ \frac{j}{\omega C_1} & R_1 + j\left(\omega L_1 - \frac{1}{\omega C_1}\right) & -j\omega M \\ 0 & -j\omega M & R_2 + R_L + j\left(\omega L_2 - \frac{1}{\omega C_2}\right) \end{bmatrix} \begin{bmatrix} I_1 \\ I_3 \\ I_4 \end{bmatrix} \tag{52}$$

Inverting this relationship, analytical expressions of the primary and secondary current are derived

$$I_1 = j\omega C_1 \frac{\omega^2 M^2 + \left[R_1 + j\left(\omega L_1 - \frac{1}{\omega C_1}\right)\right]\left[R_L + R_2 + j\left(\omega L_2 - \frac{1}{\omega C_2}\right)\right]}{\omega^2 M^2 + \left(R_1 + j\omega L_1\right)\left[R_L + R_2 + j\left(\omega L_2 - \frac{1}{\omega C_2}\right)\right]} V_1 \tag{53}$$

$$I_3 = \frac{R_2 + R_L + j\left(\omega L_2 - \frac{1}{\omega C_2}\right)}{\omega^2 M^2 + \left(R_1 + j\omega L_1\right)\left[R_L + R_2 + j\left(\omega L_2 - \frac{1}{\omega C_2}\right)\right]} V_1 \tag{54}$$

$$I_4 = \frac{-j\omega M}{\omega^2 M^2 + \left(R_1 + j\omega L_1\right)\left[R_L + R_2 + j\left(\omega L_2 - \frac{1}{\omega C_2}\right)\right]} V_1 \tag{55}$$

Thus, the ratio of the two currents is

$$\frac{I_3}{I_4} = \frac{1}{\omega M}\left\{\left(\omega L_2 - \frac{1}{\omega C_2}\right) - j\left(R_2 + R_L\right)\right\} \tag{56}$$

$$\frac{I_3}{I_4} = \frac{1}{\omega M}\left\{\left(\omega L_2 - \frac{1}{\omega C_2}\right) - j\left(R_2 + R_L\right)\right\} \tag{57}$$

The efficiency can be determined as

$$\eta = \frac{R_L\left|I_4\right|^2}{R_L\left|I_4\right|^2 + R_1\left|I_1\right|^2 + R_2\left|I_3\right|^2} = \frac{R_L}{R_L + R_2 + \frac{R_1}{\omega^2 M^2}\left\{\left[\left(\omega L_2 - \frac{1}{\omega C_2}\right)^2 + \left(R_L + R_2\right)^2\right]\right\}} \tag{58}$$

4.4.1 Compensation Design

The secondary capacitance C_2 is chosen to resonate with the secondary coil at the resonance frequency $f_0=\omega_0/2\pi$, thus

$$C_2 = \frac{1}{\omega_0{}^2 L_2} \tag{59}$$

The impedance seen by the source V_1 is

$$Z_{in} = \frac{1}{j\omega C_1 + \dfrac{1}{R_1 + j\omega L_1 + \dfrac{\omega^2 M^2}{R_2 + R_L + j\omega L_2 - \dfrac{j}{\omega C_2}}}} \tag{60}$$

Neglecting the parasitic resistance of the primary and secondary coils, the value of C_1 that cancels the imaginary part of the input impedance at the resonant frequency ω_0 is

$$C_1 = \frac{L_1 L_2^2 R_L^2 C_2^2}{M^4 + L_1{}^2 L_2 R_L^2 C_2} = \frac{1}{\omega_0{}^2\left(L_1 + \dfrac{\omega_0^2 M^4}{L_1 R_L^2}\right)} \tag{61}$$

In the PS compensation, the primary capacitance depends on both the coupling coefficient and load resistance. Thus, to operate in resonance, the estimation of both coupling coefficient and load resistance is needed.

4.5 Parallel-Parallel Compensation

A circuit of a Parallel-Series (PS) compensation scheme is shown in Figure 4.4. The parallel-parallel compensation is achieved by using capacitor C_1 connected in parallel with the ac source, as in the parallel-series compensations. The parallel combinations of these two components is connected in series with the primary side inductor L_1. On the secondary side, capacitor C_2 is connected in parallel to load resistance R_L. The parallel combination of C_2 and R_L is connected in series with the inductance L_2 and load resistance R_L as in the series-parallel compensation circuit.

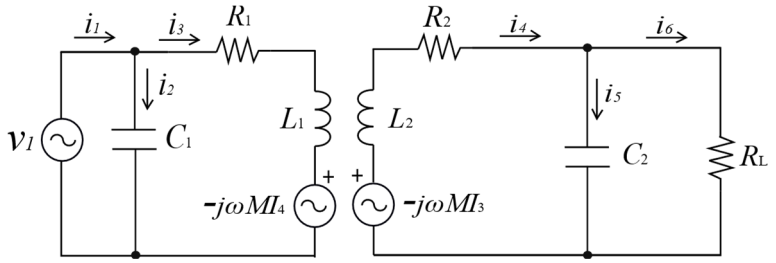

Figure 4.4: PP compensation topology.

Using Kirchhoff's voltage law (KVL) of the circuit in Figure 4.4 one obtains

$$\begin{bmatrix} V_1 \\ 0 \\ 0 \\ 0 \end{bmatrix} = \begin{bmatrix} -\frac{j}{\omega C_1} & \frac{j}{\omega C_1} & 0 & 0 \\ \frac{j}{\omega C_1} & R_1 + j\left(\omega L_1 - \frac{1}{\omega C_1}\right) & -j\omega M & 0 \\ 0 & -j\omega M & R_2 + j\left(\omega L_2 - \frac{1}{\omega C_2}\right) & \frac{j}{\omega C_2} \\ 0 & 0 & \frac{j}{\omega C_2} & R_L - \frac{j}{\omega C_2} \end{bmatrix} \begin{bmatrix} I_1 \\ I_3 \\ I_4 \\ I_6 \end{bmatrix} \tag{62}$$

Inverting the above relationship, an analytical expression for the primary and secondary currents are

$$I_1 = j\omega C_1 \frac{\omega^2 M^2 \left(\frac{j}{\omega C_2} - R_L\right) + \left[R_1 + j\left(\omega L_1 - \frac{1}{\omega C_1}\right)\right]\left\{\frac{1}{\omega^2 C_2^2} + \left[R_2 + j\left(\omega L_2 - \frac{1}{\omega C_2}\right)\left(R_L - \frac{j}{\omega C_2}\right)\right]\right\}}{\left(R_L - \frac{j}{\omega C_2}\right)\left\{\omega^2 M^2 - \left[R_2 + j\left(\omega L_2 - \frac{1}{\omega C_2}\right)\right](R_1 + j\omega L_1)\right\} - \frac{1}{\omega^2 C_2^2}(R_1 + j\omega L_1)} V_1 \tag{63}$$

$$I_3 = \frac{\frac{1}{\omega^2 C_2^2} + \left[R_2 + j\left(\omega L_2 - \frac{1}{\omega C_2}\right)\right]\left(R_L - \frac{j}{\omega C_2}\right)}{\left(\frac{j}{\omega C_2} - R_L\right)\left\{\omega^2 M^2 - \left[R_2 + j\left(\omega L_2 - \frac{1}{\omega C_2}\right)\right](R_1 + j\omega L_1)\right\} + \frac{1}{\omega^2 C_2^2}(R_1 + j\omega L_1)} V_1 \tag{64}$$

$$I_4 = \frac{\frac{M}{C_2} + j\omega M R_L}{\left(\frac{j}{\omega C_2} - R_L\right)\left\{\omega^2 M^2 - \left[R_2 + j\left(\omega L_2 - \frac{1}{\omega C_2}\right)\right]\left(R_1 + j\omega L_1\right)\right\} + \frac{1}{\omega^2 C_2^2}\left(R_1 + j\omega L_1\right)} V_1 \tag{65}$$

$$I_6 = \frac{\frac{M}{C_2}}{\left(\frac{j}{\omega C_2} - R_L\right)\left\{\omega^2 M^2 - \left[R_2 + j\left(\omega L_2 - \frac{1}{\omega C_2}\right)\right]\left(R_1 + j\omega L_1\right)\right\} + \frac{1}{\omega^2 C_2^2}\left(R_1 + j\omega L_1\right)} V_1 \tag{66}$$

Therefore, the efficiency can be calculated as

$$\eta = \frac{R_L \left|I_6\right|^2}{R_L \left|I_6\right|^2 + R_2 \left|I_4\right|^2 + R_1 \left|I_3\right|^2} = \frac{R_L}{R_L + R_2 + R_2 R^2{}_L \omega^2 C_2^2 + \frac{R_1}{M^2}\left\{\left(R_2 C_2 R_L + L_2\right)^2 + \left[\frac{R_L}{\omega} + R_2 - R_L L_2 \omega C_2\right]^2\right\}} \tag{67}$$

4.5.1 Compensation Design

The secondary capacitance C_2 is chosen to resonate with the secondary coil at the resonance frequency $f_0=\omega_0/2\pi$, thus

$$C_2 = \frac{1}{\omega_0{}^2 L_2} \tag{68}$$

The impedance seen by the source V_1 is

$$Z_{in} = \cfrac{1}{j\omega C_1 + \cfrac{1}{R_1 + j\omega\left(L_1 - M\right) + \cfrac{1}{\cfrac{1}{j\omega M} + \cfrac{1}{R_2 + j\omega\left(L_2 - M\right) + \cfrac{1}{j\omega C_2 + \cfrac{1}{R_L}}}}}} \tag{69}$$

Neglecting the parasitic resistance of the primary and secondary coils, the value of C_1 that cancels the imaginary part of the input impedance at the resonant frequency ω_0 is

$$C_1 = \frac{1}{\omega_0^2\left[\left(L_1 - \frac{M^2}{L_2}\right)^2 + \frac{\frac{M^4 R_L^2}{L_2^4}}{\omega_0^2\left(L_1 - \frac{M^2}{L_2}\right)}\right]} \tag{70}$$

As in the SP, also for the PP compensation the primary capacitance has to be calculated from the mutual inductance and the load resistance in order to operate in resonance.

4.6 Comparison between SS, SP, PS, PP

Under the conditions shown in section 4.1, the output power and efficiency comparison varying the mutual inductance, load resistance and operating frequency are shown in Figure4.5.

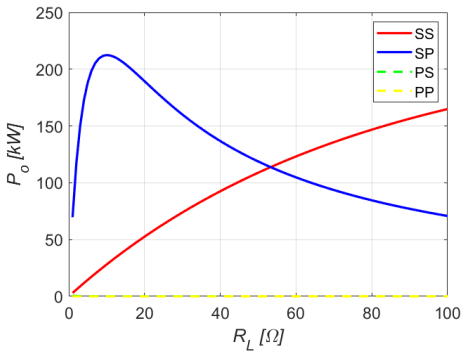

(a)

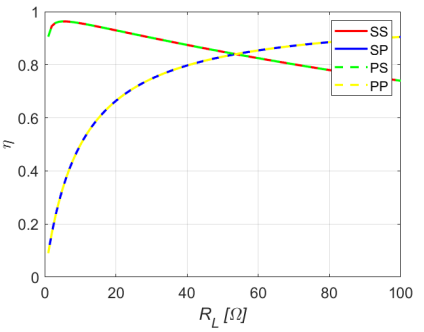

(b)

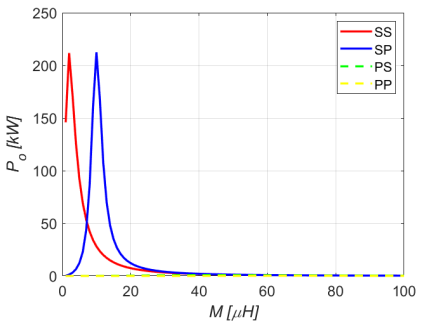

(c)

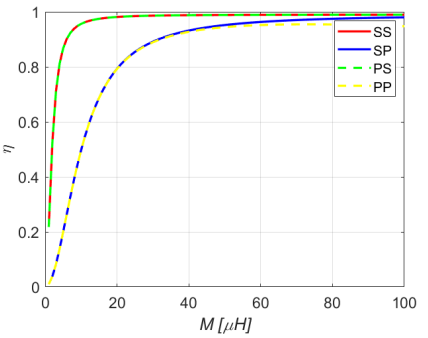

(d)

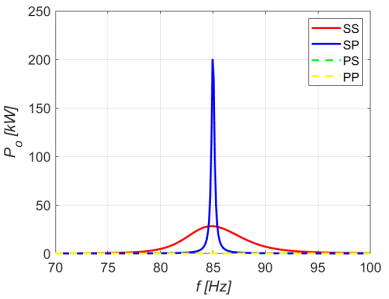

(e)

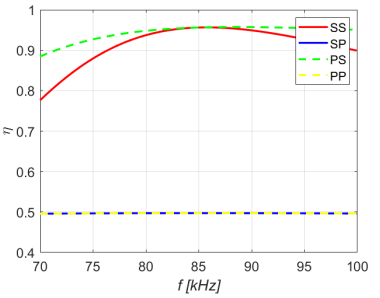

(e)

Figure 4.5: Output power P_0 and efficiency η comparison between SS, SP, PS, PP.

From the results in Figure 4.5, the PS and PP compensation are discarded for this application because of their worst performance compared with the other two. As shown in Figure 4.5(a), the SS and SP compensations have an opposite behavior as the load resistance changes. The SS compensation, working as independent current source at the output, increases the output power as the load resistance increases. On the other hand, the SP decreases the output current as the load resistance increases. Concerning the behavior under mutual inductance variation, it is possible noticed that the SP compensation has its maximum output power at the nominal value of mutual inductance M=10μH, as shown in Figure 4.5(c). This is due to the dependence of the primary capacitance on the mutual inductance, as shown in Figure 4.6. The SS compensation exhibits better performance for lower coupling coefficient. Finally, concerning the behavior under frequency variations, both SS and SP has the maximum output power and efficiency at the resonant frequency f=85kHz.

Table 4.1: COMPARISON BETWEEN RESONANT COMPENSATIONS.

	SS	**SP**	**PS**	**PP**
Primary Capacitance	$C_1 = \frac{1}{\omega_0^2 L_1}$	$C_1 = \frac{1}{\omega_0^2\left(L_1 - \frac{M^2}{L_2}\right)}$	$C_1 = \frac{1}{\omega_0^2\left(L_1 + \frac{\omega_0^2 M^2}{L_1 R_L^2}\right)}$	$C_1 = \frac{1}{\omega_0^2\left[\left(L_1 - \frac{M^2}{L_2}\right)^2 + \frac{\frac{M^2 R_L^2}{L_2^4}}{\omega_0^2\left(L_1 - \frac{M^2}{L_2}\right)}\right]}$
Dependence from R_L	NO	NO	YES	YES
Dependence from M	NO	YES	YES	YES

As shown in Table 4.1, the primary capacitance of the SS compensation depends only on the primary inductance and the resonant frequency. As explained in Section 3.2, in this project the operating frequency is assumed to be constant to the resonant frequency. Under this condition, that the SS compensation can works in resonance independently from load and mutual inductance variation. Thus, the SS compensation exhibits the best performance compared with the others.

In the next sections also the LCC, S-LCC and LCC-S will be analyzed and compared with the SS compensation.

4.7 LCC Compensation

The LCC compensation is made up from an L_{f1}-C_{f1} filter inductor L_{f1} connected in series with the voltage source v_1. Two capacitance C_1 and C_2 are connected in series respectively with two inductance L_1 and L_2. At the output another L_{f2}-C_{f2} filter is used.

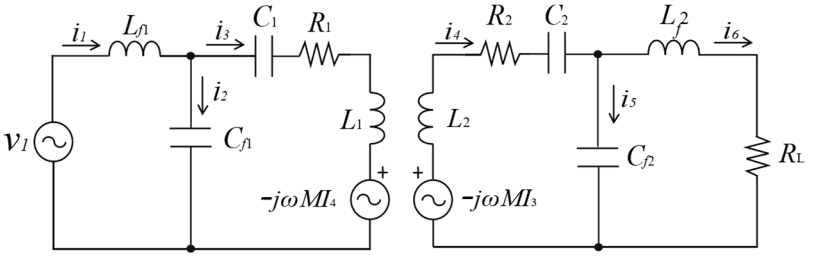

Figure 4.6: LCC Compensation topology.

Using Kirchhoff's voltage law (KVL) of the circuit in Figure 4.6, one obtains

$$\begin{bmatrix} V_1 \\ 0 \\ 0 \\ 0 \end{bmatrix} = \begin{bmatrix} j\left(\omega L_{f1} - \frac{1}{\omega C_{f1}}\right) & \frac{j}{\omega C_{f1}} & 0 & 0 \\ \frac{j}{\omega C_{f1}} & R_1 + j\left(\omega L_1 - \frac{1}{\omega C_1} - \frac{1}{\omega C_{f1}}\right) & -j\omega M & 0 \\ 0 & -j\omega M & R_2 + j\left(\omega L_2 - \frac{1}{\omega C_2} - \frac{1}{\omega C_{f2}}\right) & \frac{j}{\omega C_{f2}} \\ 0 & 0 & \frac{j}{\omega C_{f2}} & R_L + j\left(\omega L_{f2} - \frac{1}{\omega C_{f2}}\right) \end{bmatrix} \begin{bmatrix} I_1 \\ I_3 \\ I_4 \\ I_6 \end{bmatrix} \tag{71}$$

4.7.1 Compensation Design

The LCC compensation has multiple frequencies. Defining with ω_0 the resonant frequency, the system works in resonance if input voltage v1 and current i1 are in phase, leading to a zero reactance of the input impedance. In [31], the condition to work under this condition is shown, and it is represented by the following equations

$$L_{f1} \cdot C_{f1} = L_{f2} \cdot C_{f2} = \frac{1}{\omega_0^2} \tag{72}$$

$$L_1 - L_{f1} = \frac{1}{\omega_0^2 C_1} \tag{73}$$

$$L_2 - L_{f2} = \frac{1}{\omega_0^2 C_2} \tag{74}$$

Studying the circuit topology and manipulation (71), the expression of the efficiency under resonance operations is

$$\eta = \frac{R_L}{R_L + R_1 \frac{C_{f2}^2}{M^2}\left(R_2 R_L + \frac{1}{\omega^2 C_{f2}^2}\right)^2 + R_2 \omega^2 R_L^2 C_{f2}^2} \tag{75}$$

4.8 S-LCC Compensation

The S-LCC compensation topology is shown in Figure 4.7.

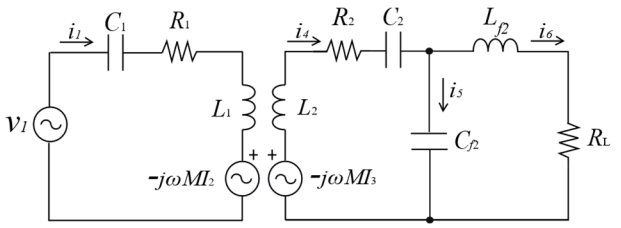

Figure 4.7: S-LCC Compensation topology.

Applying the Kirchhoff's voltage law (KVL) to the circuit in Figure 4.8, one obtains

$$\begin{bmatrix} V_1 \\ 0 \\ 0 \end{bmatrix} = \begin{bmatrix} R_1 + j\left(\omega L_1 - \dfrac{1}{\omega C_1}\right) & -j\omega M & 0 \\ -j\omega M & j\left(\omega L_2 - \dfrac{1}{\omega C_2} - \dfrac{1}{\omega C_{f2}}\right) & j\dfrac{1}{\omega C_{f2}} \\ 0 & j\dfrac{1}{\omega C_{f2}} & R_L + j\left(\omega L_{f2} - \dfrac{1}{\omega C_{f2}}\right) \end{bmatrix} \begin{bmatrix} I_1 \\ I_2 \\ I_4 \end{bmatrix} \tag{76}$$

After many manipulations, if the system is designed following this approach, the efficiency under resonance operations is

$$\eta = \frac{R_L}{R_L + R_1\left(\dfrac{1}{\omega^2 M C_{f2}}\right)^2 + R_2\left(R_L C_{f2}\right)^2} \tag{77}$$

4.9 LCC-S Compensation

The LCC-S compensation is shown in Fig.4.8.

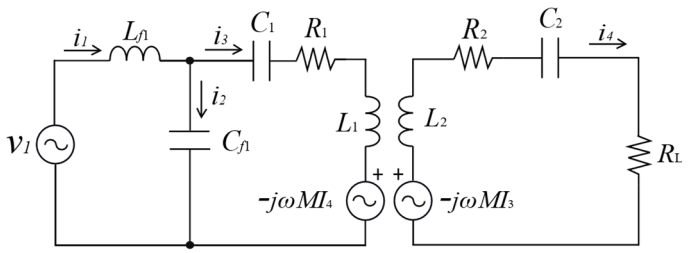

Figure 4.8: LCC-S Compensation Topology.

Using Kirchhoff's voltage law (KVL) of the circuit in Figure 4.8, results in the voltage in the matrix form as

$$\begin{bmatrix} V_1 \\ 0 \\ 0 \end{bmatrix} = \begin{bmatrix} j\left(\omega L_{f1} - \dfrac{1}{\omega C_{f1}}\right) & \dfrac{j}{\omega C_{f1}} & 0 \\ \dfrac{j}{\omega C_{f1}} & R_1 + j\left(\omega L_1 - \dfrac{1}{\omega C_1} - \dfrac{1}{\omega C_{f1}}\right) & -j\omega M \\ 0 & -j\omega M & R_L + j\left(\omega L_2 - \dfrac{1}{\omega C_2}\right) \end{bmatrix} \begin{bmatrix} I_1 \\ I_3 \\ I_4 \end{bmatrix} \tag{78}$$

After many manipulations, if the system is designed following this approach, the expression of the efficiency under resonance operations is

$$\eta = \frac{R_L}{R_L + R_2 + \dfrac{R_1 R_L^2}{\omega^2 M^2}} \tag{79}$$

4.10 Comparison between SS, LCC, S-LCC, LCC-S

Under the conditions shown in section 4.1, the output power and efficiency comparison varying the mutual inductance, load resistance and operating frequency are shown in Figure4.9.

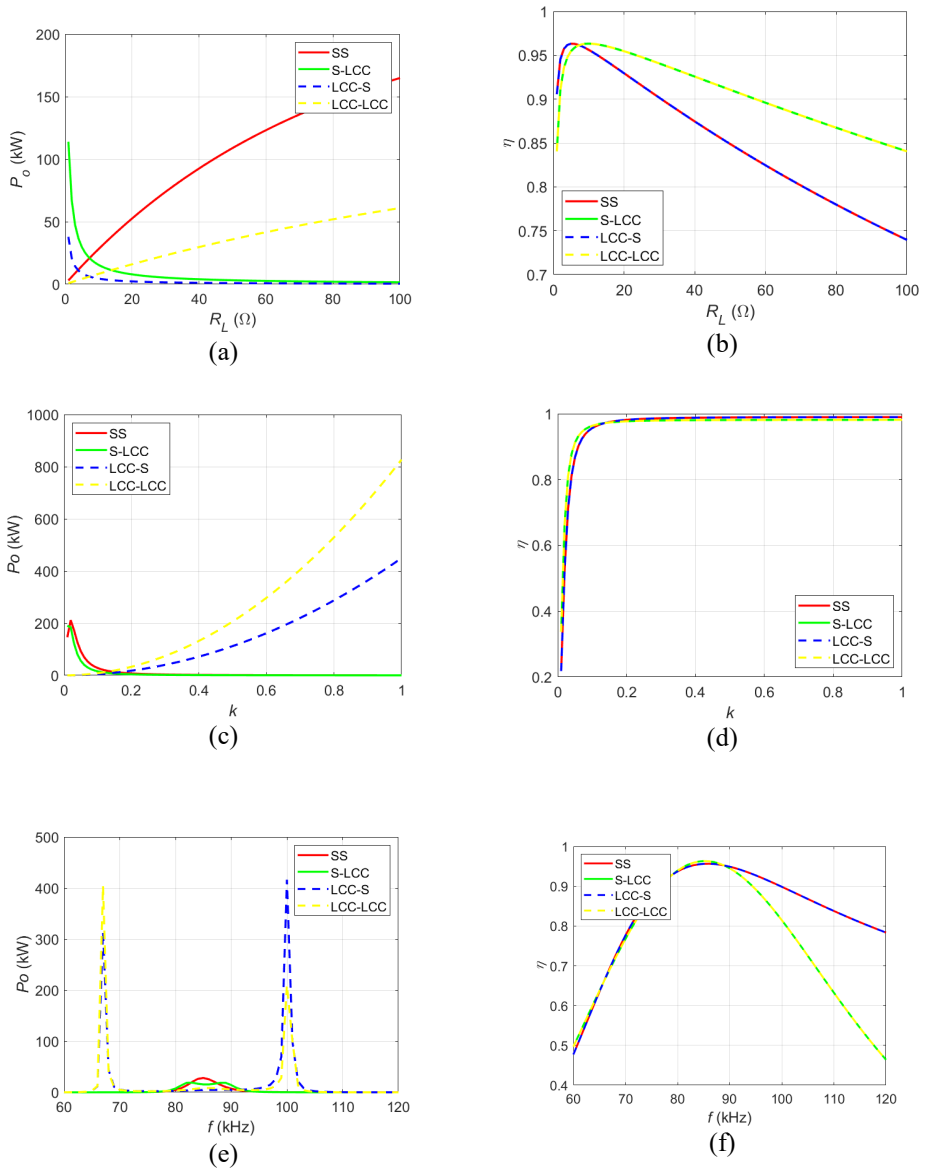

Figure 4.9: Output power and efficiency comparison SS, LCC, S-LCC, LCC-S.

As shown in Figure 4.9(a), the SS and LCC compensation increase the output power as the load resistance increases. An opposite behavior is exhibited from the S-LCC and LCC-S, reducing the output power as the load resistance increases. For all the compensations, when the transmission efficiency increases as the coupling coefficient increases. Concerning the frequency variations, the compensations exhibits the maximum efficiency when they are working at the resonant frequency f=85 kHz. The SS compensation exhibits also the maximum power transfer at the resonant frequency, while the other compensation is characterized from the bifurcation behavior, splitting the maximum power transfer at two different frequencies.

As shown in Figure 4.9, the SS and the LCC compensation increase the output power as the load resistance increases. Otherwise, the S-LCC and the LCC-S exhibits the opposite behavior: the output power decreases as the load resistance increases. For all the compensations, the transmission efficiency increase as the mutual inductance increases, because of magnetic leakage flux reduction. The power transmission efficiency is also maximized at the resonant frequency, as shown in Figure 4.9(f).

The SS compensation exhibits the best performance compared with the other compensations. Furthermore, the SS compensation has the advantage of using a smaller number of resonance components than the LCC, LCC-S and S-LCC. This leads to an economic savings, a particularly important aspect in the automotive sector. For this reason, the SS compensation is used in this project.

5. Circular Coil Geometry Optimization

5.1. Coil Overview

Without the direct contact between vehicle and charger, the coil geometry plays a key role for the system performance. The size, the shape, the materials and the locations greatly affect the transmission efficiency and the power level of the charger. For this reason, several studies have been made trying to reduce costs still ensuring high performance.

In [32] an overview concerning the coils geometry is shown. The chronology is shown in Figure 5.1, showing the new pad that have been introduced over time.

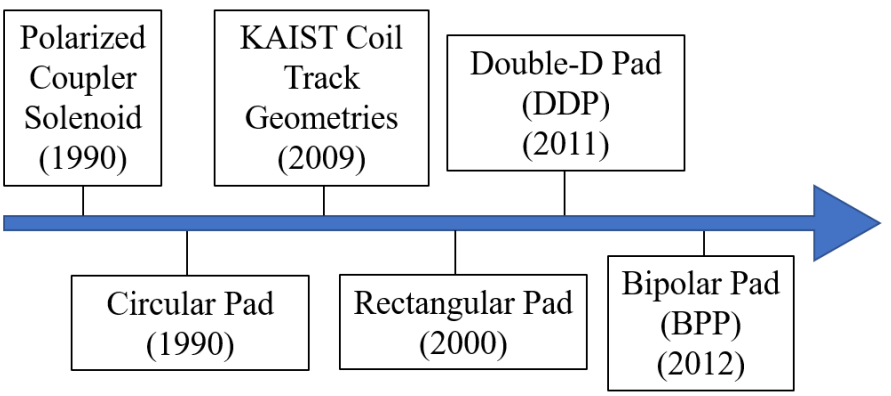

Figure 5.1: Chronology of Charging PAD for EV charging.

The *solenoid pad* (also known as *Flux Pipe* pad), was developed and used in the 90's for monorail automatic guided vehicle applications [33]. In general, the name polarized pad is used when a north and a south pole is present. It is created by wrapping a flat coil around a flat ferrite structure, as shown in Figure 5.2 (a). They allow smaller and lighter size and more tolerance of misalignment. Depending on the application, a particular length and geometry of the flux pipe can be designed. The effect of the aluminium shielding to prevent the flux from exiting the back of the pad and presenting a problem within a vehicle or causing heating of nearby objects, generates strong horizontal flux paths out each end of the ferrite that are not easily absorbed and this means that the orientation of this coupler on a vehicle must be

carefully considered [34]. Without improvement it is difficult to reach transmission efficiency comparable with the other topology.

In a *circular* coil the fundamental path height is proportional to one quarter of the outer diameter [40], as shown in Figure 5.2 (c). This mean that, for high distance applications, coils with larger diameters are needed. Anyway, the circular coil quality factor Q_L stays almost unchanged when the aluminum shielding is added. On the other hand, the flux pipe coil has an opposite behavior: the fundamental flux path height is approximately half the length of the pad but when the aluminum shielding is added a significant drop on the Q_L occurs. These behaviors are shown in Figure5.2 (a) and (b).

The *rectangular* coil is usually used when the misalignment tolerance has to be reduced along a specific direction. In fact, the rectangular coil has better tolerance to alignment in lateral dimension compared with the circular coil. Anyway, as shown in [35], the circular coil exhibits better coupling with more or less similar dimensions.

In 2009, the first-generation prototype of On-Line Electric Vehicle (OLEV) was tested. It used an E-shaped magnetic structure with the power rail to charge a golf cart. Then several improvements have been studied to increase the transmission efficiency. Anyway, being these coils used for dynamic wireless charging, these solutions will not in-depth studied in this thesis.

The *Double D* pad (*DD*) was introduced in [36] to combines the advantages of both the circular and flux pipe coil. The pad geometry is shown in Figure 5.2 (e). The ferrite bars act as flux pipe. The coils are magnetically in series and electrically in parallel. Thanks to the flux pipe made from the ferrite bars the pad works as single sided flux coupler. The effect is that the aluminum shielding can be placed with a little impact on the pad quality factor and flux with a path height proportional to half of the pad length. If the Double D coil geometry has good performance in terms of coupling along the z axis, its performance shows some disadvantages in the horizontal misalignment. As shown in [37], mutual inductance between primary and secondary coil has a null position under horizontal misalignment of about 34% of the primary length.

This issue is solved by *Double D Quadrature* (*DDQ*), by adding the quadrature coil as shown in Figure 5.2 (g). It is a multi-coil coupler with two coils placed on the ferrite bar with an overlap.

To reduce the copper pad, the *Bipolar pad* was introduced. It consists of two identical, partially overlapped, and mutually decoupled coils as shown in Figure 5.2(i). The magnetic field produced by a coil crosses the coil plane in one direction inside the coil and crosses the same plane in the opposite direction outside the coil. By exploiting this fact, decoupling of partially overlapping coils can be achieved The BP has high misalignment tolerance and high coefficient of coupling similar to DDQ pad. The main advantage of BP is that it requires 25% to 30% less copper as compared to DDQ pad [38].

In this thesis the circular coil is adopted for the power transmission because thanks to its simplicity, low cost and good performance, it represents the most currently used geometry for EV wireless charging applications [39].

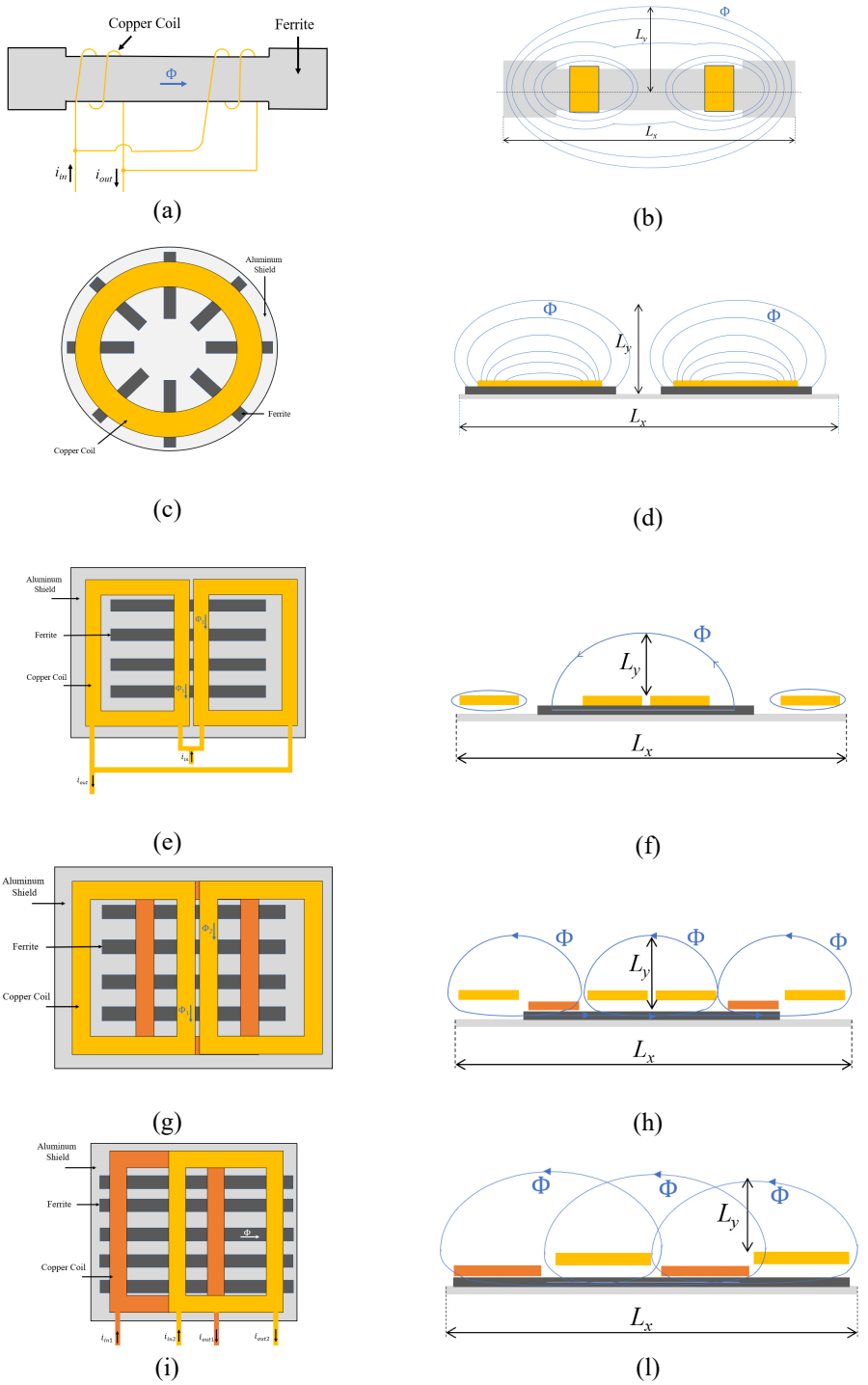

Figure 5.2: Different kind of coils.

5.2. Circular Coil Assumption

As previously explained, in this project the attention is focused on the circular coil optimization. Starting from [40-41], the effect of ferrite saturation is studied performing Finite Element Analysis (FEA) and validating the results experimentally. According to the SAE J2954 standard, the system operating frequency is fixed to f = 85 kHz. It is assumed that the geometry of the primary and secondary coil is the same. According to the space available on the vehicle, the coil dimension is limited to a maximum diameter of D_0 =50 cm. From simulations, the maximum amplitude of the sinusoidal current flowing through the coil is I_{max} = 100A. To avoid overheating due to power losses caused by skin effect and an excessively limited section, a Litz wire made up from of 2875 strand with a 38AWG diameter is selected. The coil was designed to reduce the skin effect at a frequency f=85kHz. The coil distance is fixed to d = 15 cm, while misalignment is not taken into account.

5.3 Finite Element Analysis Without Ferrite

The first step of the analysis is the design of the coil geometry without considering the effect of ferrite bars, which will be added in a following step. Using a Finite Element Modeling (FEM) software several simulations were performed by varying the number of coils turns N and the coil to coil distance d. A fixed diameter of D_0 = 40 cm was assumed. In Figure 5.3 the coil geometric parameters are shown.

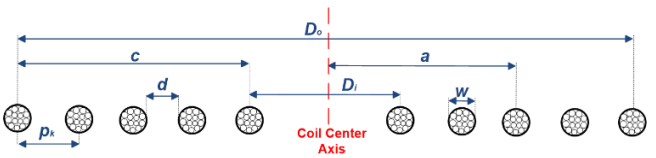

Figure 5.3: Parameters and coil geometry.

In [42], the Wheeler formula to estimate the inductance expressed in mH for a circular coil starting from the coil geometry is presented

$$L(mH) = 39.37 \cdot 10^{-3} \cdot \frac{a^2 N^2}{8a + 11c} \tag{80}$$

where c is the distance among the coil inner turn middle-point and the outer turn and is defined

$$c = \frac{D_o - D_i}{2} \tag{81}$$

while a is the distance among the coil axis and the middle of the coil winding is defined as

$$a = \frac{D_o + D_i}{4} \tag{82}$$

From (80), the coil self-inductance L decreases when increasing turn to turn distance d, while it increases when increasing the number of turns N. On the other hand, the parasitic resistance has an opposite behavior. It increases increasing of the number of turns due to dc-resistance while it increases with the decreasing of distance between turns due to the proximity effect. Concerning the inductance L, the behavior can be seen from Figure 5.4.

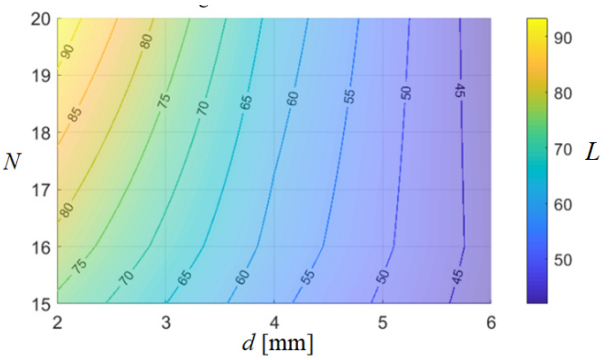

Figure 5.4: Analytical value of inductance as a function of the number of turns and distance.

To guarantee a viable compromise between inductances and parasitic resistance, a pad composed of N =15 turn spaced with d = 4 mm corresponding to an inductance of L = 58 µH was chosen.

5.4 Selection of Soft Ferrite Material

In a circular coil, ferrite plates are usually used for two main reasons:

- Creating a low reluctance flux path and improve the coupling between coils.
- Reducing the magnetic field in the surrounding environment to guarantee the safety of the people according to the International Commission on Non-Ionizing Radiation Protection (ICNIRP) directives. For this purpose, an additional aluminum plate is used to improve structural robustness and provide magnetic shielding.

There are two types of ferrites: soft and hard ferrite. Soft ferrite has low coercivity, meaning that the magnetization of the material can easily reverse direction without dissipating much energy. This property makes them suitable to be used in high frequency applications. On the other hand, hard ferrite has high coercivity and high remanence after magnetization.

This application characterized by high frequency reverse material magnetization, thus soft ferrite is used. The most common soft ferrites are composed by a combination of Manganese and Zinc (MnZn) or Nickel and Zinc (NiZn). The NiZn ferrites have a very high resistivity and are usually used for frequencies over 1 MHz. The MnZn usually work at lower frequency, in general up to 3 MHz [43].

Based on the project specifications shown in the previous section and on different manufacturer ferrites, a comparison aimed to identify the best ferrite for this application was carried out. Three different materials were compared as shown in Table 5.1.

Table 5.1: CHARACTERISTICS OF FERRITE MATERIALS

Type	μ_i	d_g [kg/m^3]	T_c [°C]	Br [mT]	Hc [A/m]	Bs [mT]	ρ [Ωm]	tan(δ)/μ_i
L8F (NiZn)	1500	5100	130	130	30	330	10^5	$60\cdot10^{-6}$ @6MHz
HS12 (MnZn)	12000	4900	130	80	6	430	0.5	$20\cdot10^{-6}$ @0.1MHz
M33 (MnZn)	2300	4700	200	55	9	390	5	$6\cdot10^{-6}$ @ 0.1MHz

The *B-H* hysteresis loop is a very useful guide for the comparison of different types of magnetic materials. One of the most important properties of ferrite when operating with AC current is the core loss. The core loss is a function of the material, core geometry, magnetic flux density B_{AC}, frequency f, and operating temperature. Thus, the choice of the magnetic material is based upon achieving the best characteristic using the standard trade-off such as cost, size, and performance.

The material L8F is NiZn, while the material HS12 and M33 are MnZn. The L8F material exhibits higher ohmic resistivity ρ but lower permeability μ_i. It can work at higher frequency compared with the other ones. Anyway, operating at f=85 kHz, the MnZn materials are more suitable for this application. The choice is therefore between HS12 and M33. The HS12 has a very high permeability but a resistivity ten times lower than M33, leading to higher eddy current losses. For this reason, the M33 material is chosen because even though it has a lower permeability, it shows higher resistivity and lower density d_g. For these reasons it is the most suitable for our purposes.

The power losses of a ferrite bar can be calculated with the following equation [44]

$$P_{core} = C_m f^{\alpha} B_{\max}^{\beta} \tag{83}$$

where C_m, α, and β are the constants which depend on the core properties. It indicates that, the bar loss for magnetic field at any point in the ferrite is directly related with the frequency of the magnetic field and the peak flux density B_{max}. The total bar loss is the volume integral of this loss in the transmitter and receiver bars, given as follows

$$P_{core}^{tot} = C_m f^{\alpha} \int_{pad} B_{\max}^{\beta} dV \tag{84}$$

Working at a fixed frequency f = 85kHz, once selected the ferrite type, the only parameter left for optimization is the flux density distribution in the bars. This means that it is possible to optimize the ferrite core losses working on the number of turns, the position and span of the coil as well as the permeability, geometry and most importantly the thickness of the core.

5.5 Positioning and Optimization of Ferrite Bars

In [40-41], the relative position between copper turns and ferrite bars that maximize the mutual inductance minimizing the leakage flux is shown. Starting from these results, a more in-depth analysis was carried out considering the ferrite nonlinear behavior when it is in saturation. Performing several FEM simulations, it was possible notice that the magnetic flux B decreases along the ends of the bars, as shown in Figure 5.5. These ferrite parts where the induction is very low are thus useless resulting in a waste of material. For this reason, the bars length was reduced letting them protrude only one centimeter with respect to the coil. An optimal length was L = 142.5 mm.

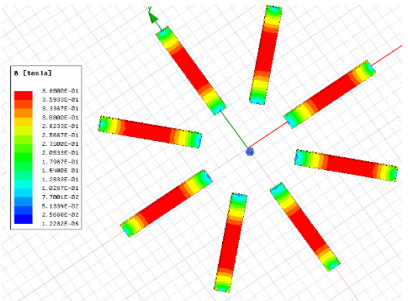

Figure 5.5: Magnetic field distribution across ferrite bars.

Once the bars length was selected, the attention was focused on the bar width and thickness. Using N=15 turns, an outer diameter of D_o=40 cm and b=8 bars with a length of L=142.5 mm an analysis on the self-inductance, the maximum magnetic flux densities and volume for different values of thickness and width was performed. In order to limit weight, size and cost of the pad, a thickness between 5 and 10 mm and a width between 25 and 40 mm was considered. The results shown in Figure 5.6 (a) show that if 25 mm width are chosen (blue trace), the bars work close to saturation independently from the thickens. A good compromise between saturation and weight is achieved using a width of 35mm and a thickness of 7.5mm. The magnetic flux density trough the bars is shown in Figure 5.6 (b).

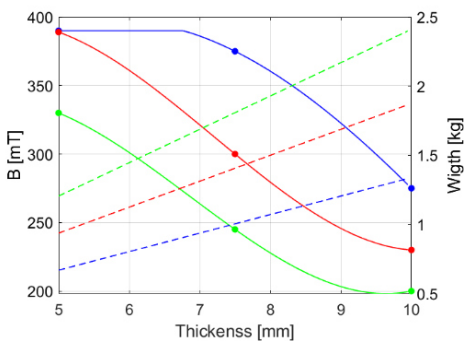

(a)

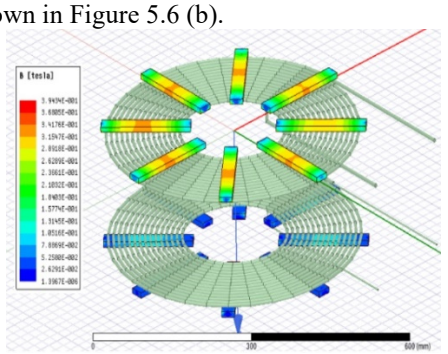

(b)

Figure 5.6. (a) Maximum Magnetic field and weight varying thickness. The blue trace is with 25mm width, the red trace is with 35mm width and the green trace is with 45mm width. (b) Flux Density with 7.5 mm thickness and 35 mm width

5.6 Aluminum Shielding

The Aluminum skin depth at a frequency f = 85kHz, resistivity ρ = $2.75 \cdot 10^{-8}\Omega$m, angular frequency $\omega = 2\pi f$ and permeability $\mu = 1.25 \cdot 10^{-6}$ H/m is

$$\delta = \sqrt{\frac{2\rho}{\omega\mu}} \tag{85}$$

The induced current density field into the aluminum plate does not vary significantly when increasing plate thickness, as long as thickness is greater than skin depth. For this reason, an aluminum plate of 1 mm thickness was used.
The system with the aluminum shielding was studied using the eddy current module in the FEA software.

The variable magnetic field induces eddy currents in the aluminum shield producing ohmic losses and reducing the mutual inductance. To avoid ferrite saturation, it has been necessary to increase ferrite bar thickness. Hence, ferrite bars with 9 mm thickness were used. In fact, coil self-inductance without aluminum plate is L_1 =91.25 μH with a mutual inductance of M=17.23μH, while the self-inductance with aluminum plate is L_1 = 84.25 μH with a mutual inductance of M = 15.10 μH.

5.6 Human Exposure to Electromagnetic Field

In this section, the electromagnetic field human exposure is analyzed to ensure the acceptable levels as specified in safety standard. There are two international groups that set standards/guidelines for Human Exposure to Electromagnetic Field (EMF): one is the International Committee on Electromagnetic Safety (ICES), and the other one is International Commission on Non-ionizing Radiation Protection (ICNIRP) [45].

As shown in Figure 3.1 for frequencies between 3 kHz and 10 MHz, the reference levels for occupational exposure to time-varying magnetic fields is 100 μT (rms), while reference level for public exposure to time-varying magnetic fields is 27 μT (rms). Since in this case, the field of interest is wireless power transfer system for electric vehicle operated for private use it is reasonable to consider it under occupational exposure regulation.

The smaller cars have a width of 150 cm. For this reason, the rms value of the magnetic field density B is evaluated in the “Point 0”, which is 75 cm far from the center of the pad, as shown in Figure 5.7 (a) and (b). The electromagnetic field exposure under the three cases of Figure 5.8 along the axis x and z is shown in Figure 5.9(a) and (b).

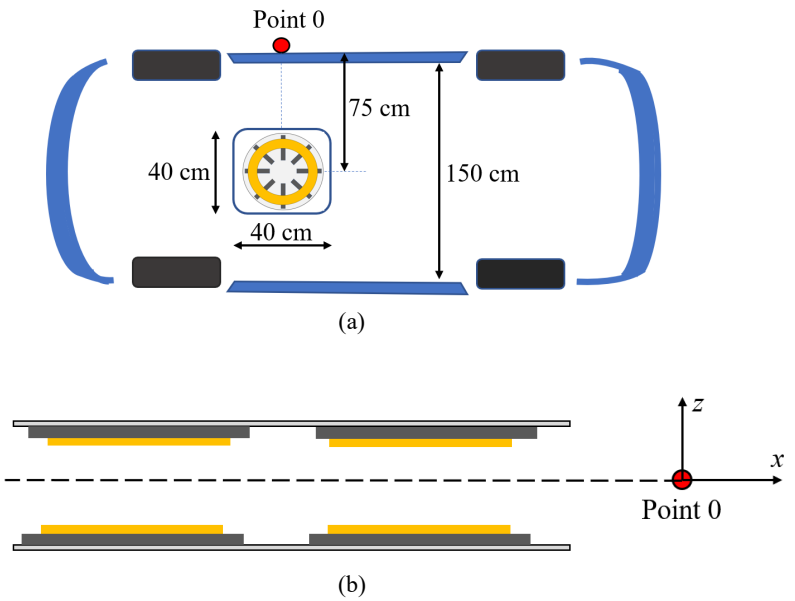

Figure 5.7: Position of the measured human exposure to magnetic flux density.

Three cases are studied: the coil without ferrite (yellow trace), the coil with ferrite bars (green trace) and the full pad made up from copper, ferrite and aluminum shielding (red trace).

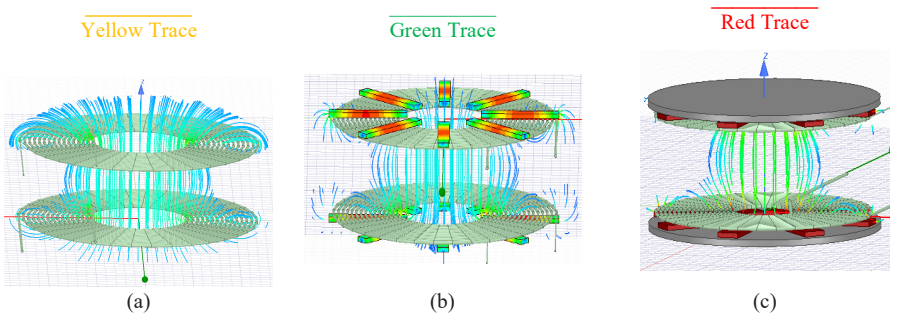

Figure 5.8: (a)Leakage magnetic flux without ferrite bars and shields. (b) Leakage flux without shield. (c) Leakage flux with aluminum shield.

As expected, the dispersed field was gradually reduced during the design steps. The yellow trace represents the pad without ferrite plates and shielding. The green trace represents the case with only ferrite plates, while the red trace represents the complete pad with ferrite and aluminum shield. The electromagnetic field exposure measured along the *x* axis is shown in Figure 5.9(a), while the exposure measured along the *z* axis is shown in Figure 5.9(b). The

EMF exposure is steadily under the occupational exposure limit only if aluminum shield is used. On the other hand, the EMF exposure is out of standard until 600 mm if the shielding is not used.

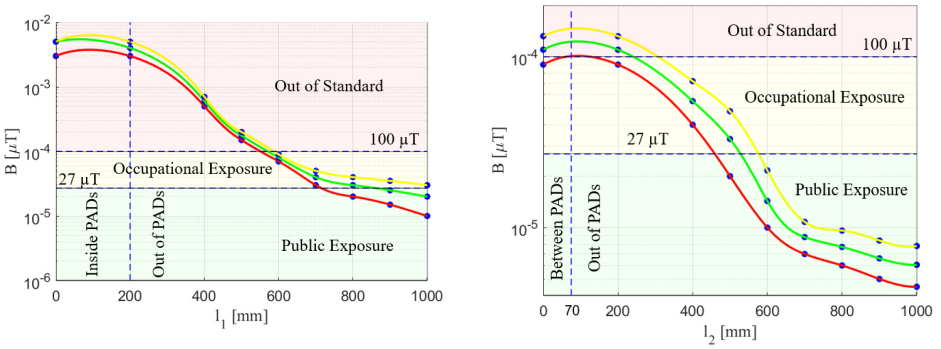

(a) (b)

Figure 5.9: Comparison between coil with aluminum shield and ferrite (red trace), coil with ferrite (green trace) and only coil (yellow trace) EMF exposure along *l1* and l_2 axis. (a) Directions of the two axes. (b) Magnetic field along l_1. (c) Magnetic field along l_2.

5.7 Power Loss Reduction

A useful tool available in Ansys Maxwell is the ohmic losses calculator. The ohmic losses can be calculated as

$$P_{ohmic} = \frac{1}{2\sigma}\iiint_V \mathrm{Re}\left(\vec{J}\cdot\vec{J}\right)dV \tag{86}$$

The ohmic losses have three main contributions. Losses in the copper coil due to skin and proximity effect, losses in the ferrite bars due to the limited resistivity and the aluminum losses caused by Foucault currents created from the alternate magnetic field. From the simulation results shown in Figure 5.10 (a) it is clear that the major ohmic losses are related to the copper coils and in the aluminum shield.

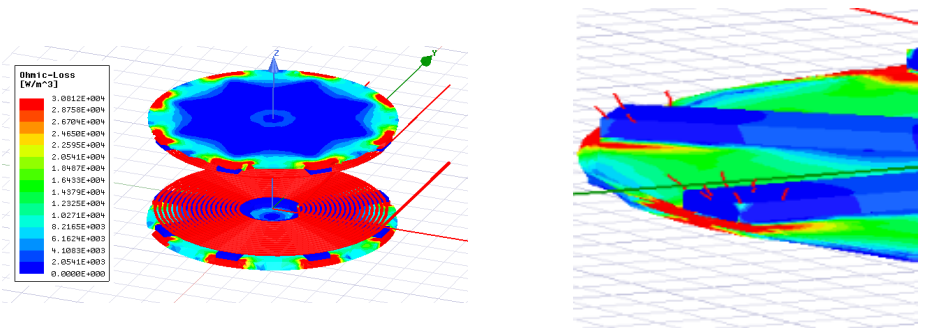

(a) (b)

Figure 5.10. Ohmic losses analysis (a)Ohmic Losses in the coil. (b) Aluminum ohmic losses at the ferrite bar termination caused from Foucault current

The copper coil losses cannot be further reduced because the AWG strand, diameter and coil geometry were already optimized. By analyzing in detail the FEM results, a critical issue concerns the ferrite termination was highlighted. In Figure 5.10, the magnetic field lines from the aluminum shield at the edge of the ferrite bars produce important ohmic losses which cause heating of the shield. The addiction of the steps (Figure 5.11) has improved the system efficiency reducing the losses due to the shield. The self-inductance with step is L = 88.64 µH with a mutual inductance of M =16.44 µH, while without step the self. Inductance is L = 84.25 µH with a mutual inductance of M =15.10 µH.

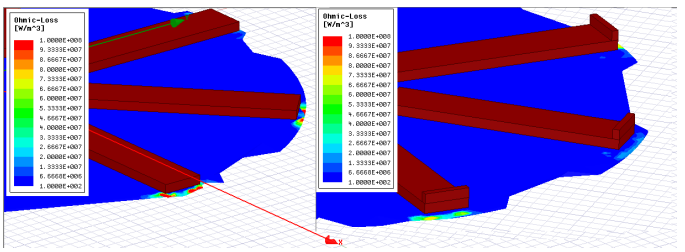

Figure 5.11: Ferrite Step insertion at the end of the bars.

5.7 Experimental Results

The mutual inductance between two planar circular coils is presented in [46]. In this paper the tracks of the planar inductors are modeled as constant current carrying filaments, as shown in Figure 5.12, and the mutual inductance between individual filaments is determined by Neumann's integral. The proposed model is derived by solving Neumann's integral using a series expansion technique. This model can predict the mutual inductance at various axial and lateral displacements. The mutual inductance M_{ij} between two single spiral coils can be calculated as

$$M_{ij} = \frac{\pi\mu_0 a_i^2 b_j^2}{2\left(a_i^2 + b_j^2 + z^2\right)^{3/2}} \tag{87}$$

To calculate the mutual inductance M between two multi-turns single layer spiral coil it is necessary calculate the coupling between each single turn

$$M = \rho \sum_{i=1}^{n_p} \sum_{j=1}^{n_s} M_{ij} \tag{88}$$

With

$$M_{ij} = \frac{\pi\mu_0 a_i^2 b_i^2}{2\left(a_i^2 + b_i^2 + z^2\right)^{3/2}} \left(1 + \frac{15}{32}\gamma_{ij}^2 + \frac{315}{1024}\gamma_{ij}^4\right) \tag{89}$$

$$\gamma_{ij} = \frac{2a_i b_j}{a_i^2 + b_i^2 + z^2} \tag{90}$$

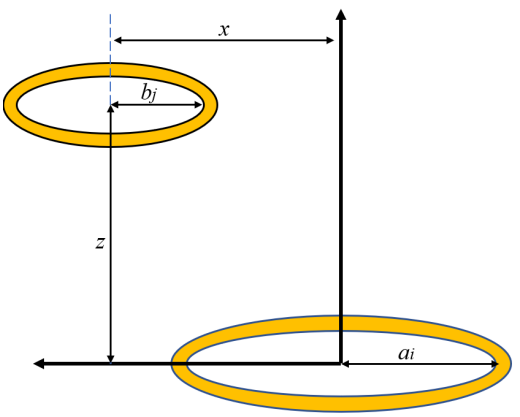

Figure 5.12: Mutual Inductance between two coil loops.

To validate the FEA results, the system was reproduced in laboratory. The experimental setup is shown in Figure 5.13(a) and (b).

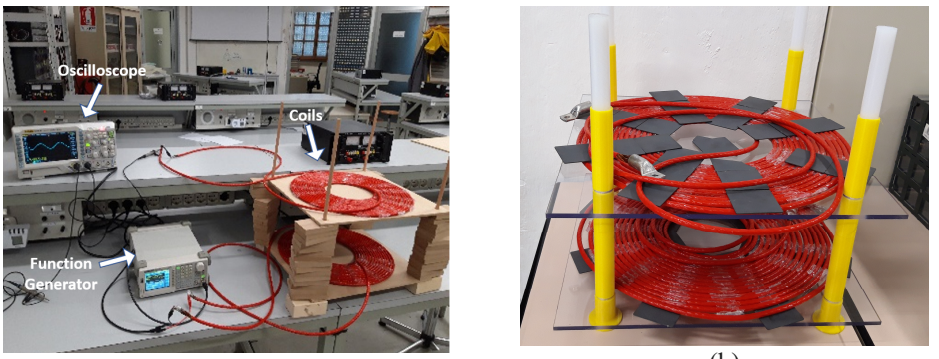

(a) (b)

Figure 5.13:Experimental setup. (a) Coils and Instrumentation. (b) Coils with ferrite bars.

Figure 5.14 (a) represents the electric circuit used to measure the mutual inductance.

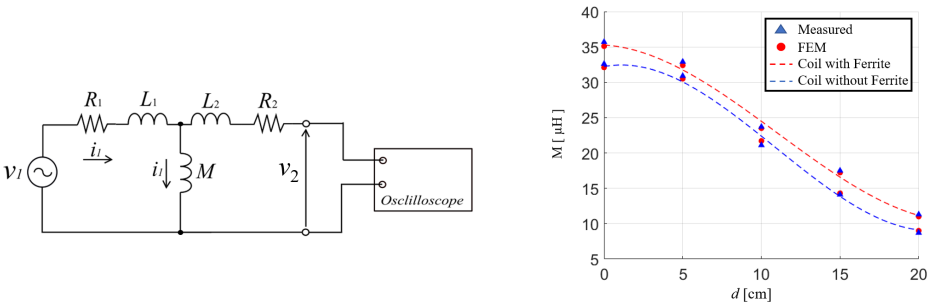

(a) (b)

Figure 5.14. (a) Equivalent measurement circuit. (b) Comparison between FEM simulations and Experimental results.

To measure the mutual inductance, the primary coil was supplied by a sinusoidal voltage and the induced voltage on the secondary side was measured with an oscilloscope. The value of the mutual inductance is

$$M = \frac{L_1 V_2}{V_1 - R_1 I_1} \tag{91}$$

The results are shown in Figure 5.14 (b).

At f=85kHz, the measured primary inductance is L_1=82.43μH with a parasitic resistance R_1=0.055 Ω, and a secondary inductance L_2=89.22 μH with a parasitic resistance R_2=0.061Ω. The obtained results are shown and compared to the simulations in Figure 5.14(b).

6. Control Strategies

6.1. System Architecture

The circuit topology of the proposed wireless charging system is shown in Figure 6.1.

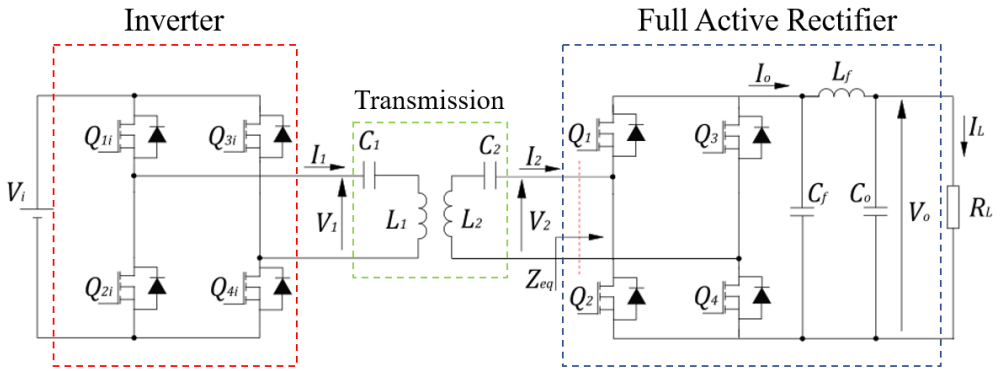

Figure 6.1: Simplified circuit topology.

The system is supplied from a DC voltage V_i which can be obtained rectifying the single-phase or three-phase power grid voltage. Then, an high frequency square wave with amplitude $\pm V_i$ is forced to the resonant tank through the full bridge inverter. Using the First Harmonic Analysis (FHA), only the first harmonic of the square voltage V_1 is considered, neglecting the higher order harmonics. The sinusoidal voltage V_1 supply the resonant tank and a sinusoidal secondary current I_2 is generated on the secondary side. This current is regulated from the full-active rectifier (FAR) in order to charge the vehicle battery, which is approximated with a load resistance R_L. In the next sections, two different control strategies will be presented, highlighting the advantages and limitations.

6.2 Control Strategy I: Variable Duty Cycle

In this control strategy, only one variable is used to regulate the output current. The modes of operation used to regulate the output current I_o are shown in Figure 6.2:

1. State I ($0 < t < t_0$): Both the MOSFETs Q_2 and Q_4 are turned ON. Current is not transferred to the load resistance during this state. The impedance seen from the secondary tank is the sum of the conduction resistance of the MOSFETs.
2. State II ($t_0 < t < t_1$): The MOSFET Q_2 is turned OFF and, therefore the current flows through Q_1 which is turned ON. The secondary current is transferred to the load.
3. State III ($t_1 < t < t_2$): The MOSFET Q_2 is turned ON. During this period the current is not transferred to the load.
4. State IV III ($t_2 < t < t_3$): The MOSFET Q_4 is turned OFF. The current flows through Q_2 and Q_3 which is turned ON. The secondary current is transferred to the load.

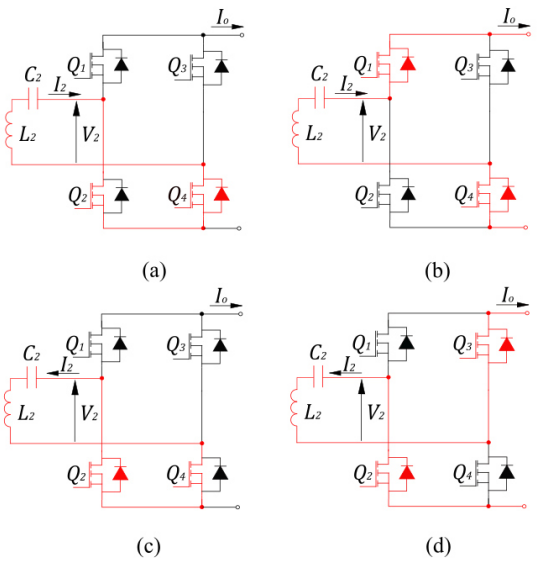

Figure 6.2: FAR Modes of operation.

The currents and voltages waveforms are shown in Figure 6.3. The FAR input current is i_2, while the output current which will be filtered to charge the batteries is i_0. The gate-to-source voltage MOSFETs are v_{GS2} and v_{GS4}. The voltage v_{GS1} is obtained inverting v_{GS2}, while the voltage v_{GS3} inverting v_{GS4}. In order to avoid cross conduction between MOSFETs of the same leg, a deadtime is used. The circuit used to perform the deadtime will be explained subsequently. The FAR input voltage is v_2, while with v_2^1 is named its first harmonic. The phase shift between the FAR input current i_2 and input voltage v_2 is named φ.

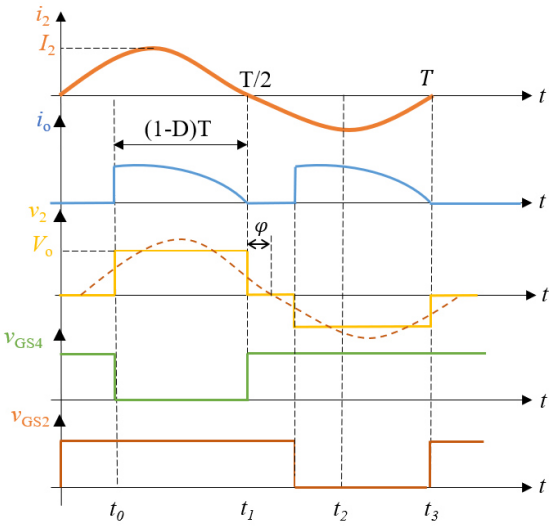

Figure 6.3: voltage and currents waveforms.

The assumptions under which the impedance matching is studied are:

- The position and the distance between the car and the charging station are fixed. This is compatible with a static wireless charging. Thus, the mutual inductance between the coils M is considered to be constant.
- The system is secondary side controlled. Thus, the transmission frequency f and the rms value of the input voltage V_i^{rms} are assumed fixed, being these values defined from the primary side.
- The vehicle battery is initially approximated as resistive load. The value of resistance depends on the state of charge.
- The primary and secondary capacitances C_1 and C_2 are calibrated on the optimal value shown in section 4.2.4.

If the semi-bridgeless active rectifier is in stable state, the average output current can be calculated from Figure 6.4 as

$$I_o^{avg} = \frac{1}{2\pi}\int_0^{2\pi} i_o(\omega t)\,d\omega t = \frac{1}{\pi}\int_0^{\pi} I_2 \sin(\omega t)\,d\omega t = \frac{I_2}{\pi}\left[-\cos(\pi)+\cos(2D\pi-\pi)\right]$$
$$= \frac{I_2}{\pi}\left[-\cos(\pi)+\cos(2D\pi)\cos(\pi)+\sin(2D\pi)\sin(\pi)\right] = \frac{I_2}{\pi}\left[1-\cos(2D\pi)\right] \quad (92)$$

The secondary current of the SS compensation is approximately independent from load variation R_L. Thus, it is possible to adjust the output current I_o^{avg} regulating the duty cycle D in the interval $D \in [0.5, 1]$. If D=0.5, the maximum current is delivered to the load

$$I_o^{avg}\Big|_{D=0.5} = \frac{2I_2}{\pi} \tag{93}$$

On the other hand, if D=1 the load is completely disconnected from the wireless system and no power is delivered, i.e.,

$$I_o^{avg}\Big|_{D=1} = 0 \tag{94}$$

Neglecting the parasitic resistances R_1 and R_2, the secondary current can be approximated as

$$I_2 \cong \frac{V_1}{\omega M} \tag{95}$$

Thus, a simple control strategy can be implemented: if an output current I_o^{avg} is needed to charge the battery the duty cycle has to be

$$D = \frac{1}{2\pi}\arccos\left(1 - \pi\frac{I_o^{avg}}{I_2^{avg}}\right) \tag{96}$$

An important task of the system is the achievement of high transmission efficiency. To reach this condition, attention has to be placed on the impedance matching between resonant tank and rectifier. To perform impedance matching, an analytical expression of the active rectifier equivalent impedance has to be found. As shown in Figure 6.3, the first harmonic of the voltage v_2 is behind the current i_2, with a phase shift between them of

$$\varphi = \left(\frac{1}{2} - D\right)\pi \tag{97}$$

The amplitude of the first harmonic voltage v_2 can be easily calculated using the Fourier series, shifting the voltage of φ in order to make it odd. Thus, the Fourier coefficient of the voltage can be written as

$$v_s^{'}(\omega t) = \frac{a_0}{2} + \sum_{n=1}^{N}\left[a_n\cos(n\omega t) + b_n\sin(n\omega t)\right] \tag{98}$$

With

$$a_0^{'} = \frac{2}{T}\int_0^{2\pi} v_s^{'}(\omega t)dt = 0 \tag{99}$$

$$a_n^{'} = \frac{2}{T}\int_0^{2\pi} v_s^{'}(\omega t)\cos\left(\frac{2\pi n\omega t}{T}\right)d\omega t = 0 \tag{100}$$

$$b_n^{'} = \frac{2}{T}\int_0^{2\pi} v_s^{'}(\omega t)\sin\left(\frac{2\pi n\omega t}{T}\right)d\omega t = \frac{4V_S^{\max}}{2\pi n}\left[\cos\left(\frac{n\pi}{4}\right) - \cos\left(\frac{3n\pi}{4}\right)\right]\sin(\pi D) \tag{101}$$

Taking into account the phase shift respect to the current i_2, it can be expressed as phasor

$$V_s^1 = \frac{2\sqrt{2}}{\pi} V_o \sin(\pi D) e^{j\left(\frac{1}{2}-D\right)\pi} \tag{102}$$

Thus, using the First Harmonic Analysis (FHA), the equivalent impedance of the active rectifier can be expressed as

$$Z_{eq} = \frac{V_s^1}{I_2} = \frac{2\sqrt{2}}{\pi} \frac{V_o}{I_2^{rms}} \sin(\pi D) e^{j\pi\left(\frac{1}{2}-D\right)} \tag{103}$$

That expressed in real and imaginary part is

$$Z_{eq} = R_{eq} + jX_{eq} = \frac{2\sqrt{2}}{\pi} \frac{V_o}{I_2^{rms}} \sin(\pi D) \left[\cos(\frac{1}{2} - D) + j \sin(\frac{1}{2} - D) \right] \tag{104}$$

6.2.1 Impedance Matching

The aim of the FAR is to give to the battery the desired current and voltage charging profile trying to simultaneously work at high transmission efficiency. From the previous analysis it exists an optimal value of load resistance that maximize the efficiency, which under the previous hypothesis can be assumed fixed to

$$R_L^{\eta_{\max}} = \sqrt{\frac{\omega^4 C_2^2 \left[M^2 R_2 + L_2^2 R_1 \right] + \omega^2 C_2 R_1 \left[C_2 R_2^2 - 2L_2 \right] + R_1}{\omega^2 C_2^2 R_1}} \tag{105}$$

The system working in resonance, therefore the previous expression can be simplifying as

$$R_L^{\eta} = R_2 \sqrt{1 + \frac{\omega^2 M^2}{R_1 R_2}} \tag{106}$$

The current at the input of the rectifier is

$$I_2 = \frac{-j\omega M}{\left[R_1 + j\left(\omega L_1 - \frac{1}{\omega C_1} \right) \right] \left[R_2 + R_L + j\left(\omega L_2 - \frac{1}{\omega C_2} \right) \right] + \omega^2 M^2} V_1 \tag{107}$$

Neglecting the parasitic resistance R_1 and R_2 and working in resonance, the equation can be simplified as following

$$I_2 \cong \frac{V_1}{\omega M} \tag{108}$$

If a current I_0 has to be supplied to the battery, the rectifier has to operate with a duty cycle

$$D = \frac{1}{2\pi}\arccos\left(1 - \frac{\pi I_{BATT}}{\sqrt{2} I_2^{RMS}}\right) \tag{109}$$

Thus, its equivalent impedance is $Z_{eq}=R_{eq}+jZ_{eq}$

$$\mathrm{R}_{eq} = \frac{2\sqrt{2}}{\pi}\frac{U_L}{I_2^{rms}}\sin(\pi D)\cos(\frac{1}{2} - D) \tag{110}$$

$$X_{eq} = \frac{2\sqrt{2}}{\pi}\frac{U_L}{I_2^{rms}}\sin(\pi D)\sin(\frac{1}{2} - D) \tag{111}$$

Thus, using this control strategy, the equivalent impedance of the rectifier has resistive and a reactive component. However, the transmission efficiency is maximized if the equivalent impedance of the FAR is equal to (106). The reactive part X_{eq} variable with the duty cycle, therefore it is difficult to be compensated. In addition, during the charging process, the resistive part R_{eq} can be different from the optimal one R_L^{max}. This means that, using only the duty cycle as control degree of freedom, the optimal charging cannot be achieved. This limitation can be overcome introducing an additional control degree of freedom as shown in the following section.

6.2.2 Conduction Losses Analysis

To estimate the conduction losses on the MOSFETs, the rms value of the current passing through them is calculated. The current flowing through the Q_1 and Q_2 is shown in Figure 6.4.

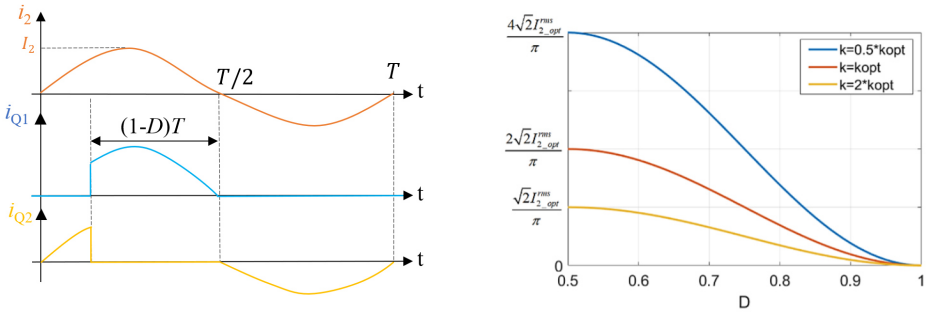

(a) (b)

Figure 6.4. (a) Current flowing through the MOSFETs. (b) Output Current for different coupling coefficient and duty cycle.

The rms value of the current flowing through Q_1 can be calculated as

$$I_{Q1}^{rms}=\sqrt{\frac{1}{T}\int_0^T i_{Q1}^2(t)dt}=\sqrt{\frac{1}{T}\int_{\frac{T}{2}-(1-D)T}^{\frac{T}{2}} I_2^2\sin^2(\omega t)dt}=\sqrt{\frac{I_2^2}{T}\left[\frac{t}{2}-\frac{\sin(2\omega t)}{4\omega}\right]_{\frac{T}{2}-(1-D)T}^{\frac{T}{2}}}=I_2\sqrt{\frac{(1-D)}{2}+\frac{1}{8\pi}\sin\left[2\pi(2D-1)\right]} \tag{112}$$

While the average current is

$$I_{Q1}^{avg}=\frac{1}{T}\int_0^T i_{Q1}(t)dt=\frac{1}{T}\int_{\frac{T}{2}-(1-D)T}^{\frac{T}{2}} i_2(t)dt=\frac{1}{T}\int_{\frac{T}{2}-(1-D)T}^{\frac{T}{2}} I_2\sin(\omega t)dt=\frac{I_2}{2\pi}\left[1+\cos(2\pi D)\right] \tag{113}$$

The rms value of the current flowing through Q_2 can be calculated as

$$I_{Q2}^{rms}=\sqrt{\frac{1}{T}\int_0^T i_{Q2}^2(t)dt}==\sqrt{\frac{I_2^2}{T}\left\{\left[\frac{t}{2}-\frac{\sin(2\omega t)}{4\omega}\right]_0^{\frac{T}{2}-(1-D)T}+\left[\frac{t}{2}-\frac{\sin(2\omega t)}{4\omega}\right]_{\frac{T}{2}}^{T}\right\}}==I_2\sqrt{\frac{D}{2}-\frac{1}{8\pi}\sin(2\pi(2D-1))} \tag{114}$$

While the average current is

$$I_{Q2}^{avg}=\frac{1}{T}\int_0^T i_{Q2}(t)dt=\frac{1}{T}\left\{\int_0^{\frac{T}{2}-(1-D)T} I_2\sin(\omega t)dt+\int_{\frac{T}{2}}^{T} I_2\sin(\omega t)dt\right\}=-\frac{I_2}{2\pi}\left[1+\cos(\pi(2D-1))\right] \tag{115}$$

These equations will be subsequently used for the thermal sizing of the switching MOSFETs.

6.3 Control Strategy II: Variable Duty Cycle and Phase Shifting

In this section a different control strategy based on duty cycle and phase shift variation is proposed. The aim of this section is to investigate the possibility of improving the system performance by increasing the variables available for the control strategy. The circuit topology is the same shown in the previous section. The modes of operation of the new control strategy are shown in Figure 6.5.

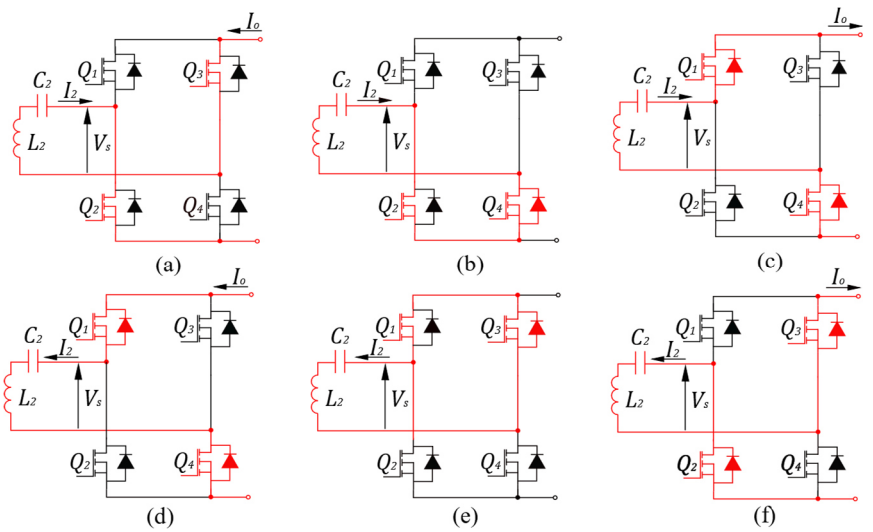

Figure 6.5: Modes of operations.

If the voltage v_s lags behind the current i_2 as shown in Figure 6.5 (a), the states of operation are:

1. State I ($0 < t < t_0$): During this interval both the MOSFETs Q_2 and Q_3 are turned ON. In this state the power is delivered from the capacitance load to the circuit. By hard switching Q_3 and soft switching Q_4 the next mode comes.
2. State II ($t_0 < t < t_1$): The voltage vs is short circuited by Q_2 and Q_4. No power is transferred to the load. By turning off (hard switching) Q_2 and turning on Q_1, the next mode comes.
3. State III ($t_1 < t < t_2$): The current flows through the load and power is transferred. No action is taken.
4. State IV ($t_2 < t < t_3$): The current changes the polarity. As in the State I, the power is extracted from the load to the circuit. By turning off Q_4 and turning on Q_3 the next modes comes.
5. State V ($t_3 < t < t_4$): the resonant tank is short circuited, and no power is delivered to the load. By turning on Q_2 (soft switching) and turning off Q_1 the next mode comes.
6. State VI ($t_4 < t < t_5$): The current flows to the load until it changes the polarity and mode I occurs again.

Defining β the duration of the pulse of the input rectifier and φ the angle between the first harmonic of the voltage v_s and the current i_2, three different modes of operation can be identified. If the shift angle $\varphi<0$, the equivalent impedance of the FAR is capacitive-resistive. If $\varphi=0$ the impedance Z_{eq} is purely resistive, while if $\varphi>0$ the impedance Z_{eq} is inductive-resistive. This behavior is shown in Figure 6.6.

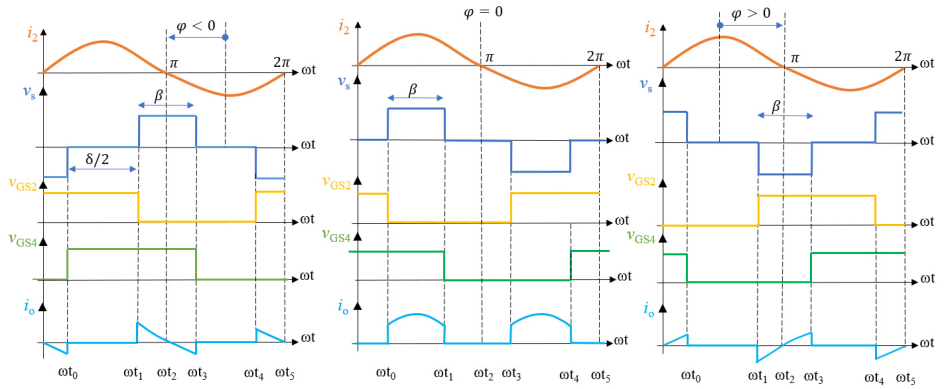

Figure 6.6: Modes of Operation. (a) Case with phase shift angle φ<0. (b) Case with phase shift angle φ=0. (c) Case with phase shift angle φ>0.

As in the previous section, the voltage v_2 at the input of the rectifier can be written as a phasor

$$V_s = \frac{2\sqrt{2}}{\pi} V_o \sin\left(\frac{\beta}{2}\right) e^{j\varphi} \tag{116}$$

According to the waveforms in Figure 6.6(a), the average of the output current i_o is

$$I_o = \frac{1}{\pi}\int_{\frac{\pi}{2}-\frac{\beta}{2}-\varphi}^{\frac{\pi}{2}+\frac{\beta}{2}-\varphi} i_2(\omega t)\,d\omega t = \frac{1}{\pi}\int_{\frac{\pi}{2}-\frac{\beta}{2}-\varphi}^{\frac{\pi}{2}+\frac{\beta}{2}-\varphi} I_2^{\max}\sin(\omega t)\,d\omega t = \frac{2\sqrt{2}}{\pi} I_2^{rms}\sin\left(\frac{\beta}{2}\right)\cos\varphi \tag{117}$$

Thus, the equivalent impedance of the rectifier can be written as

$$Z_{eq} = \frac{V_s}{I_2^{rms}} = \frac{8}{\pi^2} R_L \sin\left(\frac{\beta}{2}\right)\cos(\varphi) e^{j\varphi} = \frac{4}{\pi^2} R_L \left(1-\cos\beta\right)\cos(\varphi) e^{j\varphi} \tag{118}$$

The real and imaginary part of the impedance are

$$R_{eq} = \frac{4}{\pi^2} R_L \left(1-\cos\beta\right)\cos^2(\varphi) \tag{119}$$

$$X_{eq} = \frac{4}{\pi^2} R_L \sin(\varphi)\cos(\varphi)\left(1-\cos\beta\right) \tag{120}$$

The maximum transmission efficiency is reached when $R_{eq}= R_L{}^{\eta}$, therefore solving the system equations one obtains the conditions

$$\varphi = arctg\left(\frac{X_{eq}}{R_L^{\eta}}\right) \tag{121}$$

$$\beta = \arccos\left(1-\frac{\pi^2 R_L^{\eta}}{4R_L\cos^2(\varphi)}\right) \tag{122}$$

Studying the functions domain, the conditions needed to solve (121) and (122) is

$$\cos^2(\varphi) > \frac{\pi^2 R_L^{\eta}}{8R_L} \tag{123}$$

The possible solutions (φ, β) which satisfy the condition $R_{eq}=R_L{}^{\eta}$ for different value of load resistance R_L are shown in Figure 6.7.

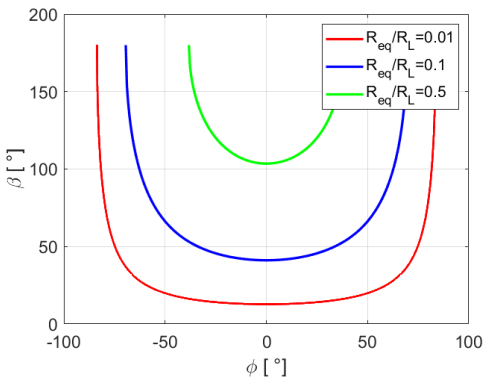

Figure 6.7: Solution (φ, β) that ensure the desired output current.

Thus, working with a shifting angle φ^*, it is possible to reproduce the optimum resistance $R_L{}^{\eta}$ only if the following condition is verified

$$\frac{R_L^{\eta}}{R_L} < \frac{8}{\pi^2}\cos^2(\varphi^*) \tag{124}$$

This is confirmed by Figure 6.7, where increasing the ratio $R_L{}^{\eta}/R_L$, a decrease in the possible angle φ occurs. If $\varphi = 0$, it is possible to operate at optimum condition only if the ratio between the load resistance R_L and the resistance that maximize the transmission efficiency R_{eq} is

$$\frac{R_{eq}}{R_L} < \frac{\pi^2}{8} \tag{125}$$

In case of cos φ <1, the system can operate under optimal condition only if

$$-\arccos\left(\sqrt{\frac{\pi^2 R_{eq}}{8R_L}}\right) < \varphi < \arccos\left(\sqrt{\frac{\pi^2 R_{eq}}{8R_L}}\right) \tag{126}$$

Thus, several solutions (φ, β) make possible to operate at $R_{eq}= R_L{}^{\eta}$. The reactive part of FAR X_{eq} is equals to zero when φ=0. The efficiency is maximized when the resonant tank is closed to a purely resistive load $R_L{}^{\eta}$, thus a phase shift angle φ=0 is chosen.

6.3.1 Impedance Matching

The aim of the control is to deliver the desired output current I_o^{ref} to the load and simultaneously ensure the maximum transmission efficiency, formulated by considering the following equations

$$\begin{cases} I_o = I_o^{ref} = \dfrac{2\sqrt{2}}{\pi} I_2 \sin\left(\dfrac{\beta}{2}\right)\cos\varphi \\ R_{Leq} = R_L^{\eta} = \dfrac{4}{\pi^2} R_L \cos^2(\varphi)\left[1-\cos(\beta)\right] \end{cases} \tag{127}$$

Solving this system of equations, one obtains

$$\cos\varphi = \frac{\pi I_o^{ref}}{2\sqrt{2} I_2 \sin\left(\dfrac{\beta}{2}\right)} \Rightarrow R_L^{\eta} = \frac{4R_L}{\pi^2}\left[\frac{\pi I_o^{ref}}{2\sqrt{2} I_2 \sin\left(\dfrac{\beta}{2}\right)}\right]^2 \left[1-\cos\beta\right] \tag{128}$$

Thus

$$\frac{1-\cos\beta}{\sin^2\left(\dfrac{\beta}{2}\right)} = 2\frac{R_L^{\eta}}{R_L}\left(\frac{I_2}{I_o}\right)^2 \tag{129}$$

with $\sin\left(\frac{\beta}{2}\right) = \pm\sqrt{\frac{1-cos\beta}{2}}$ it can be written in the form

$$1 = \frac{R_L^{\eta}}{R_L}\left(\frac{I_2}{I_o^{ref}}\right)^2 \tag{130}$$

That can be rewritten in the following form

$$\frac{R_L^{\eta}}{R_L} = \left(\frac{I_o^{ref}}{I_2}\right)^2 \Rightarrow \frac{R_L^{\eta}}{V_o I_o^{ref}} = \frac{1}{I_2^2} \tag{131}$$

The condition needed to operate at the highest transmission efficiency and to deliver the desired output current I_o^{ref} is

$$V_o I_o^{ref} = R_L^{\eta} I_2^2 \tag{132}$$

Using the SS compensation, from (105), the resistance that maximizes the transmission efficiency R_L^{η} can be assumed to be fixed. In fact, it depends on the mutual inductance M, the parasitic resistance of the coils R_1 and R_2 and the operating frequency ω. As explained before, in this project these parameters can be assumed to be constant. If the operating frequency ω and the primary voltage V_1 are constant, also the secondary current I_2 are assumed constant. Under this condition, the optimum wireless charging can be reached only by delivering to the load a constant power $P_o = V_o I_o^{ref} = R_L^{\eta} I_2^2$.

The consequences of this condition are:

- The battery must be charged with constant power charging profile. This means that while the voltage increases during the charging, the current given to the battery has to decrease to maintain the power constant.
- During the system design step, attention has to be paid to the optimum resistance $R_L{}^{\eta}$. The coils with their parasitic resistance and their mutual inductance M must be chosen to reach a desired output power P_o when a secondary current I_2 is received on the secondary side.

6.3.2 Conduction Losses

To estimate the conduction losses on the MOSFETs, the rms value of the current passing through them is calculated. The current flowing through the Q_1 and Q_2 is shown in Figure 6.8.

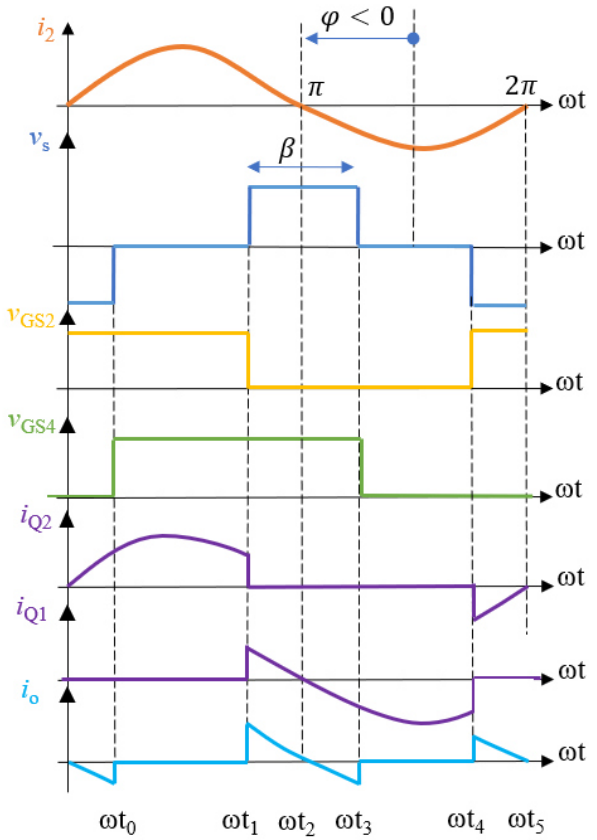

Figure 6.8: Voltage and current waveforms through the MOSFET.

The rms value of the current flowing through Q_2 can be calculated as

$$I_{Q2}^{rms} = \sqrt{\frac{1}{2\pi}\int_0^{2\pi} i_{Q2}^2(\omega t)d\omega t} = \sqrt{\frac{1}{2\pi}\int_{\frac{\pi}{2}-\varphi-\frac{\beta}{2}}^{\frac{3\pi}{2}-\varphi-\frac{\beta}{2}} I_2^2 \sin^2(\omega t)d\omega t} = \sqrt{\frac{I_2^2}{2\pi}\left[\frac{\omega t}{2} - \frac{\sin(2\omega t)}{4\omega}\right]_{\frac{\pi}{2}-\varphi-\frac{\beta}{2}}^{\frac{3\pi}{2}-\varphi-\frac{\beta}{2}}} = \frac{I_2}{\sqrt{4}} \tag{133}$$

While the rms value of the current flowing through Q_1 can be calculated as

$$I_{Q1}^{rms} = \sqrt{\frac{1}{2\pi}\int_0^{2\pi} i_{Q1}^2(\omega t)d\omega t} = \sqrt{\frac{1}{2\pi}\int_{\frac{\pi}{2}-\varphi-\frac{\beta}{2}}^{\frac{3\pi}{2}-\varphi-\frac{\beta}{2}} I_2^2 \sin^2(\omega t)d\omega t} = \sqrt{\frac{I_2^2}{2\pi}\left[\frac{\omega t}{2} - \frac{\sin(2\omega t)}{4\omega}\right]_{\frac{\pi}{2}-\varphi-\frac{\beta}{2}}^{\frac{3\pi}{2}-\varphi-\frac{\beta}{2}}} = \frac{I_2}{\sqrt{4}} \tag{134}$$

6.2 Simulation Results

The two control strategies were simulated on Plexim. In Figure 6.9 the whole schematic is shown.

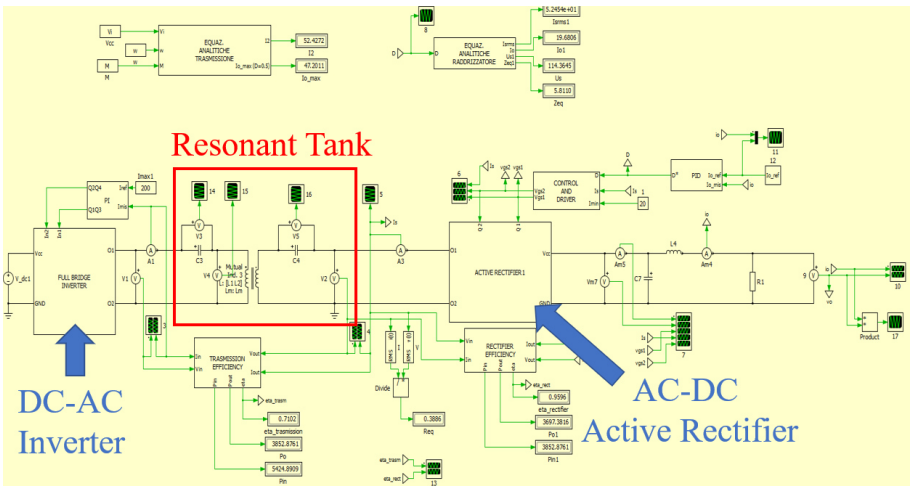

Figure 6.9: Schemathic of the control using Plexim.

In Figure 6.10 some results using the control strategy I are shown.

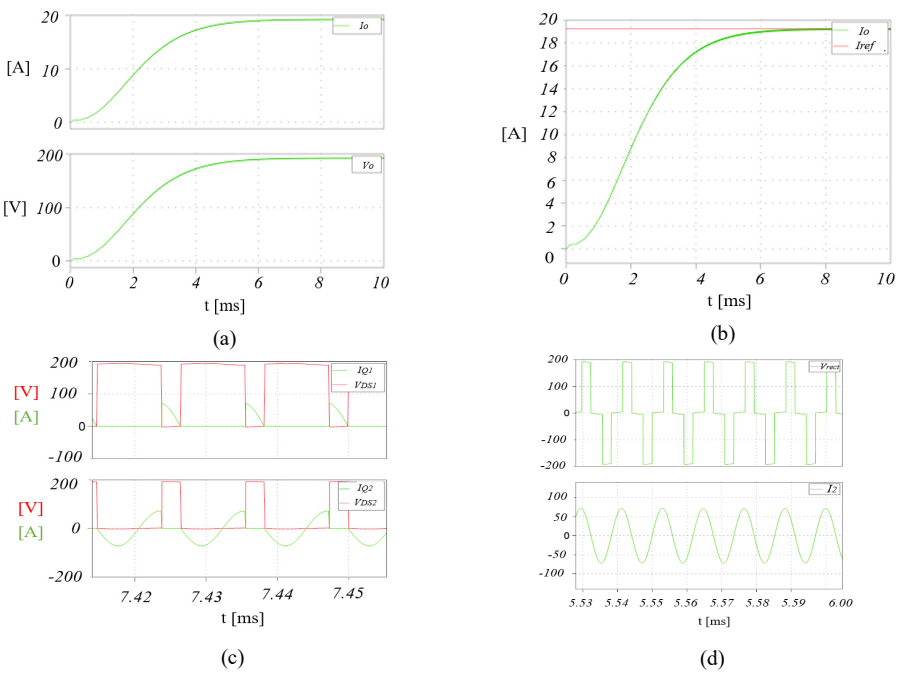

Figure 6. 10. FAR Measurement. (a) Output current and Output voltage. (b)Output current and reference current. (c) Current and Voltage across high side and low side MOSFET. (d) FAR Input voltage and input current

In Figure 6.10(a) the voltage and current through the load resistance R_L=10Ω are shown. As expected, the power is P_o=3.7kW. In Figure 6.10(b) it is shown how the output current goes to the reference. In Figure 6.10(c) the current and voltage through the MOSFET, while in Figure 6.10(d) the FAR input current and voltage are shown. The efficiency is estimated for both transmission and rectifications. From the simulation a transmission efficiency η_{tran}=0.97 and a rectification efficiency η_{FAR}=0.95 are achieved. The expected system efficiency is lower because the switching losses are not taken into account during this simulation.

7. Design and Development of Charging System Prototype

7.1. Inverter and Full Active Rectifier

As shown in Figure 6.1, the WPT system is made up from a primary inverter and a secondary rectifier. The topologies of these two converters are very similar. In order to reduce the cost and the complexity of the system, a power board able to work both as inverter and rectifier, depending on jumpers connection, was designed. The designed PCB board is shown in Figure 7.1.

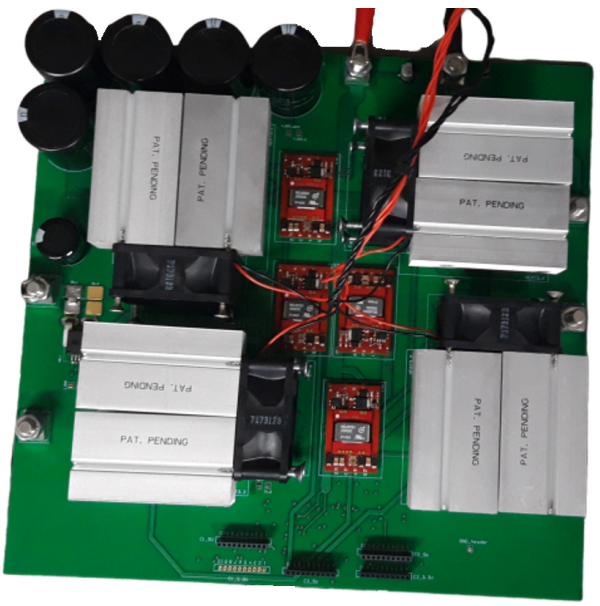

Figure 7.1: PCB power Board

The operating scheme is shown in Figure 7.2. The power board is supplied from an external +24V DC bus. Then, the voltage levels is changed by DC-DC converters. The isolated transformer MGJ6D242005DC by Murata is used to convert the +24 to +20V used to supply

the SiC MOSFET driver. All the components such as MOSFETs driver and current sensor are supplied by a voltage +5V created by a Traco Power TDN-3-2411N.

In order to perform the control strategy, the current flowing in the secondary coil has to be measured. When the circuit is working at the maximum power, the secondary sinusoidal current has a frequency of 85kHz and a maximum amplitude of 100A. These characteristics make the measurement challenging. As shown in Figure 7.2, the adopted implementation solution for components consists on two shunt resistor R_{shunt} placed between the source of the MOSFETs and the ground. Being on side of the shunt resistor referred to ground, this greatly simplifies the measurements reducing the voltage common mode requirements of the ICs.

The current delivered to the battery is measured by Hall sensor. These sensors are able to measure high current value but are usually characterized by a limited band. For this reason, a Hall sensor is used to measure the changing current which is characterized by a low dynamic. The red lines in the schematic represents the output signals of the board. They are the currents measurement which are processed by the STM32 control board to control the system.

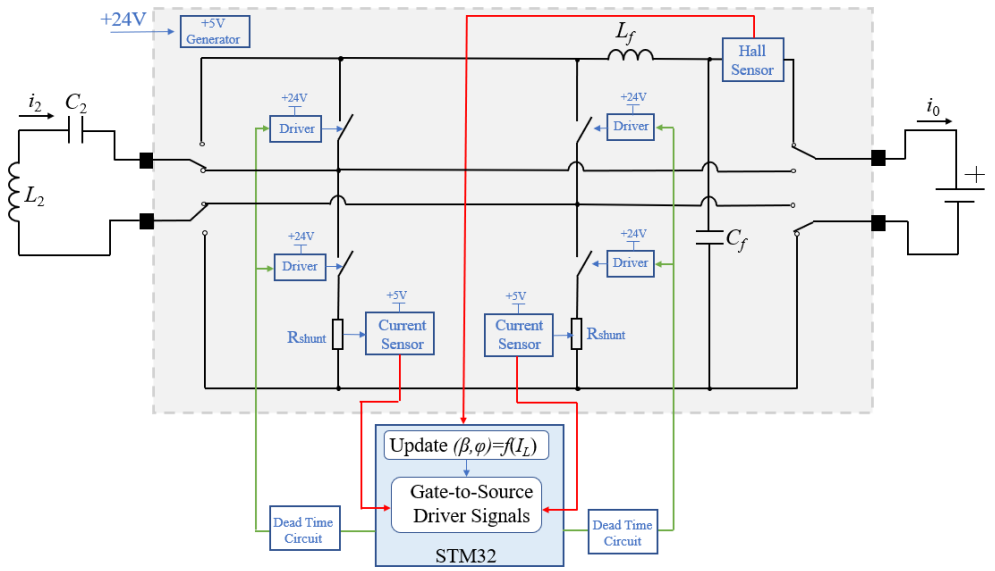

Figure 7.2: Logic circuit diagram of the power board.

The green lines are the input signals of the power board and they represent the switches driving signals. The regulation is made up from two control loops. The low speed outer loop consists on the measurement of the DC current delivered to the load I_o. It is checked every second and the sampled value is used to update the duty cycle and phase shift angle of the driving signals. The high-speed inner loop consists on the measurement of the secondary current i_2 and of driving signals generation.

In the next sections each part of the power board is analyzed in depth.

7.1.1. **Dead-time Circuit**

Deadtime is extremely important for controlled voltage source inverters (VSI) to avoid short circuit of DC link. If dead-time circuit are not used several problems such as additional losses, increasing of THD and even thermal runaway can occur. To solve these problems, many studies have been made to deal with the dead-time issues. The dead-time circuit used in this project is shown in Figure 7.3 (a).

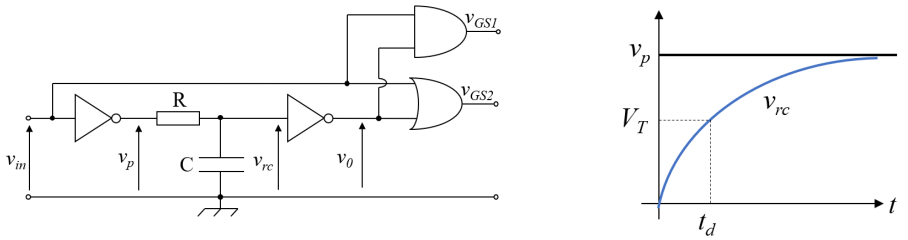

(a) (b)

Figure 7.3: Dead time circuit.

The deadtime interval t_d is created by an RC circuit. The driving voltage is v_{in}. Then, this voltage is negated and it is represented by v_p. When v_p is on high level, the voltage across the capacitance v_{rc} starts increasing with a time constant $\tau=RC$ as shown in Figure 7.3(b). When the voltage reaches the threshold V_T, the output voltage v_0 goes low. The waveforms of the circuit are shown in Figure 7.4. The deadtime between v_{GS1} and v_{GS2} is achieved.

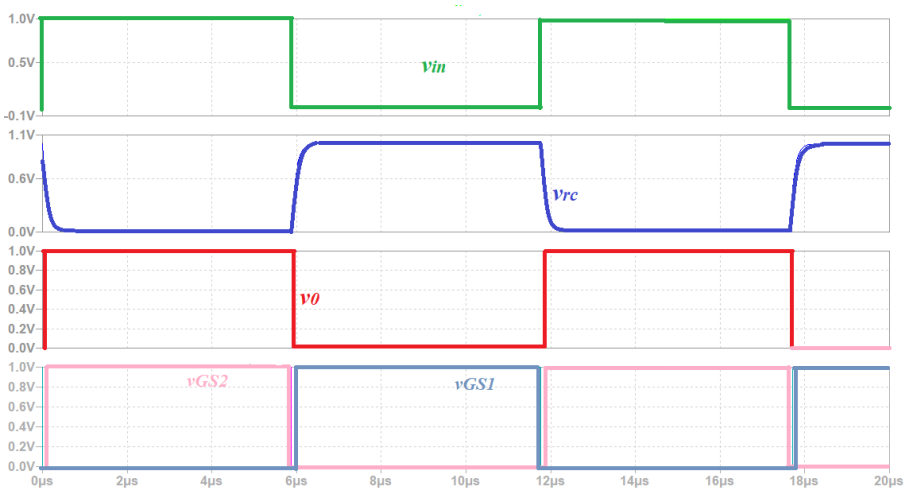

Figure 7.4: Waveforms of deadtime circuit

The deadtime interval can be regulated tuning the values of R, C and selecting the logic family technology used. The RC time constant is

$$\tau = RC \tag{135}$$

When the voltage v_p is high, the capacitor C starts charging, Thus the voltage v_{rc} is

$$v_{rc}(t) = V_p\left(1 - e^{-\frac{t}{\tau}}\right) \tag{136}$$

The relationship between the time constant τ and the dead-time t_d, is obtained

$$\tau = \frac{t_d}{\ln\left(\frac{V_p}{V_p - V_T}\right)} \tag{137}$$

Selecting R and C appropriately gives a particular dead time t_d

$$t_d = \tau \ln\left(\frac{V_p}{V_p - V_T}\right) \tag{138}$$

With the switching frequency f=85 kHz, a deadtime of t_d=100 ns is enough to prevent the previous citated issues. Using logic gates TTL compatible (V_p=+5V, V_T=2.1V), a resistance R=1kΩ, a capacitor C=183pF is used. In Figure 7.5 the driving signals and the relative deadtime are shown.

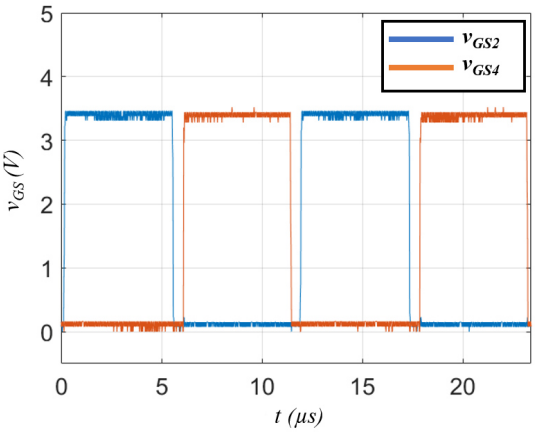

Figure 7.5: Gate to source driving signals.

7.1.2. Power Switch Considerations

The choice of the switching device is of primary importance for a power converter. Concerning the EV charging application, several papers available in literature have been compared. In [47], a comparison between a Si-IGBT, and a SiC MOSFET for WPT application shows that increasing the operating frequency, the power losses of SiC devices are significantly lower that using Si-IGBT.
The same results are substantially obtained in [48], where at 85kHz, the power losses is reduced of 30% using SiC MOSFETs in a 3kW WPT system.
Finally, in [49], a comparison of 22 kHz and 85 kHz 50kW wireless charging system using Si and SiC Switches for Electric Vehicle is presented. The results obtained are perfectly in line with the previous references [47-48].
Thus, all of the papers available in literature concerning the EV charging, shows that the use of Wide Bandgap Semiconductor (WBG), and in particular the SiC devices, are convenient for increasing the system performance. The benefits of SiC materials are numerous. A very high electric breakdown field allows for the design of power devices with ten times thinner and 100 times higher doped voltage blocking layers. The same voltage rating devices have a much smaller voltage drop and on-state resistance than their Si counterparts, which guarantees smaller conduction losses. In addition, SiC has a significantly lower intrinsic carrier concentration, resulting in a much higher temperature capability. This quality, along with high thermal conductivity, makes SiC suitable for high-temperature applications [50].
To confirm these results a market survey of power MOSFETs was carried out taking into account several characteristics such as:

- Conducting resistance r_{DS}^{ON}
- Drain to source maximum current I_{DS}^{MAX}
- Breakdown Voltage V_{DSS}
- Total Gate Charge Q_G
- Junction Temperature T_J
- Junction to Case thermal resistance R_{jc}
- Cost

The MOSFET used is the SCT3022AL from RHOM Semiconductor. The main characteristics are shown below.

Table 7.1: ELECTRICAL CHARACTERISTICS OF THE MOSFET

Parameter	Value
Drain-Source Breakdown Voltage $V_{(BR)DSS}$	650 V
Gate Threshold Voltage $V_{GS(th)}$	5.6 V
Drain-Source Static Resistance R_{DS}	22 mΩ
Continuous Drain Current	93 A
Gate Plateau Voltage $V_{plateau}$	9.6 V
Reverse Recovery Charge Q_{rr}	146 nC
Rise Time t_r	53 ns
Fall Time t_f	35 ns

7.1.3. **MOSFET Power Losses Estimation and Thermal Analysis**

For a preliminary switching losses estimation, the procedure proposed in [51] was used. The power losses in a MOSFET can be divided into three contributions:

- Conduction loss
- Switching loss
- Leakage loss: usually negligible.

The switching losses can be divided in two parts: turn-on and turn off switching losses. Using the simulations, the value of voltage across the MOSFETs before the turn-on transient and the value of current through the MOSFETs before the turn off transient can be estimated. In Fig7.6 the current and the voltage across the MOSFETs in one leg are shown, assuming that the system is working at the maximum output voltage V_{batt}^{max} =302.4V.

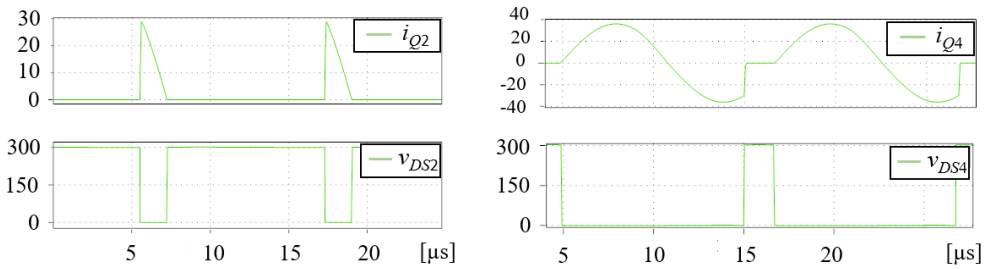

(a) (b)

Figure 7.6: Current and voltage across the high side and low side MOSFET (a) High side MOSFET (b) Low side MOSFET.

The interval used to estimate the turn-on and turn-off switching transient are shown in Figure7.7. As current and voltage levels quite high, two MOSFETs in parallel were used as power switch. Under this condition, the current flowing on each MOSFET is shown in Figure 7.6. For the high side MOSFETs, under the worst operating condition, the voltage before the turn on is V_{DS}^{max}=302.4 V. The turn-off occurs under zero current condition, thus without switching losses. For the low side MOSFETs, under the worst operating condition, the voltage before the turn on is V_{DS}^{max}=302.4 V, while the current before that turn off is I_{DS}^{max}=35 A.

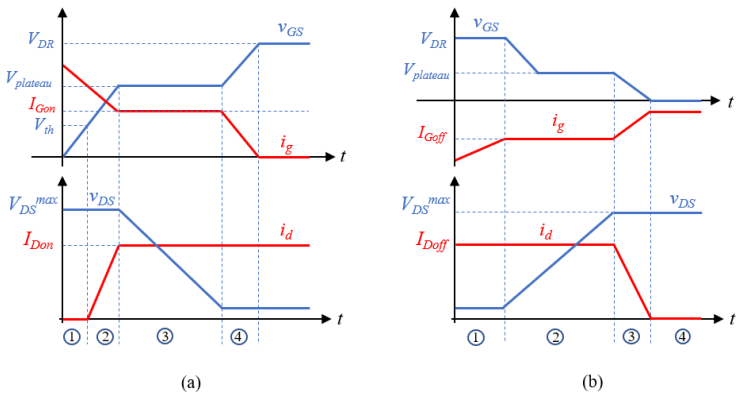

Figure 7.7: Switching transient of power MOSFET. (a) Turn-on transient. (b) Turn-off.

The turn-on switching transient can be divided into four main states:
State ①: The driver circuit changes its state from 0V to V_{DR}, the gate voltage rises to the threshold voltage V_{th}, with the time-constant defined by the gate resistor and the equivalent MOSFET input capacitance (C_{iss}=C_{GD}+C_{GS}). Until the gate voltage reaches the V_{th}, the drain to source voltage does not change.
State ②: After the V_{th} has been reached, the drain current i_D rises and takes over the load current. During this period, the drain-source voltage is V_{DS}^{max}.
State ③: the drain-source voltage is falling from V_{DS}^{max} to its on-state value V_{DS}^{on}=R_{DS} I_{Don}. The Miller effect takes place and the gate-source voltage is clamped at the $V_{plateau}$. The slope of the drain-source voltage is dictated through the gate current flowing through the gate-drain capacitance (C_{GD} = C_{rss}). The calculation of the voltage fall time is not easy because of the non-linearity of the gate-drain capacitances on the drain-source voltage. A reasonably caution choice for the estimation of switching losses is to select the value in the datasheet.
State ④: When the v_{DS} reach the conduction value of V_{DS}^{on}, the gate-source voltage reaches its final value V_{DR} and the gate current decreases to zero.

Switch-off process corresponds to the switching-on process of the MOSFET in the reverse order and will thus not be discussed in detail.

According to previous considerations, the worst-case turn-on energy losses in power MOSFET E_{on} can be calculated as the sum of the switch-on energy without taking the reverse recovery process into account and the switch-on energy caused by the reverse-recovery of the free-wheeling diode

$$E_{on} = \int_0^{t_r} v_{DS}(t) \cdot i_{DS}(t) dt = V_{DS}^{\max} \cdot I_{DS}^{on} \cdot t_r + Q_{rr} V_{DS}^{\max} \tag{139}$$

The switch-off energy losses in the MOSFET can be calculated in the similar manner. The switch-off losses in the diode are normally neglected. Therefore

$$E_{off} = \int_0^{t_f} v_{DS}(t) \cdot i_{DS}(t) dt = V_{DS}^{\max} \cdot I_{DS}^{off} \cdot t_f \tag{140}$$

The switching losses in the MOSFET and the diode are the product of switching energies and the switching frequency

$$P_{sw} = \left(E_{on} + E_{off}\right) \cdot f \tag{141}$$

Concerning the conduction losses, two different power losses occurs on the high side and low side MOSFET.
For the low side MOSFET the worst case is when the low side MOSFETs are conducting continuously (D=1). This situation can occur when no power has to be delivered to the load. The maximum power losses can be easily calculated as

$$P_C^L = R_{DS}^{on} I_{DS}^2 = 0.022 \cdot 35^2 = 26.95 \ W \tag{142}$$

For the high side MOSFET the worst case is when a duty cycle of D=0.5 is used. As calculated in the previous section, the current flowing through the low side MOSFETs is

$$I_{rms} = I_2 \sqrt{\frac{1}{2}(1-D) + \frac{1}{8\pi}\sin\left(2\pi(2D-1)\right)} = \frac{I_2}{2} \tag{143}$$

Thus, the conduction losses in the high side MOSFET is

$$P_C^H = R_{DS}^{on} I_{DS}^2 = 0.022 \cdot 17.5^2 = 6.73 \ W \tag{144}$$

The switch-off energy in the high side MOSFET is

$$E_{off}^H = V_{DS}^{\max} \cdot I_{DS}^{off} \cdot t_f = 420 \cdot 0 \cdot 35 \cdot 10^{-9} = 0 \ mJ \tag{145}$$

The switch-on energy in the high side MOSFET is

$$E_{on}^H = V_{DS}^{\max} \cdot I_{DS}^{on} \cdot t_r + Q_{rr} \cdot V_{DS}^{\max} = 302.4 \cdot 35 \cdot 53 \cdot 10^{-9} + 146 \cdot 10^{-9} \cdot 302.4 = 0.6051 \ mJ \tag{146}$$

The switch-off energy in the low side MOSFET is

$$E_{off}^L = V_{DS}^{\max} \cdot I_{DS}^{on} \cdot t_f = 302.4 \cdot 35 \cdot 35 \cdot 10^{-9} = 0.3704 \ mJ \tag{147}$$

The switch-on energy in the low side MOSFET is

$$E_{on}^L = V_{DS}^{\max} \cdot I_{DS}^{on} \cdot t_r + Q_{rr} \cdot V_{DS}^{\max} = 302.4 \cdot 0 \cdot 53 \cdot 10^{-9} + 146 \cdot 10^{-9} \cdot 302.4 = 0.0441 \ mJ \tag{148}$$

Thus, the total switching losses are

$$P_{tot}^H = \left(E_{on}^H + E_{off}^H\right) \cdot f = 51.43 \ W \tag{149}$$

$$P_{tot}^L = \left(E_{on}^L + E_{off}^L\right) \cdot f = 35.24 \ W \tag{150}$$

Thus, in Tab.7.2 are shown the estimated total power losses for both high side and low side MOSFETs.

Table 7.2: SWITCHING AND CONDUCTION POWER LOSSES

Parameter	Switching Power Losses	Conduction Power Losses	Total Power Losses
High Side Power MOSFET	51.43 W	6.73 W	58.16 W
Low Side Power MOSFET	35.24 W	26.95W	62. 91 W

These power losses estimation are needed for a correct design of the thermal heatsink.

Starting from the power loss estimation on each MOSFET, a thermal analysis to properly size the heatsink is carried out. The maximum power loss in a MOSFET can be P_{tot}=62.91W. After many comparisons among heatsinks, the B60-075 heatsink from OHMITE was selected. Each dissipation module is made up of two heatsinks connected to a fan as shown in Figure 7.15(a). On each dissipation module is mounted two MOSFETs, which operate electrically in parallel. The heatsink are placed in order to air flow, as shown in Figure 7.15(b). From the datasheet, assuming to connect two devices on the dissipation module and assuming to use a fan working with a flow rate of 28cfm, the heatsink thermal resistance is R_{th_sink}=0.92ºC/W.

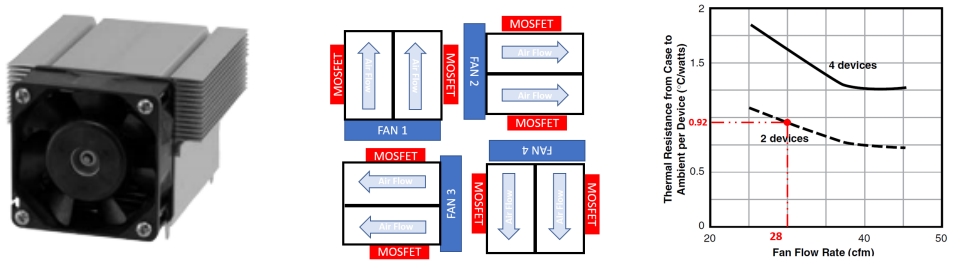

(a) (b) (c)

Figure 7.8 Heatsink. (a) Heatsink and fan Mechanical structure. (b) Disposition of heatsink on the board. (c) Thermal resistance varying the fan flow rate.

To guarantee electrical insulation between the MOSFET drain and the heatsink, a HI FLOW 300P Sil PAD is used. Its thermal resistance is R_{th_pad} 0.92°C/W under a pressure of 50 psi. From the SCT3022AL MOSFET datasheet, the junction to case thermal resistance is R_{th_jc}=0.44°C/W.

Table 7.3: THERMAL RESISTANCES.

Parameter	Value
Ambient Temperature	T_a=25 °C
Heatsink Thermal Resistance	$R_{th\ sink}$=0.92 °C/W
Silpad Thermal Resistance	$R_{th\ pad}$=0.92 °C/W
Junction to Case Thermal Resistance	$R_{th\ jc}$=0.44 °C/W

In Figure 7.16 (a) and (b) are shown the equivalent thermal model.

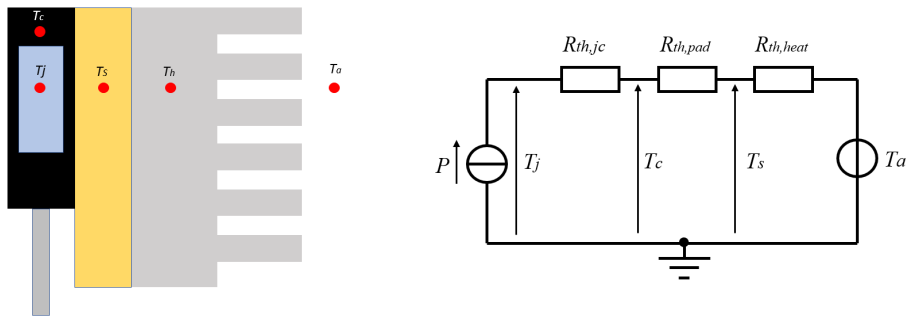

(a) (b)

Figure 7.9:Thermal temperature. (a) Temperature across the MOSFET, Silpad, heatsink and ambient temperature. (b) Equivalent thermal model.

The junction temperature of the SCT3022AL is T_j^{max}=175°C. The sink temperature T_s can be calculated as

$$T_s = T_a + P_{tot} R_{th\_sink} = 25 + 62.19 \cdot 0.92 = 82.21°C \tag{151}$$

The case temperature T_c will be

$$T_c = T_{sink} + P_{tot} R_{th\_pad} = 82.21°C + 62.19 \cdot 0.92 = 139.42°C \tag{152}$$

While the junction temperature T_j

$$T_j = T_c + P_{tot} R_{th\_jc} = 139.42°C + 62.19 \cdot 0.44 = 166.79°C \tag{153}$$

Achieving the safety condition T_j=166.79°C<175°C.

7.2 Current Sensing

As shown in the schematic in Figure 7.2, in order to implement the control strategy, two current measurements are needed. The FAR charges the vehicle battery through the output current i_0. This current must be controlled in order to ensure to the battery the desired charging profile and to avoid thermal drift ensuring safety operations. As the dynamic of this current particularly slow, it can be assumed to be a DC current. For this reason an Hall sensor was used for this measurement.
It is assumed that the system has to charge a battery made up from a parallel of 16 modules of 72 Li-Ion cells in series. A typical charging profile of a Li-Ion cell is shown in Figure 7.8.

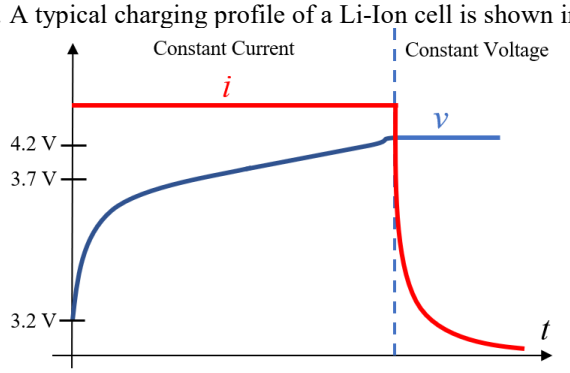

Figure 7.10: Li-Ion charging profile.

The minimum voltage of a Li-ion cell is approximately V_{cell}^{min}=3.7V, while the maximum voltage is V_{cell}^{max}=4.2V. Thus, when the battery pack is discharged, the minimum voltage of the pack is V_{batt}^{min}=3.7·72=266.4V. Assuming that the charging power is constant to P=3.7kW during the whole charging process, the maximum current which can flows to the battery is approximately I_{max}= P/ V_{batt}^{min}=13.88A. The maximum pack voltage is V_{batt}^{max}=4.2·72=302.4V Taking into account the current levels, a current sensor ACS770lcb-050U-PFF-T by Allegro was selected. This sensor measures a maximum unidirectional current I=50A with a sensitivity of 80mV/A and a -3db bandwidth BW=120kHz.

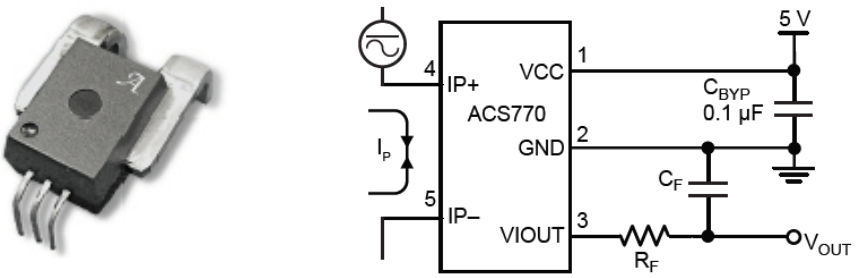

(a) (b)

Figure 7.11: Hall sensor. (a) Package used in the project. (b) Electric Schemathic.

Another measurement needed for the control strategy implementation is the secondary current i_2. This current is an 85kHz, 100A amplitude sinusoidal current. The only information needed for the control strategy is the zero-crossing detection of this sinusoidal current. As shown in Figure 7.1, the adopted solution used two shunt resistor R_{shunt} placed between the switch and

the ground. With one side of the shunt resistor referred to ground, this greatly simplifies the measurements reducing the voltage common mode requirements of the measurement ICs and makes possible to detect the zero crossing independently from the duty cycle and phase shift. The measurement chain and the ICs used for the measurement are shown in Figure 7.12 (a).

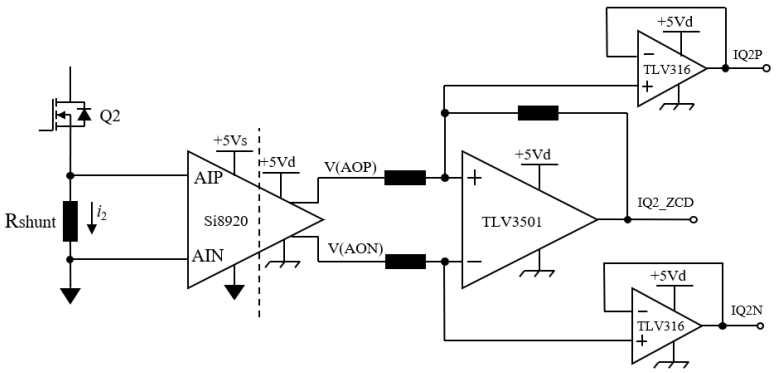

(a)

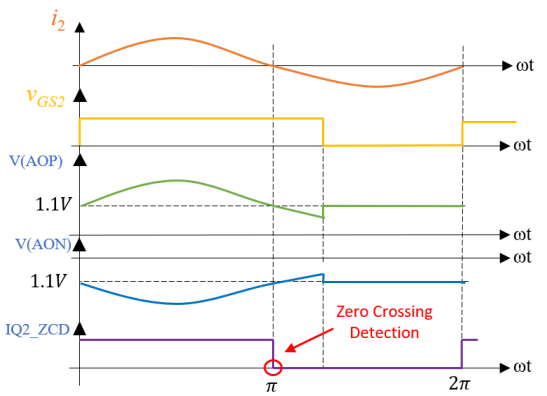

(b)

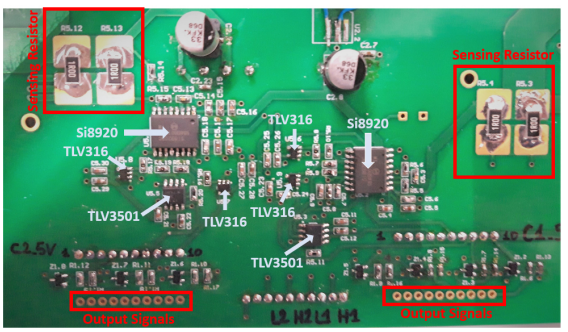

(c)

Figure 7.12: Secondary current measurement circuit. (a) Schematic. (b) Current and voltage waveforms across the circuit. (c) PCB layout.

It consists of a galvanically isolated analog amplifier Si8920B by Silicon Labs. The isolation is used to separate the FAR from the battery. It has a low-voltage differential input, ideal for measuring voltage across a current shunt resistor. The output has a differential output common mode voltage equals to (V_{AOP}+V_{AON})/2=1.1V. Each output signal is amplified by a factor 8.1. The main characteristics are summarized in Table 7.3.

Table 7.4: ELECTRICAL CHARACTERISTICS OF Si8920

Parameter	Symbol	Value
Specified Full-Scale Input Amplitude	$V_{AIP} – V_{AIN}$	–200 mV to +200mV
Full-scale Output	$V_{AOP} – V_{AON}$	1.62V
Signal Delay	t_{PD}	0.75µs
Amplifier Bandwidth	BW	950kHz

The waveforms are shown in Figure 7.12(b). To detect the zero-crossing a rail-to-rail high speed comparator TLV3501 is used. In order to increase its noise immunity a hysteresis is introduced. It is a push-pull output comparator with 4.5 ns propagation delay and a maximum toggle frequency f_{max}=80MHz. These high-speed characteristics make it suitable for this application. A feedback on the non-inverting input is used to obtain a hysteresis. This type of comparator is used to eliminate any unwanted indecision and switching caused by electrical noise. The input-output transfer function is shown in Figure 7.13.

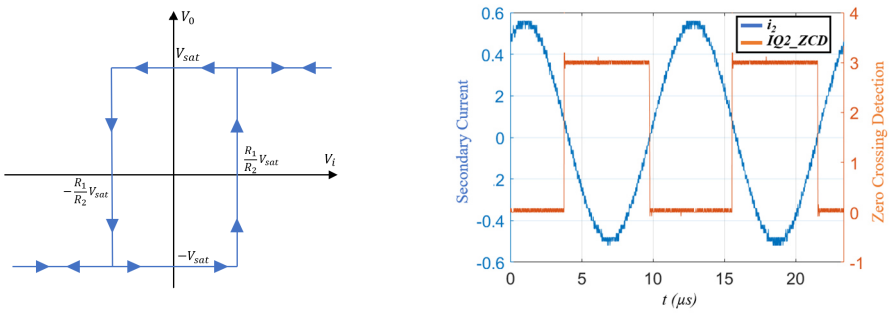

(a) (b)

Figure 7.13. (a) Hysteresis loop used to eliminate the undesired switching. (b) Zero crossing detection. The blue trace is the secondary current. The red trace is the zero-crossing signal, it changes state when a zero crossing occurs.

In Figure 7.13(b), the TLV3501 measured output voltage (IQ2_ZCD) is shown.

7.3 Resonant Compensation

Starting from the simulations results, the expected voltages and currents ratings of the resonant capacitors were estimated. In Figure 7.13 the voltages and currents through the primary and secondary capacitance are shown.

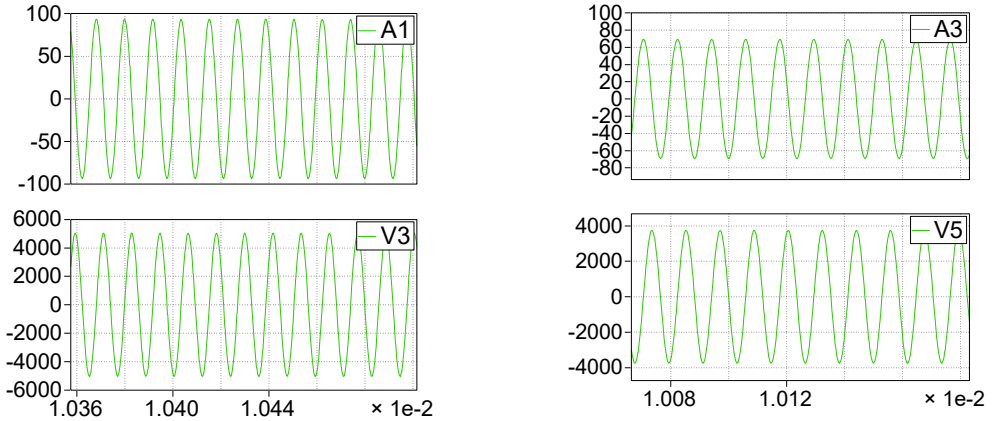

(a) (b)

Figure 7.14: Capacitors voltage and current ratings. (a) Resonant Primary capacitor. (b)Resonant Secondary Capacitor.

Because of resonance, both the current and voltage through the capacitances are sinusoidal. The amplitude of the primary current is approximately I_{C1}=100A, while the voltage V_{C1}=5000V. On the secondary side the current is I_{C2}=70A, while the voltage V_{C2}=4000V. The waveforms frequency is f_0=85 kHz. The high values of voltage and current ratings and the high switching frequency makes the choice of the best capacitor technology challenging.

In [52] a review on different capacitor technologies for wireless charging applications is presented. In this paper several capacitor technologies for EV wireless charging are studied focusing the attention on tight tolerance, low losses, low temperature coefficient and reliability. The study shows that polypropylene (PP) film capacitor exhibits better performance compared to the other technologies. In Table 7.4 are summarized the main technologies characteristics studied in the paper.

Table 7.5: CHARACTERISTICS OF DIFFERENT CAPACITOR.

Parameter	X7R	NPO	PET	PP
Tolerance	±10%	±1%	±1%	±1%
Losses	(7-0.2)% DF	(0.07-0.1)% DF	(0.2-1.4)% DF	(0.02-0.04)% DF
AC Voltage	>5kV	>5kV	>5kV	>5kV
Maximum Operating Temperature	125°C	125°C	125°C	105°C
Typical Operating Frequency Range	(0-10) MHz	(0-10) MHz	(0-150) kHz	(0-150) kHz
Reliability	Aging Hard Fault	No Aging Hard Fault	Graceful Aging Self-Healing	Graceful Aging Self-Healing

With the inductor L_1=82.43 μH and L_2=89.22 μH, in order to operate in resonance at f=85kHz, the resonant capacitances are respectively

$$C_1 = \frac{1}{\omega_0^2 L_1} = 45.53nF \tag{154}$$

$$C_2 = \frac{1}{\omega_0^2 L_2} = 39.29nF \tag{155}$$

Obviously no single capacitor able to operate at that high frequency and power ratings is available on the market. For this reason, a series and parallel connection of several capacitors is needed. The selected capacitor must have the following requirements:

- Low cost
- High voltage and current ratings
- Low parasitic resistance (ESR)
- Correct value to reach an equivalent capacitance of approximately C_{eq}=33nF.

After a market survey, the SNFP X0 2330 7D 4A KS00 from WIMA capacitor was selected. It has nominal value C=33 nF and exhibits a rated DC voltage of 4000V. One important parameter is the dissipation factor (tan δ), defined as the ratio of the ESR and capacitive reactance X_c. It is also known as the tangent of the loss angle

$$\tan\delta = \frac{ESR}{X_c} \tag{156}$$

The dissipation factor changes with the frequency. In Table7.5 the dissipation factor measured at 20°C for different frequency is shown.

Table 7.6: DISSIPATION FACTOR FOR DIFFERENT FREQUENCIES.

Frequency	tan δ
1 kHz	$6\cdot10^{-4}$
10 kHz	$6\cdot10^{-4}$
100 kHz	$15\cdot10^{-4}$

With the operating frequency f=85kHz, it is assumed tan δ=$10\cdot10^{-4}$. Thus, The parasitic resistance is

$$ESR = \tan\delta \bullet X_c = 10\cdot10^{-4}\cdot\frac{1}{2\cdot\pi\cdot85\cdot10^3\cdot33\cdot10^{-9}} = 0.0567\ \Omega \tag{157}$$

As shown in Figure 7.14(a) and (b) the maximum current flowing through the capacitor bank is I_1=100A. With this dissipation factor the power loss is

$$P_o = ESR\cdot\left(I_c^{rms}\right)^2 == 0.0851\cdot\left(\frac{100}{\sqrt{2}}\right)^2 = 283.5W \tag{158}$$

A critical aspect is related to the maximum voltage across the component. The maximum voltage with which the capacitor can operate decreases with the increasing of frequency. As shown in Figure 7.15, at f=85kHz, the maximum voltage is approximately V_{max}=300V, while the current I_{max}=7A.

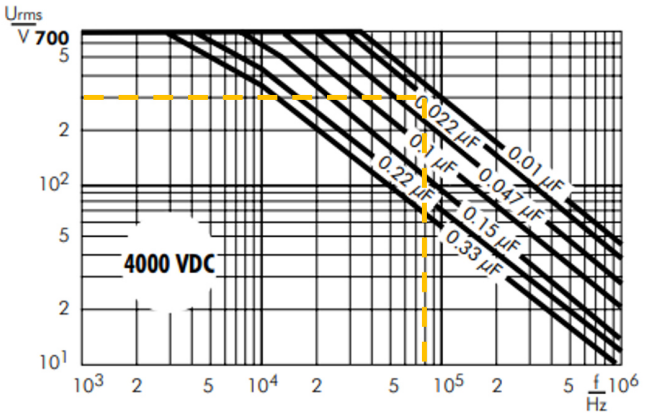

Figure 7.15: Permissible AC voltage in relation to frequency

To avoid fault, a matrix of capacitor has to be used. With the capacitance of C=33nF, a square matrix with the same number of capacitors in series N_s and in parallel N_p is chosen. The matrix dimension can be easily calculated as shown

$$N_p = \frac{I_{\max}}{I} = \frac{70}{7} = 10 \tag{159}$$

$$N_s = \frac{V_{\max}}{V} = \frac{5000}{300 \cdot \sqrt{2}} = 11.8 \cong 12 \tag{160}$$

In order to ensure safety operation and an equivalent capacitance of $C_{eq}=(N_p/N_s)\,C$, N_p=12 and N_s=12 is chosen. In Figure 7.16 the capacitors banks are shown.

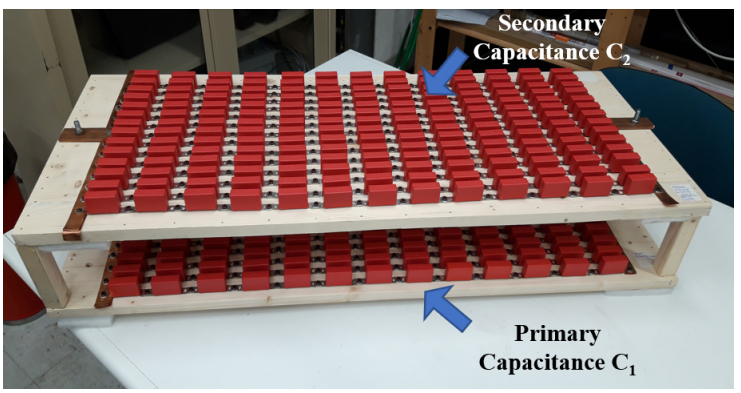

Figure 7.16:Capacitor bank.

7.5 STM32 Control Board

The STM32F4DISCOVERY control board with the STM32F407VG high performance microcontroller with the ARM® Cortex®-M4 32-bit core is used to implement the control strategy, which is made of two different loops as shown in Figure 7.17. The external loop does no needs particular requirements in terms of computational cost. It consists of a periodical measurement of the charging current i_o and of the updating of the duty cycle and phase shift reference. In this project the charging current is measured every second, therefore the outer loop has a frequency of 1Hz.

The second loop consist of the four MOSFETs driver signal generation. This is the high frequency loop because several tasks must be done every period:

- Zero Crossing (ZC) detection: it is necessary detect the zero crossing of the current i_2 under both positive (ZCP) and negative derivate (ZCN). This task is substantially performed from the external circuit on the power board, simplifying considerably the computational cost.
- Counting: after the detection of the zero crossing the MCU has to count for a time interval dependant from the duty cycle and the phase shift.
- Provide the input signal for the MOSFETs drivers.

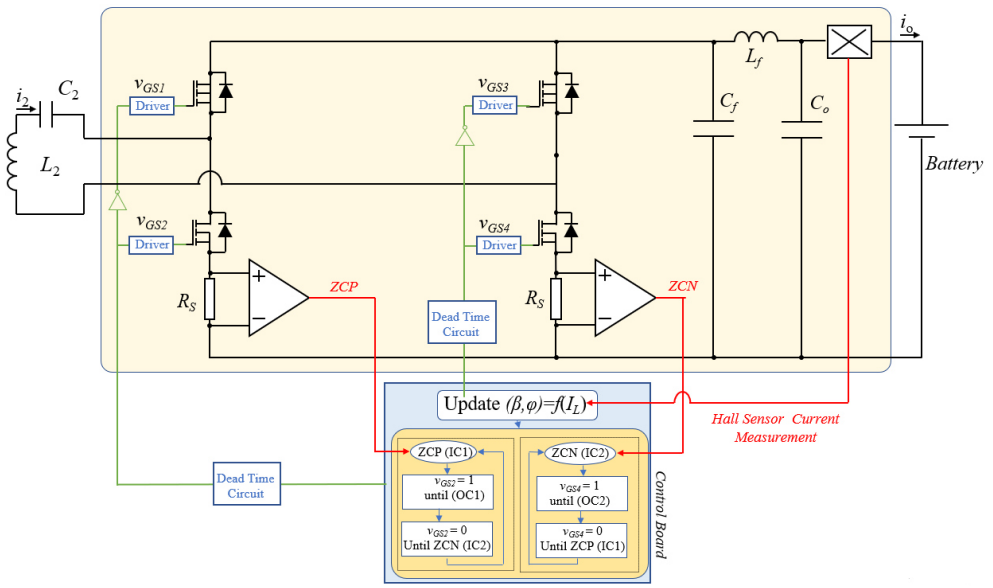

Figure 7.17: Control Strategy Diagram.

In Figure 7.19, the control waveforms for the first control strategy are shown.
The ZCP and ZCN are the output signal from the power board. These signals are received from the STM32 board and used to detect the zero crossing of the secondary current i_2 though two interrupts called IC1 for the ZCP and IC2 for ZCN. The input capture (IC) can be used to capture the time of a specific, user defined, event. The event could be falling, rising, or any edge. When a ZC is detected, a counter is initialized. When the counts reach a threshold value dependant from the duty cycle, an interrupt OC1 or OC2 is detected. The output compare (OC) allows the user to generate an output signal when the value of the free running counter reaches a defined value.

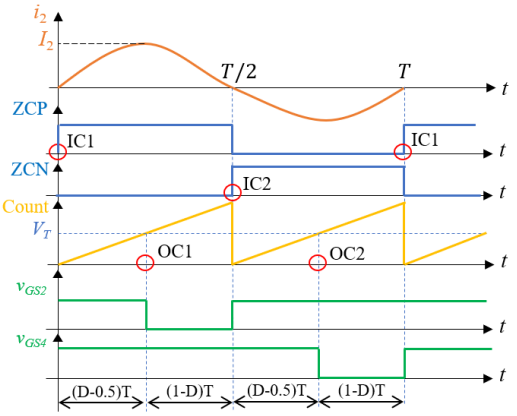

Figure 7.18: Implementation on STM32.

Given the high computational cost needed to perform all these tasks, the STM32F407VG mounting a microcontroller ARM® Cortex®-M4 32-bit core (core frequency is 168MHz) was chosen as good compromise between performance and cost. To program the board the STM32CubeMx tool was used. It consists of a graphical tool that allows a very easy configuration of STM32 microcontrollers, including STM32F4DISCOVERY. It is used to generate the initialization code. After the pin initialization and the control strategy was write in c on Truestudio by Atollic.

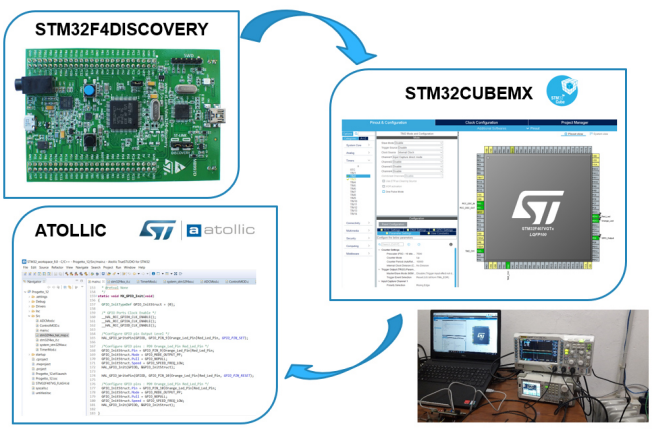

Figure 7.19: Control board programming process.

7.6 Experimental Results

The experimental prototype setup built in laboratory is shown in Figure 7.19. The three-phase grid voltage is regulated by a Variac and rectified by a three phase rectifier. Thus, the DC generator is able to provide a DC voltage between 0-300V and the power is limited to P_{max}=6 kW. The Variac made possible to expose the components to the stress gradually. The DC current is converted into a f=85kHz alternate voltage by the power borad inverter. Then, the voltage supplies the resonant tank made up of two inductor L_1 and L_2 and the resonant capacitor C_1 and C_2. The high frequency AC secondary current is then rectified by the FAR. The control is performed by the STM32 programming board. A rheostat was used as load in order to simulate different operating points along the charging characteristics of the battery.

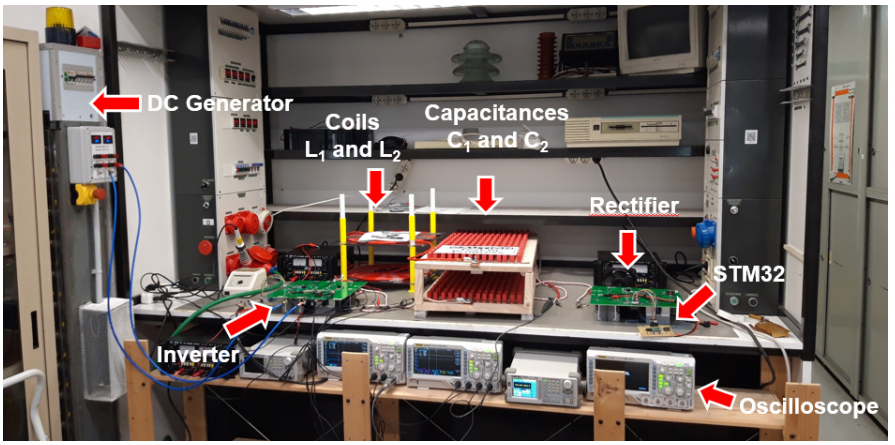

Figure 7.209: Experimental Setup

In Figure 7.20 the current and voltage waveforms at the input of the active rectifier are shown. The secondary current i_2 is substantially constant independently from the duty cycle β and the phase shift. Depending on φ and β, the output current can be modulated. With the FAR connected to a resistive load, the output voltage changes when the current changes, as shown in Figure 7.21. In Figure 7.21 (a), the case φ=0 and β=π/2 is shown. In Figure 7.21 (b), the case with φ=0 and β=π/2 is shown and the transferred output is approximately P_o=2.047Kw. In Figure 8.2(c) the case φ= - π/4 and β=π/2 is shown while in Figure 8.2(d) the case φ= +π/8 and β=π/2 is shown.

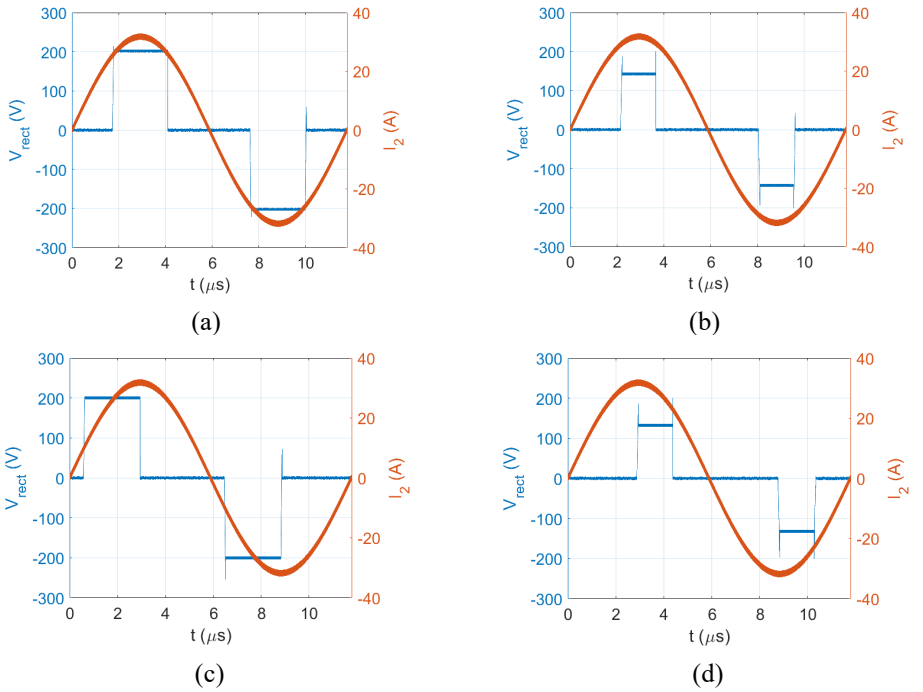

Figure 7.210: Voltage and currents at the input of the rectifier. (a) Case φ=0 and β=π/2. (b) Case φ=0 and β=π/4. (c) Case φ= - π/4 and β=π/2. (d) Case φ= +π/8 and β=π/2.

The overall efficiency for different output power is shown in Figure 7.21.

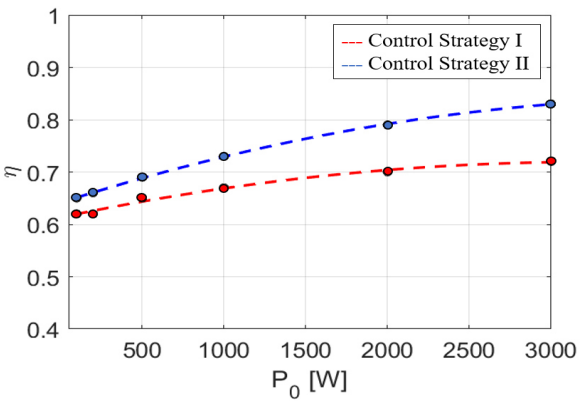

Figure 7.21: Overall system efficiency for different output power.

The maximum system efficiency is reached at full load, and it is $\eta_{sys}=\eta_{tran}\cdot\ \eta_{FAR}$=0.82.

8. Conclusions

The research carried out during the PhD course was focused on the analysis and design of a secondary side controlled charging system. Unlike most of the wireless charging system available in the market and in literature, in the proposed solution the power transmission control strategy is implemented and managed from the vehicle side. The system is based on a power board placed on the vehicle able to manage the power received from the primary and charge the EV battery.

The scientific novelty of the proposed system consists on the possibility to charge the EV and simultaneously to maximize of the transmission efficiency through a continuous impedance matching. The condition under this operation can be performed if found analytically and validated experimentally.

Thanks to the interrupt-based control technique, the secondary power board is able to implement the control independently from the primary operating frequency. The only necessary operation is the secondary capacitance adjustment in order to resonate with the secondary coil at the new frequency. This operation can be performed by sectioning the capacitances array using power switches.

Two different control strategies have been developer and compared. The first control strategy is based on the duty cycle variation, while the second control strategy uses an extra control parameter that is the phase shift. From the mathematical point of view, it is shown that the first control strategy, computationally easier, allows to manage the energy received on the secondary side and it gives the desired charging profile to the battery. However, this control strategy does not allow to maximize the transmission efficiency because of the equivalent resistance of the active rectifier that it is never equal to the optimal one. Introducing the phase shift as additional control variable, it is possible to charge the vehicle and simultaneously maximize the transmission efficiency. The efficiency improvement introduced from the second control strategy is confirmed experimentally. The system efficiency is lower for lower output power because of semiconductor power losses, which are substantially constant as the output power changes.

As future developments, the efficiency can be improved by reducing the parasitic components and investigating further solution to increase the coupling between the coils leading to an higher transmission efficiency.

Bibliography

[1] A. Abas, J. Yong, M. Mahila, A. Hannan, "Techno-Economic Analysis and Environmenal Impact of Electric Vehicles", IEEE Access, Vol.7, July 2017, pp. 98565-98578.

[2] M. Ramoni, H. Zhang, End-of-life (EOL) issues and options for electric batteries, Springer-Verlag Berling Heidelberg 2013.

[3] Feyijimi Adegbohun , Annette von Jouanne, and Kwang Y. Lee, "Autonomous Battery Swapping System and Methodologies of Electric Vehicles", energies MDPI, 19 February 2019.

[4] V. Doan, H. Fujimoto, T. Koseki, T. Yasuda, H. Kishi, T. Fujita, "Allocation of Wireless Power Transfer System from Viewpoint of Optimal Control Problem for Autonomous Driving Electric Vehicle", *IEEE Trans. on Intelligent Transportation System*, Vol. PP, pp. 1-16.

[5] C. Mi, G. Buja, S. Y. Choi, and C. T. Rim, "Modern advances in wireless power transfer systems for roadway powered electric vehicles," *IEEE Trans. Ind. Electron.*, vol. 63, no. 10, pp. 6533–6545, Oct. 2016.

[6] WiT-3300TMResonator Pair R2.3. Available:http://www.witricity.com/assets/WiT-3300_R2.3_DS.pdf

[7] R. Hough, ''EvatranTMAwarded Department Of Energy Sub-Contract ToIntegrate High Power Wireless Charging Technology Into ProductionElectric Vehicles," in PluglessTMLevel 2 EV Charging System (3.3kW), ed. PRNewswire Association LLC: PR Newswire Association LLC, 2013.

[8] A. Munir, B. Ranun, "Wireless Power Charging System for Mobile Device Based on Magnetic Resonance Coupling", 5th International Conference on Electrical Engineering and Informatics, Aug. 10-11, 2015, Bali, Indonesia.

[9] Hua Zhang, Fei Lu, Heath Hofmann," A Four-Plate Compact Capacitive Coupler Design and LCL-Compensated Topology for Capacitive Power Transfer in Electric Vehicle Charging Application", IEEE Transaction on Power Electronics, Vol. 31, NO.12, December 2016, 16. pp. 8541-8551.

[10] L. Yang, M. Ju and B. Zhang, Bidirectional Undersea Capacitive Wireless Power Transfer System, IEEE Access (Volume: 7), 27 August 2019, pp. 121046 – 121054.

[11] B. Regensburger, A. Kumar, S. Sinha and K. Afridi , High-Performance 13.56-MHz Large Air-Gap Capacitive Wireless Power Transfer System for Electric Vehicle Charging, IEEE 19th Workshop on Control and Modeling for Power Electronics (COMPEL), 25-28 June 2018, Padua, Italy.

[12] A. Koruprolu, R. Erfani, P. Mohseni and S. Nag, Capacitive Wireless Power and Data Transfer for Implantable Medical Devices, IEEE Biomedical Circuits and Systems Conference (BioCAS), 17-19 Oct. 2018, Cleveland, OH, USA.

[13] Brock J. DeLong, Asimina Kiourti, and John L. Volakis, "A Radiating Near-Field Patch Rectenna for Wireless Power Transfer to Medical Implants at 2.4 GHz", IEEE Journal of Electromagnetism, RF and Microwaves in Medicine and Biology, VOL. 2, NO. 1, March 2018, pp. 64-69.

[14] Hao Zhang ; Yong-xin Guo ; Zheng Zhong ; Wen Wu, "Cooperative Integration of RF Energy Harvesting and Dedicated WPT for Wireless Sensor Networks", IEEE Microwave and Wireless Components Letters, Vol. 29 , Issue 4 , April 2019 , pp. 291 – 293.

[15] Med Nariman, Anna Papió Toda, Ahmadreza Rofougaran, Franco De Flaviis, "A Compact 60-GHz Wireless Power Transfer System", IEEE Transaction on Microwave Theory and Techniques, Vol. 64, No. 8, August 2016, pp. 2664-2677.

[16] A. Reatti, F. Corti, L. Pugi, L. Berzi, R. Barbieri, M. Delogu, M. Pierini, "Application of Induction Power Recharge to Garbage Collection Service", 3rd International Forum on Research and Technologies for Society and Industry, 11-13 Sept. 2017, Modena, Italy.

[17] M. Longo, D. Zaninelli, A. Cipriani, V. Di Dio, . Miceli, "Economic Assessments on the Use of Wired and Wireless Recharging Systems in Italian and European Market", IEEE AEIT onference, 20-22 Sept. 2017, Cagliari, Italy

[18] C. Panchal, S. Stegen, J. Lu, "Review of static and dynamic wireless electric vehicle charging system", Engineering Science and Technology an International Journal, 27 June 2018, pp. 922-937.

[19] Devendra Patil, Matthew K. Mcdonough, John M. Miller, Babak Fahimi, Poras T. Balsara, ,"Wireless Power Transfer for Vehicular Applications: Overview and Challenges", IEEE Transaction on Transportation Electrification, Vol. 4, No. 1, March 2018.

[20] ICNIRP Guidelines for Limiting Exposure to Time-Varying Electric and Magnetic Fields (1Hz – 100 kHz), Health Physics, 2010, pp. 818-836.

[21] John M. Miller, Omer C. Onar, and Madhu Chinthavali, "Primary-Side Power Flow Control of Wireless Power Transfer for Electric Vehicle Charging", IEEE Journal of Emerging and Selected Topics in Power Electronics, Vol.3, No. 1, March 2015.

[22] M. Khalilian and P. Guglielmi, "Primary-Side Control of a Wireless Power Transfer System with Double-Sided LCC Compensation Topology for Electric Vehicle Battery Charging", IEEE International Telecommunications Energy Conference (INTELEC), 7-11 Oct. 2018, Turin, Italy.

[23] K. Hata, T. Imura, Y. Hori, "Maximum efficiency control of wireless power transfer systems with Half Active Rectifier based on primary current measurement", 3-7 June 2017, Kaohsiung, Taiwan.

[24] X. Liu, X. Yang, D. Ma and H. Tang, "A Novel Receiver for Dual-side Controlled Wireless Power Transfer System", Wireless Power Transfer Conference (WPTC), 3-7 June 2018, Montreal, QC, Canada, Canada.

[25] Y. Geng et all, "Optimization of Dual Side Control Strategy for Wireless Power Transfer System in Light Rail Vehicle", IEEE PELS Workshop on Emerging Technologies: Wireless Power Transfer (WoW), 4-6 Oct. 2016, Knoxville, TN, USA.

[26] Q. Zhao, A. Wang, J. Liu, X. Wang, "The Load Estimation and Power Tracking Integrated Control Strategy for Dual-Sides Controlled LCC Compensated Wireless Charging System", IEEE Access, Vol.7, 12 June 2019, pp. 75749 – 75761.

[27] B. Pang, J. Deng, P. Liu, Z. Wang, "Secondary-Side Power Control Method for Double-side LCC Compensation Topology in Wireless EV Charger Application", 43rd Annual Conference of the IEEE Industrial Electronics Society, 29 Oct.-1 Nov. 2017, Beijing, China.

[28] Z. Li, K. Song, C. Zhu, R. Lu, G. Wei, "Constant Current Charging for Variable Load Employing Secondary Side Controlled Wireless Charging System", IEEE Transportation Electrification Conference and Expo, Asia-Pacific (ITEC Asia-Pacific), 7-10 Aug. 2017, Harbin, China.

[29] G. Lovison, T. Imura, H. Fujimoto, Y. Hori, "Secondary-side-only Control for Smooth Voltage Stabilization in Wireless Power Transfer Systems with Constant Power Load", International Power Electronics Conference (IPEC-Niigata 2018 - ECCE Asia), 20-24 May 2018, Niigata, Japan.

[30] L. Pamungkas, M. Tampubolon, Q. Lin , H. Chiu, "Performance Comparison of Primary Side PFM and Secondary Side PWM for SS Wireless Power Transfer CC/CV Control Strategy", IEEE International Power Electronics and Application Conference and Exposition , 4-7 Nov. 2018, Shenzhen, China

[31] S. Li, W. Li, J. Deng, C. Mi, "A Double-Sided LCC Compensation Network and Its Tuning Method for Wireless Power Transfer", IEEE Transactions on Vehicular Technology, Vol. 64 , Issue 6, 2014, pp. 2261 – 2273.

[32] C. Liu, C. Jiang, C. Qiu, "Overview of Coil Designs for Wireless Charging of Electric Vehicle", Workshop on Emerging Technologies: Wireless Power Transfer, 20-22 May 2017, Chongqing, China.

[33] T. Boys and A. Covic, "Magnetic Circuits for Powering Electric Vehicles", IPT Fact Sheet Series: No. 2.

[34] Abiezer Tejeda, Seho Kim, Fei Yang Lin, Grant A. Covic, John T. Boys, "A Hybrid Solenoid Coupler for Wireless Charging Applications", IEEE TRANSACTIONS ON POWER ELECTRONICS, VOL. 34, NO. 6, JUNE 2019, pp. 5632-5645.

[35] D. Ongayo and M. Hanif, "Comparison of circular and rectangular coil transformer parameters for wireless power transfer based on finite element analysis", IEEE 13th Brazilian Power Electronics Conference, 29 Nov.-2 Dec. 2015, Fortaleza, Brazil.

[36] M. Budhia, J. T. Boys, G. Covic and C. Huang, Development of a Single-Sided Flux Magnetic Coupler for Electric Vehicle IPT Charging Systems, IEEE Transaction on Industrial Electronics, Vol. 60, NO. 1, January 2013.

[37] N. Rasekh, M. Mirsalim, "Analysis of a Compact and Efficient DDQ pad Integrated to the LCC Compensation Topology for IPT", Annual Power Electronics, Drive Systems, and Technologies Conference, 2018, Tehran, Iran.

[38] Adeel Zaheer, Grant A. Covic , Dariusz Kacprzak, "A Bipolar Pad in a 10-kHz 300-W Distributed IPT System for AGV Applications", IEEE Transaction on Industrial Electronics, , Vol. 61, NO. 7, July 2014.

[39] A. Ahmad, M. Alam, R. Chaaban, "A Comprehensive Review of Wireless Charging Technologies for Electric Vehicles", IEEE Transaction on Transportation Electrification, Vol. 4, NO. 1, March 2018.

[40] A. Dolara, S. Leva, M. Longo, F. Castelli, M. Mauri, "Power Pad Design and Optimization for Contactless Electric Vehicle Battery Charging System", IEEE International Conference on Environment and Electrical Engineering, 6-9 June 2017, Milan, Italy.

[41] A. Dolara, S. Leva, M. Longo, F. Castelli, M. Mauri, "Coil Design and Magnetic Shielding of a Resonant Wireless Power Transfer System for Electric Vehicle Battery Charging", IEEE 6th International Conference on Renewable Energy Research and Applications , 5-8 Nov. 2017, San Diego, CA, USA.

[42] H. Wheeler, "Simple Inductance Formulas for Radio Coils", Prooceding of the Institute of Radio Engineers, Vol. 16, Issue 10, Oct.1928, pp. 1398-1400.7

[43] Y. Sakaki, T. Matsouka, "Hysteresis Losses in MnZn Ferrite cores", IEEE Transaction on Magnetics, Vol.22, No.5, pp. 623-625, September 1986-

[44] M. Mohammad, S. Choi, "Optimization of ferrite core to reduce the core loss in double-D pad of wireless charging system for electric vehicles". IEEE Applied Power Electronics Conference and Exposition, 17-21 March 2018, Anaheim, CA, USA, pp. 1350-1356.

[45] H. Jiang, P. Brazis, M. Tabaddor, J. Bablo, "Safety Consideration of Wireless Charger for Electric Vehicle- A review paper", IEEE Symposium on Product Compliance Engineering, 5-7 November 2012, Portland, OR, USA, pp. 1-6.

[46] S. Raju, R. Wu, M. Chan, C. Yue, "Modeling of Mutual Coupling Between Planar Inductors in Wireless Power Transfer Applications", IEEE Transaction on Power Electronics, 2014, pp. 481-490.

[47] S. Ohara et all, "Comparative Study of IGBT and SiC-mosfet IN A Wireless V2H System with a New Bidirectional Single-Ended ZVS Converter", IEEE International Power Electronics and Motion Control Conference, 25-28 Sept. 2016, Varna, Bulgaria.

[48] R. Maeno et all, "A 3kW Single-Ended Wireless EV Charger with a Newly Developed SiC-VMOSFET", International Conference on Renewable Energy Research and Applications, 14-17 Oct. 2018, Paris, France.

[49] M. Haque, M. Mohammad, J. Pries, S. Choi, "Comparison of 22 kHz and 85 kHz 50kW Wireless Charging Using Si and SiC Switches for Electric Vehicle", 6th Workshop on Wide Bandgap Devices and Applications, 2 Nov. 2018, Atlanta, USA.

[50] Di Han, Jukkrit Noppakunkajorn, Bulent Sarlioglu, "Comprehensive Efficiency, Weight, and Volume Comparison of SiC- and Si-Based Bidirectional DC–DC Converters for Hybrid Electric Vehicles", IEEE Transaction on Vehicular Technology, Vol. 63, No. 7, Sept. 2014.

[51] Dušan Graovac, Marco Pürschel, Andreas Kiep, "MOSFET Power Losses Calculation Using the DataSheet Parameters", Application Note, V 1.1, July 2006.

[52] M. Brubaker, H. Kirbie, A. Hosking, T. Kampen, "System Level Considerations for Integration of Resonant Capacitors in High Power Wireless Charging", Conference on Electric Roads and Vehicles, 2012.